2021

Axial Symmetry Tests of Milky Way Disk Stars Probe the Galaxy's Matter Distribution

Austin Hinkel
University of Kentucky, austin.hinkel7@gmail.com
Author ORCID Identifier:
https://orcid.org/0000-0002-9785-914X
Digital Object Identifier: https://doi.org/10.13023/etd.2021.471

STUDENT AGREEMENT:

I represent that my thesis or dissertation and abstract are my original work. Proper attribution has been given to all outside sources. I understand that I am solely responsible for obtaining any needed copyright permissions. I have obtained needed written permission statement(s) from the owner(s) of each third-party copyrighted matter to be included in my work, allowing electronic distribution (if such use is not permitted by the fair use doctrine) which will be submitted to UKnowledge as Additional File.

I hereby grant to The University of Kentucky and its agents the irrevocable, non-exclusive, and royalty-free license to archive and make accessible my work in whole or in part in all forms of media, now or hereafter known. I agree that the document mentioned above may be made available immediately for worldwide access unless an embargo applies.

I retain all other ownership rights to the copyright of my work. I also retain the right to use in future works (such as articles or books) all or part of my work. I understand that I am free to register the copyright to my work.

REVIEW, APPROVAL AND ACCEPTANCE

The document mentioned above has been reviewed and accepted by the student's advisor, on behalf of the advisory committee, and by the Director of Graduate Studies (DGS), on behalf of the program; we verify that this is the final, approved version of the student's thesis including all changes required by the advisory committee. The undersigned agree to abide by the statements above.

Austin Hinkel, Student

Dr. Susan Gardner, Major Professor

Dr. Chris Crawford, Director of Graduate Studies

Axial Symmetry Tests of Milky Way Disk Stars Probe the Galaxy's Matter Distribution

DISSERTATION

A dissertation submitted in partial
fulfillment of the requirements for
the degree of Doctor of Philosophy
in the College of Arts and Sciences
at the University of Kentucky

By
Austin Hinkel
Lexington, Kentucky

Director: Dr. Susan Gardner, Professor of Physics & Astronomy
Lexington, Kentucky
2021

https://orcid.org/0000-0002-9785-914X

ABSTRACT OF DISSERTATION

Axial Symmetry Tests of Milky Way Disk Stars Probe the Galaxy's Matter Distribution

In Galactic dynamics, various assumptions have been employed for mathematical ease. These assumptions are approximately valid, but departures reveal perturbations on our Galaxy. In this dissertation, we select a complete, Gaia DR2 data set, and using this data, we find evidence for axial symmetry breaking in the Galaxy, away from the spiral arms and the Galactic bar. This asymmetry is compatible with a prolate dark matter halo tilted with respect to the disk, with a long axis pointing in the direction of the Magellanic Clouds, and this matches an inventory of nearby torques. These asymmetries vary North and South of the mid-plane, which we interpret as evidence of non-steady-state effects, and we note that it varies radially. Indeed, the axial asymmetry changes sign towards the Galactic center, and this matches expectations of an orbit "flip" near the Outer Lindblad Resonance. Using this, we infer the pattern speed of the Galactic bar, though other interpretations are possible. Finally, we test the symmetry of pair counts via correlation function analyses, probing structural differences throughout the nearby Galaxy. Accounting for survey geometry, we show that two-particle correlations abound which cannot be explained by steady-state effects.

KEYWORDS: Astronomy, Galactic Dynamics, Galactic Archaeology, Galactoseismology

Austin Hinkel

December 16, 2021

AXIAL SYMMETRY TESTS OF MILKY WAY DISK STARS PROBE THE GALAXY'S MATTER DISTRIBUTION

By
Austin Hinkel

Susan Gardner
Director of Dissertation

Chris Crawford
Director of Graduate Studies

12/15/2021
Date

ACKNOWLEDGMENTS

I would like to express my deepest gratitude and appreciation to a number of people, without whom this work would not exist.

First, a huge thank you is owed to my advisor, Dr. Susan Gardner, for her guidance and unwavering support over the past several years. Both Susan and my mentor Dr. Brian Yanny have my deepest gratitude for their countless hours of collaboration, instruction, and feedback. This work has benefited immensely from their expertise, as has my development as a scientist.

Second, I would like to thank my parents, who have kindled my love of science, and who have provided countless opportunities to stoke that passion throughout the years.

Additionally, to my friends and family, who have had to put up with my undying urge to talk about all things science: thank you – merely allowing me to wax poetic about my work was a bigger part of my support system than you will likely ever know.

Finally, the highest form of thanks is owed to my wife, Grace, who has endured the long periods of work-life imbalance that has become rather synonymous with graduate school, all in the name of me achieving a lifelong dream. Grace has been a huge factor in my decision to stick with graduate school despite the roadblocks I encountered, and for this I will be eternally grateful.

Oh – and also coffee.

TABLE OF CONTENTS

LIST OF TABLES

LIST OF FIGURES

Chapter 1 A Brief Preface

For millennia, humans have looked up and wondered about the milky swath of stars spilling across the sky. It has held many names: for the Greeks, *Galaxius*, while the Chinese Jin Dynasty referred to the galaxy as a "Silver River" (Waller, 2017). In Greek mythology, the band of light was said to have come from the spilled breast milk of the goddess Hera, directly leading to the popular name of our galaxy, the Milky Way (Waller, 2017). Indeed, even the word Galaxy itself comes from the Greek word for milk (Harper et al., 2001).

Despite the collective curiosity of generations past, it has not been until the past few centuries that humanity has been able to learn more about our home Galaxy, as well as others. While perhaps a shock to the non-astrophysicist, the astronomy community does not actually have a complete picture of what our own Galaxy looks like. There are numerous examples of disagreements in the literature as to how the Milky Way looks and how it behaves.

We can, however, see other galaxies through various telescopes and learn more about the possibilities and evolutionary paths for our own Galaxy through the observed ensemble. Due to the immense scale of the Milky Way and the limitations of currently established physical laws, it seems unlikely that humanity will ever be able to send a probe far enough away to image our entire Galaxy directly. Alas, we are essentially stuck in a forest, condemned to infer the structure of the sylvan landscape by noticing patterns within the trees which we are able to see.

The outlook is not all that bad. Despite the difficulties associated with developing a picture of a structure from within, ever advancing telescope technology has opened the skies to insightful analysis. In the era of "big data" and at a time when the Gaia space telescope allows an unprecedented look at the galaxy, there is no better time than the present to analyze the Milky Way. Indeed, we do just that in the field of Galactic Archaeology.

Not unlike an archaeologist unearthing an array of structures in an ancient dig site, galactic archaeologists "dig" through these ever-growing troves of data in hopes of finding extant structure within the Milky-Way. Much akin to the artefacts at a traditional dig site, the structures found within the Milky Way's stars can help piece together a story of the Galaxy's past: a past apparently rife with collisions and interactions with other galaxies, each leaving their own distinct mark on our own. Armed with data on billions of stars, this dissertation outlines a few novel methods of analysis to be added to the Galactic Archaeologist's toolbox, and submits a number of new findings in the story of the Milky Way.

Chapter 2 Introduction

Astrophysics often differs from other sub-fields of physics in that we cannot study many of the associated phenomena in a laboratory – the spatial and temporal scales involved are simply too substantial. Thus, we are left with only observational evidence and theory. To even begin describing the cosmos through theoretical means, the astrophysics community has had to employ various assumptions regarding the structure and dynamics of the Milky Way, purely out of necessity. Of course, many of the assumptions are rooted in firm principles and may largely hold up well in light of exponentially increasing data volume, but it is precisely the departures from these assumptions that reveal interesting structures and dynamic effects that stretch our understanding of the Galaxy. To this end, this dissertation offers a novel look at the breaking of some of these assumptions and what the departures from the various assumed behaviors tell us about the history, structure, and dynamics of the Galaxy.

In order to better understand the necessity of the assumptions that have heretofore governed the theory of Galaxy dynamics, it is useful to first consider the collisionless nature of stars. Our star, for example, is some million kilometers in diameter, while the distance to the next closest star is some 7 orders of magnitude greater. Thus, in the enormity of space that our Galaxy occupies, individual stars are mere points, or particles. Moreover, the Galaxy, as a collective of stars, exerts a gravitational force on its constituent stars that does not vary wildly from point to point, and it is this fact that enables the modeling of stars as a smooth distribution, or a phase-space fluid. To this end, we rely on a distribution function, $f(\vec{x}, \vec{v}, t)$, in order to describe the positions and velocities of stars at some time, t. However, instead of painstakingly describing the orbital trajectories of every last star of the hundreds of billions of stars in the Milky Way, we instead opt for a probabilistic description through this distribution function (Binney and Tremaine, 2008). In essence, f describes the probability density of finding a star in a galaxy with a position in some small volume $d^3\vec{x}$ and within some small region of velocity space $d^3\vec{v}$, at some particular time.

With the view of a Galaxy's stars as a phase-space fluid, one can, in some contexts (Gardner, McDermott, and Yanny, 2021), employ the statistical mechanics workhorse known as the Collisionless Boltzmann Equation, or Vlasov Equation (Binney and Tremaine, 2008). The Collisionless Boltzmann Equation is written below in Eq. 2.1:

$$\frac{\partial f}{\partial t} + \vec{v} \cdot \frac{\partial f}{\partial \vec{x}} - \vec{\nabla}\Phi \cdot \frac{\partial f}{\partial \vec{v}} = 0. \tag{2.1}$$

Furthermore, Eq. 2.1 makes reference to the galactic potential, Φ, which can self-consistently be solved for as a potential-density pair when the Poisson Equation (Eq. 2.2) is also considered:

$$\nabla^2\Phi = 4\pi G \int f(\vec{x}, \vec{v})\ d^3\vec{v} = 4\pi G\rho(\vec{x}). \tag{2.2}$$

Here, $\rho(\vec{x})$ defines the spatial distribution of the stars only, with velocity information having been integrated out:

$$\rho(\vec{x}) \equiv \int f(\vec{x}, \vec{v})\ d^3\vec{v}. \tag{2.3}$$

As one might notice, the fewer coordinates on which f and Φ depend, the simpler the math becomes. By assuming a symmetry, or equivalently that f and Φ are not functions of a particular coordinate, the number of terms in Eq. 2.1 are reduced.

As a particular example of a symmetry, f is often assumed to be axially symmetric given the approximate disk-like shape of our Galaxy. In this case, the distribution function does not depend on the azimuthal coordinate ϕ. Another symmetry that is often employed as a simplifying assumption is the existence of North-South reflection symmetry, or that f is an even function of z, the height above the Galactic mid-plane. Such an assumption is rooted again in the disk-like geometry of the Galaxy. Explicit tests of both of these symmetries are detailed in later chapters, though it is worth mentioning that obvious departures from these symmetries exist (e.g. spiral arms as detailed by Reid et al. (2019)), and it has been suggested that they could be considered as mere "decorations" (Binney, 2017) sprinkled upon an underlying model which bears the symmetries above.

Of course, this is not to say that assumptions of symmetry are inherently bad or made purely for mathematical ease. No, the assumption of axial symmetry and reflection symmetry are at least approximately supported by the data. However, by explicitly exploring these assumptions and near-symmetries, any structures which buck the general trend can be readily detected and studied. Indeed, as is detailed in later chapters, departures from axial and reflection symmetry reveal substantial structure in our Galactic disk.

Furthermore, if the distribution function does not depend on time, there is a steady-state solution to the Collisionless Boltzmann Equation, and thus the first term in Eq. 2.1 may be neglected entirely. This assumption, that a Galaxy is in steady-state, implies that its distribution function in stars does not change appreciably with time. Of course, Galactic timescales are often measured in Myr or Gyr[1], so that we have no hope of just waiting around to check this assumption, and thus other methods must be employed (a novel method is outlined in later chapters).

In addition to steady-state and symmetry assumptions, stars in the Galaxy are assumed to be non-correlated. That is, the probability of finding a star in a specified region of six-dimensional phase-space, $p_1 = f d^3x_1 d^3v_1$, and the probability of finding a star in some other region of that phase-space, $p_2 = f d^3x_2 d^3v_2$ should simply be multiplied to yield the probability of finding the two stars in the particular regions of phase-space (here f is the one-particle distribution function). To wit, the events should be entirely independent of one another. Put another way, the probability of finding a star in a particular region of phase-space should not influence the probability

[1]The crossing time, or the time for a star to move across the Galaxy, is some 100 Myr, while the relaxation time, or the time required for a star to undergo velocity changes roughly equal to the magnitude of its velocity vector, is older than the age of the universe (Binney and Tremaine, 2008).

of finding another star in some region of phase-space. In practice, the assumption of non-correlated stellar data is implemented by assuming the N-particle distribution is "separable," and by extension, that an average of the one-particle distribution function is reliable enough to provide an assessment of a particular observable (Binney and Tremaine, 2008). Here, it is important to note that "separable" describes the nature of the N-particle distribution function, $f^{(N)}$, in terms of one-body densities, f, as encoded in Eq. 2.4.

$$f^{(N)}(\vec{x_1}, \vec{v_1}, ..., \vec{x_N}, \vec{v_N}, t) = \prod_{i=1}^{N} f(\vec{x_i}, \vec{v_i}, t) \tag{2.4}$$

The assumption of non-correlated stellar distributions is obviously wrong for stellar clusters and binary stars, as gravity certainly holds significant sway amongst stars in bound clusters, but it is nonetheless employed for the bulk of the Galaxy. Indeed, away from these stellar clusters, e.g., one can expect the non-correlated assumption to hold as the force from a single star on another nearby star should be much smaller than the force from the rest of the Galaxy because of the long ranged nature of the gravitational force (Binney and Tremaine, 2008; Kardar, 2007), and this physics is the basis for the effective potential in the Collisionless Boltzmann Equation (Kardar, 2007; Binney and Tremaine, 2008). This assumption is tested on the nearby Galaxy in a later chapter.

Altogether, these simplifying assumptions of Galactic dynamics have been necessary to gain an analytic foothold in the complex arena of the dynamics of the Milky Way. Moreover, the models gleaned from theoretical means have been successfully deployed as simple models of the Milky Way when appropriate. However, in the age of growing data sets, the astrophysics community is now able to highlight the differences between the simplistic models and the real data unlike ever before, resulting in interesting and novel insights into the dynamics and structure of the Galaxy. Indeed, we can now go beyond simply stating that a model is insufficient and instead focus on the precise profile or nature of that insufficiency in order to pinpoint probable sources of structure, perturbations, or other effects.

Chapter 3 The Galaxy's Matter Distribution

3.1 Theoretical Models and Their Associated Symmetries

The various components of the Milky way are all modelled through different density profiles. These components, including the thin disk, the thick disk, the central bulge, central bar, and the halo, all tend to be modelled by employing the assumptions outlined in the previous sections. That is, many models have built-in symmetries against which we can compare the data, potentially isolating more interesting effects. As such, it is important to outline a selection of models often used in descriptions of our Galaxy.

Throughout this dissertation, a number of coordinate systems will be used. In what follows, (x, y, z) will denote Cartesian, Galactocentric coordinates, with the origin at the Galactic Center (GC), x extending from the GC away from the Sun, z increasing towards the Galactic North Pole, and y suitable to a right-handed coordinate system. Moreover, Galactocentric cylindrical coordinates will be employed, with R denoting the in-plane Galactocentric radius, ϕ the Galactocentric azimuth, which is zero at the positive x-axis, and z the same as above. Standard solarcentric coordinates will also be used later in the thesis, with l being the solarcentric longitude, defined as zero toward the GC, while b is the solarcentric latitude, increasing to 90 degrees towards the North Galactic Pole, and is zero at the mid-plane.

The Galactic Disk

The galactic disk is often modelled via a few different density profiles (Kuzmin, 1956; Miyamoto and Nagai, 1975, e.g.), and often includes both a thin and thick disk component (Bensby, Feltzing, and Oey, 2014) on account of the kinematic and chemical differences of stars at greater heights (Yan et al., 2019, e.g.). The radial dependence of the disk's density profile is almost ubiquitously described by an exponential decay function with radial scale length R_s. Crudely, the falloff in density in the vertical direction can also be described with an exponentially decreasing form with scale height z_s, yielding a simplistic model:

$$\rho_{disk}(R, z) = \rho_{0_{disk}} e^{-R/R_\mathrm{s}} e^{-|z|/z_\mathrm{s}}. \tag{3.1}$$

The exponential disk model, however, yields a cusp at $z = 0$ and is thus unphysical when modelling the Galaxy near the mid-plane. A more physical solution which satisfies the Poisson Equation and Collisionless Boltzmann Equation comes from Spitzer Jr. (1942), resulting in a vertical profile that goes as the hyperbolic secant squared as a function of z, avoiding any discontinuities in the density gradient near $z = 0$. Tacking on the same radial exponential decay, we arrive at a popular model for the Milky Way disk:

$$\rho_{disk}(R, z) = \rho_{0_{disk}} e^{-R/R_\mathrm{s}} \mathrm{sech}^2\left(\frac{z}{z_\mathrm{s}}\right). \tag{3.2}$$

This distribution is sometimes superimposed with another hyperbolic secant squared function in order to model the thin and thick disks simultaneously, albeit in an ad hoc manner. In this case, the thin disk may be described by some scale height z_{thin} and the thick disk by z_{thick}. The fractional contribution of the thick disk component is tuned via the f parameter in the form:

$$\rho_{disk}(R,z) = \rho_{0_{disk}} e^{-R/R_s} \left(\text{sech}^2 \left(\frac{z}{z_{\text{thin}}} \right) + f \text{sech}^2 \left(\frac{z}{z_{\text{thick}}} \right) \right). \tag{3.3}$$

Separate radial scale lengths for each disk component may also be employed.

Next, in what will turn out to be from the same family of solutions as some of the halo distributions detailed in a later subsection, the Miyamoto-Nagai Disk (Miyamoto and Nagai, 1975) can model the Galactic Disk with a radial scale length, a, a vertical scale height, b, and a total mass parameter, M. For compactness, the potential half of this particular potential-density pair is given in Eq. 3.4, with the density derivable via the Poisson Equation.

$$\Phi_{\text{disk}}(R,z) = \frac{GM}{\sqrt{R^2 + [a + \sqrt{z^2 + b^2}]^2}} \tag{3.4}$$

While this dissertation is not meant to be a complete compendium of density profiles which describe the disk, it is important to note the underlying assumptions and symmetries of some common forms. In Eqs. 3.1, 3.2, 3.3, and 3.4, none of the models have explicit ϕ dependence, speaking to axial (or azimuthal) symmetry. Further, all of these disk models encode a reflection symmetry from $z \to -z$; that is, $\rho_{\text{disk}}(R,-z) = \rho_{\text{disk}}(R,z)$. More colloquially, one might say the models are North-South symmetric, i.e., they are reflection symmetric about the Galactic mid-plane.

Now, of course, the Galaxy has a few structures which are not axially symmetric, including the spiral arms and the Galactic Bar, but away from the Galactic Center and a couple hundred parsecs away from the mid-plane (Reid et al., 2019), assumptions of axisymmetry are employed almost ubiquitously. Another feature of the Milky Way disk, the Galactic Warp (e.g. Skowron et al., 2019), breaks both axial symmetry as well as reflection symmetry, and will be discussed further in later sections. Regardless, it is precisely because of the breaking of expected symmetry that these features are studied so intently, as the particular patterns of symmetry-breaking may encode dynamical effects.

The Galactic Dark Halo

Spiral galaxies like our own are generally enveloped in a voluminous halo of matter which governs much of the Galaxy's dynamics away from the Galactic Center and the mid-plane. Indeed, dark matter is thought to reside in this halo, along with stars, as evidenced by the rotation curve studies of Rubin and Ford Jr (1970) which indicate a large mismatch between gravitationally inferred matter and luminous matter. Due to the distances involved to the halo stars, the immense size of the inferred halo (Deason et al., 2020), and the comparatively fewer halo stars available for study,

the nature of the halo is a source of much disagreement in the literature. Indeed, Eggen, Lynden-Bell, and Sandage (1962) suggest that the halo collapsed from an over-dense region of gas along with the formation of our disk and thus possesses an angular momentum vector that is aligned, more or less, with the disk's. On the other hand, Searle and Zinn (1978) posits that the Galactic halo is likely built out of an accumulation of accretion events over the course of cosmic time. In the latter, much more likely (Helmi, 2020) view, a cacophony of previous merger events and tidal disruptions have populated the halo orbits in the Milky Way, specifically in a way that may leave rogue clumps of dark matter or streams of stars careening through the halo. A hybrid of these views is also possible (Norris, 1994; Beers et al., 2012), with a smoother component and a potentially clumpy matter component, with the former being in-situ and the latter being built from accretion events, though even in situ dark matter could potentially retain clumpy substructure in a Cold Dark Matter model.

Regardless of the particular view of the Galactic halo, the simplest models are all spherical in their geometries. Indeed, simulations of dark matter and galaxy formation tend to favor two power density profiles at large and small radius, yielding a family of equations (Binney and Tremaine, 2008) for modelling the halo:

$$\rho_{\text{halo}}(r) = \frac{\rho_0}{(\frac{r}{r_s})^\alpha (1+\frac{r}{r_s})^{\beta-\alpha}} \tag{3.5}$$

where r is the radial spherical coordinate, r_s is the halo's radial scale length, and α and β both control which particular power laws are chosen to model the halo.

One such member of this family of profiles is the Hernquist Sphere (Hernquist, 1990), for which $\beta = 4$ and $\alpha = 1$:

$$\rho_{\text{Hernquist}}(r) = \frac{\rho_0}{\frac{r}{r_s}(1+\frac{r}{r_s})^3}. \tag{3.6}$$

Further, the Navarro-Frenk-White Halo (Navarro, Frenk, and White, 1997), or NFW profile, belongs to this family of models as well, with $\beta = 3$ and $\alpha = 1$ and is a common choice (Klypin, Trujillo-Gomez, and Primack, 2011), because it has observational support, for modelling the Dark Matter halo:

$$\rho_{\text{NFW}}(r) = \frac{\rho_0}{\frac{r}{r_s}(1+\frac{r}{r_s})^2}. \tag{3.7}$$

Regardless of the particular form of halo model chosen above, one may notice that spherical symmetry is manifest. That is, all of the above halo models depend only on r, and are thus invariant under any rotation of the azimuthal angle ϕ or polar angle θ. Some halo models, on the other hand, do indeed allow for flattening or distortion of the halo, but tend to commit to a common z-axis parallel to that of the disk's (see, e.g., Vera-Ciro and Helmi (2013), Johnston, Law, and Majewski (2005), and Helmi (2004) for oblate models and Posti and Helmi (2019) and Banerjee and Jog (2011) for prolate). In these aligned halo models, the halo may be "flattened" into an oblate geometry (i.e., an ellipsoid with two, identical major axes and one minor axis), or

"stretched" into a prolate one (i.e., an ellipsoid with one major axis and two, identical minor axes).

More recently, Erkal et al. (2019) fit the Milky Way halo via a distorted NFW profile which allowed the symmetry axis of the non-spherical halo to be an outcome of the fit. That is, they did not simply choose the z-axis of the disk to be the special axis of the halo, they instead let the data inform the orientation of the model halo. Specifically, Erkal et al. (2019) determined the shape of the Milky Way halo by examining the effects of the Large Magellanic Cloud system on the Orphan Stream, whilst accounting for the reflex motion of our Galaxy (Erkal et al., 2021). In doing so, they arrived at best fit models for oblate, spherical, and prolate geometries, though the prolate model which accounted for reflex motion was their best overall fit. By allowing the distorted halo orientation to be unaligned with the disk's z-axis and fitting such a geometry with an analytic form, Erkal et al. (2019) explicitly encoded symmetry-breaking effects into their model, offering us an excellent opportunity to compare our direct study of axial and reflection symmetry in our Galaxy with that of their model. The particular profiles of axial symmetry-breaking and reflection symmetry-breaking we have found will be analyzed in later chapters in light of this newer model for the Galaxy's halo.

Other Components of the Galaxy

Although this dissertation focuses primarily on the disk and halo of the Galaxy, it bears mentioning that the Galaxy also possesses a central bulge and a central bar as well, along with a dust and gas component, with the dark matter almost entirely residing in the halo. As gas and dust make up a small fraction of the Galaxy's mass, and thus play a very minor role in the dynamics of the Milky Way, these components will largely be ignored in this document, save for their potential effects on observations later on.

The Galaxy's central bulge can be modelled as a Hernquist sphere (Hernquist, 1990), which as we saw previously can double as a model of the halo as well. The Galpy library, a library for galactic dynamics, also models the central bulge as a power-law density distribution with an exponential cut-off (Bovy, 2015). While both of these models are spherical in nature, it has been suggested that the bulge is actually "boxy" in shape (Dwek et al., 1995), or potentially "peanut" shaped (Li and Shen, 2012).

Furthermore, Robin et al. (2012) show that the best fits to the central region require two separate triaxial components, suggesting the existence of both a boxy bulge and a central bar like that first found by Blitz and Spergel (1991). The bar (and long axis of the triaxial bulge) are thought to point roughly 13-33° away from the $\phi = 180°$ ray, in the region where $90 < \phi < 180°$ (Robin et al., 2012; Portail, 2016). Outside of the extent of the bar, the bar's potential is often modelled by a quadrupole potential of the form (Dehnen, 2000):

$$\Phi_{\text{bar},\ R>R_\text{b}} = -A \left(\frac{R_\text{b}}{R}\right)^3 \cos(2(\phi - \Omega_\text{p} t)), \tag{3.8}$$

where A describes the relative strength of the bar's potential relative to one's chosen model for the Galaxy, $\Omega_{\rm p}$ is the bar's pattern speed, and $R_{\rm b}$ is the in-plane radial scale length of the Galactic bar. Here, the bar's $m = 2$ symmetry[1] is explicit in the argument of the cosine factor, and the potential is time dependent, an important fact to note for axial symmetry breaking and steady-state assumptions respectively. If the Galactic bulge is indeed peanut shaped, the central region of our Galaxy could have significant $m = 2$ and $m = 4$ components, as depicted in Fig. 3.1, which will have important ramifications for our study of resonances of the Galactic bar later on, which we discuss in Chapter 7.

Although gas and dust make up a small fraction of the Galaxy's mass, it is worth highlighting where it is in relation to the features we study, as extinction and reddening can influence various measurements. For the most part, the dust is confined to about 100 parsecs from the mid-plane (Drimmel and Spergel, 2001). The stellar scale-height of the spiral regions, which can be traced with the Galaxy's dust (Kh et al., 2018), is similar to that of the dust (Drimmel and Spergel, 2001), as is the scale height of HI gas near the solar circle (Kalberla and Kerp, 2009). As motivated a bit more later on, cutting away the data in the 200 parsecs closest to the mid-plane effectively eliminates these components from our analysis, where we note that Reid et al. (2019) finds spiral arm widths of about 200-300 parsecs (i.e. heights of 100-150 pc).

Putting the Pieces Together

With the above components in mind, we can begin to piece everything together in order to get a better picture for how the Galaxy looks. Of course, any model will fail to describe the data perfectly, but again it is precisely the differences we wish to highlight in later chapters. Not unlike the subject of a bas-relief sculpture standing out amidst a smooth background, the effects we search for stand out against the above models. To that end, it is pertinent to take a brief look at a simple model for the Galaxy, while keeping in mind that we will focus specifically on the solar neighborhood[2].

The Galaxy has a total mass of around $\sim 0.8 - 1.0 \times 10^{12} M_\odot$ (Ablimit et al., 2020; Erkal, Belokurov, and Parkin, 2020; Deason et al., 2021; Bovy, 2015), with around $6 \cdot 10^{11} M_\odot$ within 100 kpc (Deason et al., 2021), though results in the literature use different methods, populations of stars, and sample volumes (Erkal, Belokurov, and Parkin, 2020). Of this, around $7 \cdot 10^{10} M_\odot$ is due to the disk, while the bulge and bar make up a very small fraction (Bovy, 2015). The majority of the mass is thus in the halo, which can substantially affect the dynamics of the disk and ensures

[1] For this dissertation, we will use the notation m for the azimuthal "mode number," which describes the angle through which one must rotate a system to restore its original orientation. This rotational invariance is described by $360°/m$, so a system with $m = 4$ symmetry will possess rotational invariance for rotations of 90°.

[2] We define the solar neighborhood as roughly the region within a couple kiloparsecs from the Sun's location: $(x, y, z) \approx (-8, 0, 0)$ kpc., though we note that recent refinements from Abuter et al. (2019) resolve the sun's position to a much finer degree: $x \approx -8.178 \pm 0.026$ kpc.

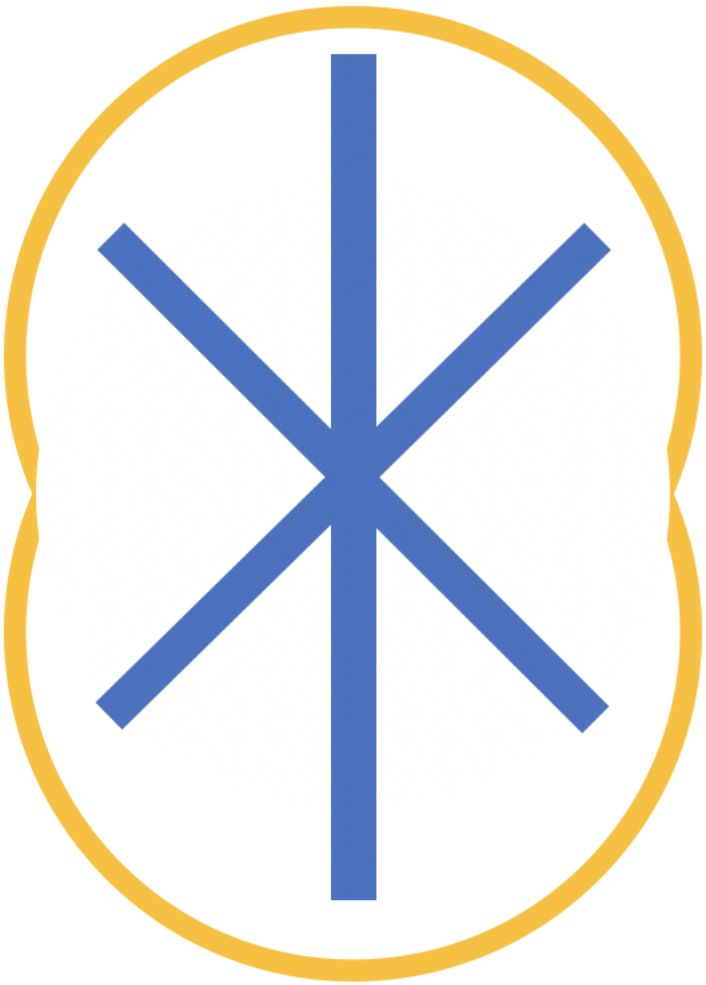

Figure 3.1: The $m = 2$ (bar), and $m = 4$ (x-shape) components of the potential can add up to a peanut-shaped Galactic Bulge (orange).

its stability (Ostriker and Peebles, 1973), and note evidence for the halo comes from measurements of the rotation curve (Rubin and Ford Jr, 1970; Sofue and Rubin, 2001; Eilers et al., 2019; Mróz et al., 2019, e.g.), and the warping of the disk (Skowron et al., 2019; Chen et al., 2019b; Djorgovski and Sosin, 1989; Kerr, 1957; Burke, 1957).

It is worth noting that the bulge has a scale radius of around ~ 1 kpc, and it can be safely ignored in the solar neighborhood. As a pure quadrupole, the bar's potential at the solar circle is some $\left(R_\mathrm{b}/R_0\right)^3 \sim 0.2$ times smaller than at the edge of the bar region, on top of an already small contribution to the mass of the Galaxy within the solar circle. Nonetheless, the bar still represents a large enough contribution to the potential in the solar neighborhood to be important in some cases, and resonant orbits can exist as well, greatly magnifying the Galactic center contribution as a result. Due to the difficulty of modelling resonant structure, due to its sharp features, this dissertation will instead opt to search for structure beyond simple disk-and-halo

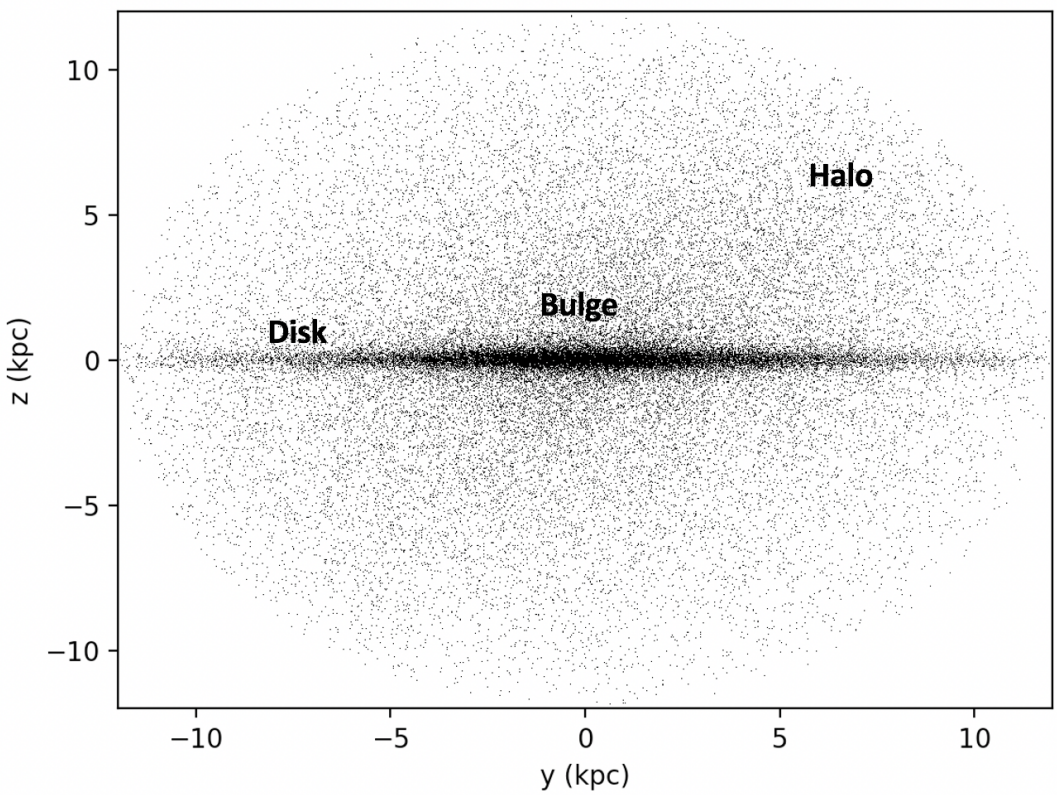

Figure 3.2: A simple model for the Milky Way illustrates the various stellar components of our Galaxy. This $y-z$ projection shows a Miyamoto-Nagai disk (Miyamoto and Nagai, 1975) centered on $z = 0$, a faintly perceptible bulge in the ~ 1 kpc closest to the origin, modelled as a Hernquist Sphere (Hernquist, 1990), and a distorted NFW halo (Navarro, Frenk, and White, 1997; Erkal et al., 2019). The Galactic bar, spiral arms, gas, and dust are not pictured. Note also that the abrupt cut-off at $\sqrt{y^2 + z^2} < 12$ kpc has been imposed for illustrative purposes only.

models in an effort to constrain the pattern speed of the Galactic bar. For illustrative purposes, Fig. 3.2 shows a simple view of the Milky Way, modelled as a Miyamoto and Nagai (1975) Disk, Hernquist (1990) central bulge, and a modified Navarro, Frenk, and White (1997) halo (Erkal et al., 2019). As this dissertation will highlight, this relatively simple picture does not fully capture the array of smaller structures which exist in our Galaxy, and these departures will yield insights into the history of the Milky Way.

3.2 Tools for Probing the Galaxy's Matter Distribution

In our quest to learn more about the structure and dynamics of the Galaxy, astronomers have typically observed a number of stars and either fit various fit forms to the data (e.g. Jurić et al., 2008), effected a clustering analysis (e.g. Borsato, Martell, and Simpson, 2019), or plotted the data in various parameter spaces (e.g. Antoja et

al., 2018) in such a way as to highlight an anomaly or effect of interest. Heretofore, these processes have uncovered a bounty of dynamical effects and significant structures, and these methods presumably will continue to uncover interesting finds as available data proliferates. However, it is likely that not all effects can be unearthed in our galacto-archaeological dig of the Milky Way by using a limited tool set. To this end, this dissertation will develop new techniques for uncovering structure in the Galaxy.

Measuring Asymmetries in the Milky Way

Asymmetries are of great interest in nuclear and particle physics, because they are exquisite probes of fundamental and/or beyond-Standard-Model physics, as illustrated in the famous polarized electron-deuterium deep inelastic scattering experiment at SLAC, which proved that parity symmetry is broken by the electroweak neutral current (Prescott et al., 1978; Hoddeson et al., 1997). While perhaps only somewhat recently introduced to astronomy and astrophysics (Widrow et al., 2012; Yanny and Gardner, 2013), the measurement of an asymmetry is a powerful tool in discovering structure in the Milky Way. In particular, asymmetries are useful in showing differences in one part of the Galaxy versus another, and are normalized by the number of stars participating in the effect so as to account for differing amounts of data as so often is the case in observational scenarios.

As an illustrative example let us suppose a system is Left-Right symmetric along some generic direction, η. That is, we suppose this system should be the same on the left of some symmetry line (say $\eta = 0$) and the right of that line. To compute any departures from this symmetry, we can employ the asymmetry observable, $\mathcal{A}$:

$$\mathcal{A} = \frac{N_{\rm L} - N_{\rm R}}{N_{\rm L} + N_{\rm R}}, \tag{3.9}$$

where $N_{\rm L}$ is simply the number of stars on the left of the symmetry line in question, and $N_{\rm R}$ the number of stars on the right. This can be generalized to other asymmetries, including reflection symmetry and axial symmetry. Eq. 3.9 need not necessarily be measured in bulk for a system. In fact, one may explore the particular "profile" of the asymmetry observable by examining how close to (or far from) symmetry the system is for some small volume on the left of the symmetry line, $d^3r_{\rm L}$ and a matching volume on the right $d^3r_{\rm R}$. Such an examination of the asymmetry lends itself to a different way of thinking about the asymmetry observable: the asymmetry profile $\mathcal{A}(\eta)$, which describes the precise pattern of symmetry-breaking should any symmetry-breaking exist.

The idea of an asymmetry profile is of particular interest to astronomy, as a nearly-axially-symmetric system may have some non-axially-symmetric structures sprinkled throughout it which could conceivably be detected in bas-relief against the symmetric backdrop via the study of asymmetries. In practice, asymmetries in the Milky Way can be computed to test North-South reflection symmetry as a function of z, or to test azimuthal symmetry as a function of Galactocentric longitude, ϕ.

Noether's Theorem and the Galaxy

In what will tend to be a recurring motif throughout this dissertation, tools from small-scale physics (e.g. nuclear and particle) can be applied with success at Galactic Scales. Perhaps the most famous of these tools is Noether's Theorem (Noether, 1918). Noether's Theorem states that any differentiable symmetry in nature is accompanied by a corresponding conservation law or integral of motion. Further work by Olver (1993) proves that the converse of Noether's theorem holds for special cases where the corresponding integral of motion is non-zero.

Now, continuous symmetries may seem a bit irrelevant in astrophysics at first glance, but the Galaxy is modelled via distribution functions which solve the collisionless Boltzmann Equation and Poisson Equation, underpinned by the phase-space-fluid nature of the Galaxy's stars. To wit, the distribution of stars is modelled as continuous, and so one can apply Noether's Theorem at Galactic scales. In the case of the Milky Way, the angular momentum about the z-axis, L_z, is an integral of motion, and this corresponds to axial symmetry. Moreover, the axisymmetric Galaxy possesses a third, non-analytic integral of motion and in certain special cases, the integral can be taken as the energy of vertical motion, E_z, (Binney and Tremaine, 2008).

Armed with the insights of Noether (1918) and Olver (1993), one can examine the axial symmetry of the Galaxy as a probe of the quality of the conservation law for L_z. In other words, the asymmetry observable of the previous section can thus be used to investigate if L_z can be used as an integral of motion for the Galaxy. Failure of axial symmetry of the Galaxy would speak to external torques on the Milky Way, and the precise pattern of the symmetry breaking can help to identify the most likely culprits.

A Milky-Way-Adapted Two-Point Correlation Function

The two-point correlation function (2PCF) has been widely used as an essential probe of structure in condensed matter and nuclear physics, e.g., and has a long-established history in extra-galactic astrophysics as a probe of Dark Matter mega-structure. To date, however, the 2PCF has been employed to only a very limited extent to probe structure in our Galaxy, and assumptions of spherical symmetry have carried over to existing studies (Kamdar et al., 2020; Lancaster, Belokurov, and Evans, 2019), sweeping some nuances of the 2PCF under the rug, so to speak. For example, Kamdar et al. (2020) finds some evidence of clustering with approximately co-moving stars and interprets this in terms of simulations built to model star formation in the Galaxy. However, by examining only the 3-D distances between stars, information is lost that could conceivably capture the particular clustering geometry as well as interesting dynamical effects. Additionally, Lancaster, Belokurov, and Evans (2019) examines the Milky Way halo with the 2PCF, but does so with only about 40,000 stars and severe survey geometry limitations.

Intrinsically, the 2PCF is a function with vector arguments, and thus one can examine each component separately, each providing an additional degree of insight

to the structure and dynamics of our Milky Way. Further, given the Galaxy's approximate symmetries, it is advantageous to look for structures which may stand out amidst the near-symmetries. In other words, examining each component of the arguments of the 2PCF helps to highlight various excitations and structures in the Galaxy.

While foregoing the spherical symmetry assumption from applications of the 2PCF to extra-Galactic Dark Matter studies, we retain interest in structure from the dark sector. Indeed, a key difference between Cold Dark Matter (CDM), or slowly moving dark matter, and Warm Dark Matter (WDM), or semi-relativistic dark matter, is the existence of structure at small, 10-1000 pc scales (Bose et al., 2016; Nadler et al., 2021; Gardner, McDermott, and Yanny, 2021) – scales to which large, extra-Galactic (Mpc-scale) simulations cannot probe due to computational constraints (e.g. Lewandowski and Senatore, 2017; Lewandowski and Senatore, 2020). By examining structure within our Galaxy, we are sensitive to the precise scales which complement numerical simulations.

Extant structure in the Galaxy need not come from dark matter, however. Indeed, excitations of the Galactic disk (e.g. corrugation patterns or waves), clusters of stars, and stellar streams are all conceivably detectable with some form of a 2PCF analysis. To this end, we adopt the Landy-Szalay Estimator for the 2PCF (Landy and Szalay, 1993; Wall and Jenkins, 2012) and apply it to Milky Way stars:

$$\xi_{\mathrm{LS}}(q_i) = \frac{RR(q_i) - 2DR(q_i) + DD(q_i)}{RR(q_i)}. \tag{3.10}$$

As written in Eq. 3.10, the Landy-Szalay (LS) Estimator is constructed from three separate histograms (RR, DD, and DR), and can be examined for a particular component of the separation vector between two stars, q_i. All of these histograms count the number of pairs of stars which are separated by some distance q to $q + dq$: DD counts these pairs for correlations within our Gaia data set, RR counts the correlations within a mock sample generated via a Metropolis algorithm (Metropolis et al., 1953b), e.g., and DR counts the cross-correlation pairs between the two data sets. The histograms must all be normalized to unit area by dividing them by the total number of pair counts in each (e.g. $RR/(r(r-1)/2)$ for r points in the mock catalogue).

In essence, the LS Estimator measures structures (i.e. recurring star-star separation distances) which are not already captured by the model with which one wishes to compare the data against. Further, since models are often built to describe the data in question, the DR histogram accounts for any cross-correlations between the two data sets, and thus allows the LS Estimator to instead look for additional structure. A perfectly uncorrelated set of data will yield an estimator value of zero for all separation distances.

In this thesis, we extend the implementation of the 2PCF to analyses of structural differences in various locations of the Galaxy in a data driven way. To wit, one may demarcate one particular region of the Galaxy (R) as the data set for the RR histogram instead of a mock catalog, and compare it with a separate part (D) of

the Galaxy for the DD histogram. In this case, the geometries must be identical. In practice, this may look like the following: structure in the northern half of the Galaxy is logged into the DD histogram, while a reflection of the southern half of the Galaxy across the mid-plane is then analyzed for structure which is logged into the RR histogram. Here, the fact that the reflection of the southern data occupies the same volume of space as the northern data ensures that DR is sampling true structural differences in the two data sets and not simply distances between two distinct subsets of data[3]. In order to differentiate the different types of 2PCF analyses, we will refer to comparisons against a mock catalog as Gaia-Model studies and comparisons between two distinct Gaia data sets as Gaia-Gaia studies.

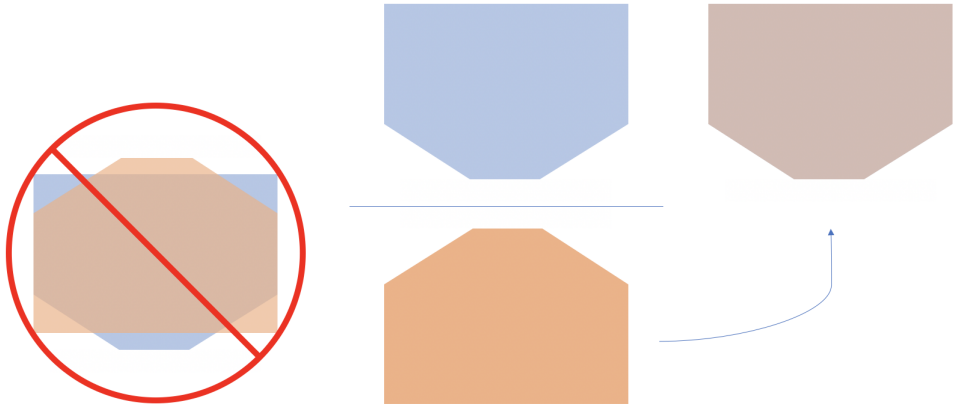

(a) (b)

Figure 3.3: a) When comparing two data sets, it is imperative that their geometries are the same. In this schematic representation, the geometries do not overlap, and so the DR histogram will record separation values at nonsensical scales, delivering results that speak more to the lack of data set overlap than they do actual structure. One can easily see the issue if the base (near the longest side) of the hexagons in this toy model/schematic contains a large number of stars – in this case, how one "overlays" the data sets will determine which scales dominate in the DR histogram, which is clearly not of any physical value. b) To properly compare two data sets, in this case the North (blue) and the South (red), one must reflect the Southern data to match the geometry of that of the North, so that the sample geometries are identical. Upon reflection through a natural symmetry plane, the figure attempts to illustrate perfect overlap by slightly altering the color of the final shape.

Regardless of the particular type of 2PCF analysis we employ, there are essentially two different strategies one can use in a search for structure. First, one can examine as large a sample as computationally practical and attempt to accumulate statistics in order to uncover any persistent, diffuse, ubiquitous structure in the Galaxy. This,

[3]Effects like the Galactic warp may slightly bend the disk to the point that our nominally symmetric data sets as defined in a non-warped system will actually sample slightly different regions of the Galactic matter distribution. Such an effect is small, though, as we discuss later.

of course, is very computationally intense and can miss more localized structures if they are dwarfed by the sheer size of the rest of the data set.

Alternatively, a 2PCF analysis may instead search for diffuse but still somewhat localized structure via a sector-by-sector approach. Not unlike a grid search in an archaeological dig site, this approach can better uncover variations in structure from sector to sector. By dividing the data set up into smaller chunks, this method is computationally quicker, as the number of pairs in a sector goes roughly as $(N/M)^2$, the total number of stars divided by the total number of sectors into which one divides the data. Doing this for M different sectors yields a process that results in N^2/M pairs to consider. However, while reducing the total computational requirements by a factor of M, this approach necessarily prevents study of correlations between stars in separate, presumably arbitrarily chosen bins. Both strategies have their own advantages and disadvantages and thus both will be employed in this dissertation.

In particular, it is interesting to note that Gaia-Model 2PCF comparisons may allow for sequentially finer structure probes. To wit, once a structure is discovered, that structure could then potentially be folded into the model so that its effect is effectively erased in subsequent data vs. model studies, allowing for the potential discovery of even finer structures. Indeed, this is demonstrated in Fig. 3.4 via a fit to the vertical wave structure in the Milky Way, allowing one to search for other structures. This feature of the Gaia-Model comparisons is due to the fact that the LS Estimator practically ignores any structure that is already present in the model as it is accounted for in the DR and RR histograms.

Comparing the data with a mock catalogue of stars does come with a number of pitfalls, however. Because the LS Estimator in this case compares the structural differences of the data with a model, the model obviously has to be reasonable. Nonetheless it bears saying that the LS Estimator would of course suggest structural differences if, to use a condensed matter example, graphene's hexagonal geometry is compared against a model of a cubic lattice. The same is true in astronomy – if the model does not describe the data sufficiently well, any non-zero values of the LS Estimator may speak only to the poor quality of fit, and not to any real structure.

Because of this, one must take great care to model the Galaxy as well as realistically possible in order to be sure that any possible underlying structure inferred from the analysis is not merely a sign of a poor fit. However, this very fact may lead to yet another possible pitfall of the Gaia-Model 2PCF method: fitting a sample of data to a model of such a high degree may result in "absorbing" any structure one wishes to find into the model! If this is indeed the case, the Gaia-model 2PCF analysis will fail to find that particular structure.

To avoid this "over-fitting" dilemma, it may useful to fit a larger swath of data all at once, allowing differences in the average best-fit model to help highlight structural differences throughout the Galaxy. However, as we detail later in this document, there is a huge variation in fit-forms across the Galactic plane, and by choosing a model which does not describe each individual wedge of data well, a non-zero result in the LS Estimator could result in ambiguities as to whether the non-zero result is due to actual structure or simply a poor fit to the local data. For example, Bland-Hawthorn and Tepper-Garcıa (2021) suggest that a combination of density waves and bending

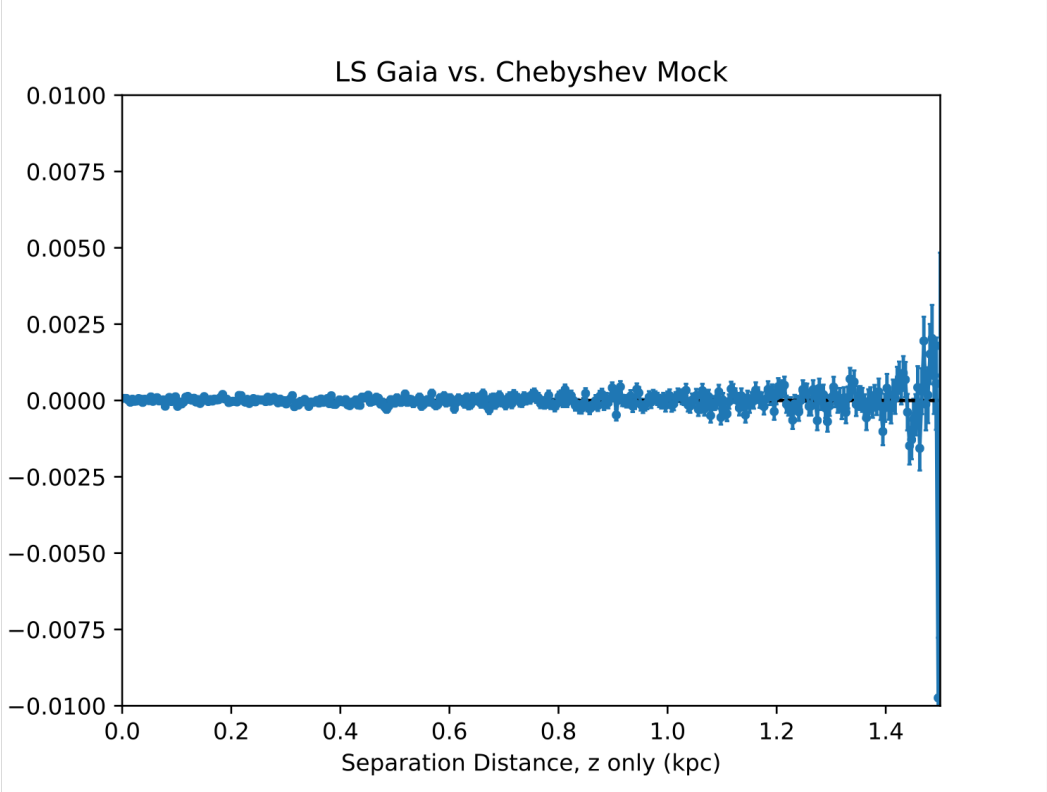

Figure 3.4: A Gaia vs. Model 2PCF comparison illustrating structural differences between the vertical profile of the Milky Way disk, which is known to have wave-like density perturbations, and a model designed to incorporate that waviness. The wave-like perturbation is captured via a 32-degree Chebyshev polynomial fit. With the waves fit to an extremely accurate degree, no structure appears, even though the vertical waves are known to exist in the region. This fact illustrates the ability of the 2PCF to absorb known structure and make way for the detection of finer structure, should it exist.

waves could create complicated corrugation patterns in the Galaxy, which may be difficult to fit correctly. Regardless, employing the 2PCF should be a powerful test of the suggested effects.

Chapter 4 Structures and Findings in the Galaxy

As more and more reliable data becomes available via astrometric surveys, the astrophysics community's understanding of the Galaxy has evolved away from a galaxy similar to that of the simple models outlined in chapter 3. Instead of a well-behaved, razor-thin disk and a spherical halo, the Milky Way is undeniably more complicated: there are waves, warps, and regions of over- and under-densities, and various components of the Galactic potential are not necessarily symmetric or aligned. Invariably, this complicated Galactic landscape has given rise to numerous disagreements on an array of different measurements (e.g. the pattern speed of the bar). In this chapter, we review the existing literature in an effort to place the work in this thesis into context.

4.1 Asymmetries in the Structure of the Milky Way

Given that the simple equations often used to model the galaxy have certain manifest symmetries (e.g. the reflection symmetry of a disk), it is interesting to study how these symmetries are actually borne out in the galaxy itself. Do the data match the symmetries we expect? If not, is the discrepancy negligible or significant? What does the profile of the asymmetry tell us about potential causes?

The first such instance of this topic being explored is the work of Widrow et al. (2012) wherein the sub-field of galactoseismology was arguably born[1]. The authors studied the vertical structure of the galaxy and found that an asymmetry exists in number counts near the Sun's location exhibiting a wavelike pattern. The paper suggests that this wave was likely excited by a relatively recent collision event such as a satellite galaxy (e.g. Sagittarius) or a Dark Matter subhalo passing through the disk. Recent simulation work by Bennett, Bovy, and Hunt (2021), though, seems to suggest that the most recent Sagittarius impact alone could not have caused the observed asymmetries, agreeing with the analysis of Chequers, Widrow, and Darling (2018). Bland-Hawthorn and Tepper-Garcıa (2021), on the other hand, suggest that the *second* most recent passage of Sagittarius may have been responsible for the phase space spiral (Antoja et al., 2018). The latter agrees with an analysis by Binney and Schönrich (2018), though it is as yet unclear if the phase space spiral and vertical waves are related.

In the wake of this discovery, a number of papers were published confirming the wavelike perturbation of the Galactic disk. Yanny and Gardner (2013) confirmed the asymmetry with a more robust analysis which both boasted a larger sample size, thanks to SDSS DR9 (Ahn et al., 2012), and considered a suite of systematics. Following this confirmation was a more localized study of the disk by Ferguson, Gardner, and Yanny (2017) which showed that the vertical distribution of stars in

[1]For a brief history of galactoseismology, see appendix A of Bland-Hawthorn and Tepper-Garcıa (2021), where it is noted that Iye (1985) first used the term 'Galactic seismology,' while Widrow et al. (2012) introduced the term 'galactoseismology.'

both the North and South varied across the Galactic plane. To wit, the vertical profile of the Galaxy was shown to vary somewhat with both R and ϕ, speaking to possible warping of the disk or variations in $z_\odot$. Additionally, a corresponding North-South asymmetric velocity structure (Widrow et al., 2012) was shown to exist as well (Williams et al., 2013).

Armed with the tremendous numerical size of the *Gaia* DR2 data set, Bennett and Bovy (2018) resolved the vertical waves in the solar neighborhood to the clearest extent yet thanks to astrometric distances. Bennett and Bovy (2018) also brought up the interesting point of determining the Sun's height above the mid-plane, $z_\odot$, in a galactic disk that is locally perturbed away from an equilibrium distribution, particularly in a manner that bears odd symmetry with respect to z. To wit, the even and odd terms in z can change the local maximum of the vertical density profile, an effect which may be difficult to disentangle from what they call the "true" $z_\odot$.

Further study by An (2019) showed that the vertical waves found above correspond to metallicity gradients which also show wavelike patterns. Such a discovery lends tremendous strength to the collision hypothesis offered by Widrow et al. (2012). Indeed, the photometrically-inferred metallicity gradient found by An (2019) implies that disk stars are excited vertically by some 80 pc, as estimated via a photometric distance method.

Given the evidence for variations in the form of the vertical waves from Ferguson, Gardner, and Yanny (2017) across the plane of the Galactic disk, it is natural to wonder if the axial symmetry of the Galaxy is broken. Of course, with features like the spiral arms and a bar, the Galaxy is not perfectly axisymmetric, but away from these objects, how axially symmetric is the Milky Way? This symmetry is precisely what we test in Gardner, Hinkel, and Yanny (2020) and Hinkel, Gardner, and Yanny (2020b) and we will outline the process in greater detail in later chapters.

In short, we have found that the Galaxy is not perfectly axially symmetric, and that the precise pattern of symmetry breaking agrees with a distorted halo model for the Milky Way (Erkal et al., 2019), which might explain the warping of the Galactic disk in both gas (Kerr, 1957; Burke, 1957) and stars (Djorgovski and Sosin, 1989; Skowron et al., 2019; Chen et al., 2019b). Moreover, Noether's Theorem suggests (Noether, 1918; Olver, 1993) that a failure of axial symmetry implies that the angular momentum about the z-axis is not conserved, and thus the Galaxy is subject to an external torque. A quick inventory of the Local Group suggests that the Large Magellanic Cloud (LMC) system is likely responsible (Gardner, Hinkel, and Yanny, 2020), and interestingly, the model that is found to best describe the asymmetry is based on an LMC-induced halo distortion. Ultimately, the asymmetry analysis supports the notion that the LMC may be responsible for the Galactic warp (Weinberg and Blitz, 2006) via this distorted halo (Law and Majewski, 2010).

The above interpretation of the axial asymmetry we find relies on an approximate, hierarchical study of present-day torques on our sample of stars in order to determine which perturber is most likely, in light of Noether's Theorem. Presumably, axial asymmetries could also have been generated in the somewhat recent past, so long as the differential rotation of the Galaxy has not washed out such an effect. Moreover, while very close to the mid-plane, spiral arms may nonetheless hold some sway over

the positions of the stars above or below them, thanks to the gravity from those over-densities. Indeed, Bland-Hawthorn and Tepper-Garcıa (2021) suggest that the Milky Way is experiencing both bending waves as well as density waves, and that significant corrugations exist when these two effects are combined, potentially warping the spiral arms. Such corrugations could conceivably yield the axial asymmetry profile we have found. Such a possibility might be tested by better mapping the corrugation structures.

4.2 A Galaxy Not in Steady State

As motivated in previous chapters, the Galaxy has been widely assumed to be in steady-state, and thus the one-body distribution function, f, does not vary with time. Colloquially, we might say that the stars in the Galaxy have undergone many orbits around the Galactic center and have undulated above and below the plane many times and have thus settled in to steady-state behavior (Binney and Tremaine, 2008). In this view, it is easy to suggest that the existence of objects like stellar streams are evidence of non-steady-state effects – after all, a collision between our Galaxy and another is a time dependent effect. However, stellar streams make up a small fraction of the Galaxy, and it is pertinent to ask if non-steady-state behavior exists more broadly.

This type of "proof" of non-steady-state effects leaves something to be desired in terms of rigor. Indeed, there exists a pattern in the literature of pointing to various effects and claiming non-steady-state effects follow from the complicated nature of some particular, observed pattern in the stars of the Milky Way. For example, the unexpected nature of the "Gaia Snail" discovered by Antoja et al. (2018), reminiscent of phase-mixing (Gandhi et al., 2021), is the quintessential example of this proof-by-complication method. This is not to downplay the incredible find of Antoja et al. (2018) nor is it to say that the Gaia Snail is not indicative of non-steady-state effects (it may well be!), but it is always a good practice to be a bit more rigorous in a proof. To this end, we have determined a more direct way of demonstrating that non-steady-state effects are indeed operative in the Milky Way in Gardner, Hinkel, and Yanny (2020) and Hinkel, Gardner, and Yanny (2020b), which are included herein as chapters 5 and 6.

Enabling the aforementioned direct method is the theoretical work of An, Evans, and Sanders (2017), who prove several theorems and corollaries of galactic dynamics. One of these theorems states that any isolated, axisymmetric system which is in steady state must be reflection symmetric (i.e. North-South Symmetric) about the Galactic mid-plane. To this end, we have shown via the ultra-pure data set of Gardner, Hinkel, and Yanny (2020) and Hinkel, Gardner, and Yanny (2020b) that the magnitude of the Galaxy's axial asymmetry differences in the North minus the South is much larger than the aggregate asymmetry, indicating that reflection symmetry is broken in a manner much more significantly than axial symmetry – an indicator of non-steady-state effects based on the galactic dynamics theorems of An, Evans, and Sanders (2017).

4.3 The Shape of the Galactic Halo

With the realization that the galaxy's rotation curve is not as would be expected for the luminous mass distribution of the disk, it became clear that a spherical or nearly-spherical halo of mostly dark matter was required to explain the observations (Ostriker and Peebles, 1973; Rubin and Ford Jr, 1970; Sofue and Rubin, 2001). However, the halo may not need to be exactly spherical. It is much more analytically tractable, though, to treat it as such, as illustrated in previous sections. Nonetheless, if the halo is not truly spherical, to what degree is it ellipsoidal, how might it be oriented, and is it prolate, oblate, or triaxial?

Given that the halo is thought of as being built by a limited number of significant collisions with our Galaxy (Searle and Zinn, 1978; Bell et al., 2008; Helmi et al., 2018b), it is possible that one or two collisions dominate the orientation of the halo. The recently discovered Gaia-Enceladus or Sausage (Helmi et al., 2018b; Belokurov et al., 2018) and Sequoia (Myeong et al., 2019) galaxies are strong candidates for such dominant collisions, as the mass ratios of the satellites to our Galaxy were around one-fourth at the time of the collision. If the construction of our Galaxy's halo is truly built from a steady cadence of torn apart satellite galaxies in various stages of disruption, not just in situ stars (Di Matteo et al., 2019), and is dominated by a couple of collisions (Mackereth et al., 2018; Fattahi et al., 2019), then it seems reasonable that a perfectly spherical halo is unlikely. Additionally, nearby satellite galaxies tugging on the Milky Way's matter make non-spherical halo geometries all the more likely.

Many attempts have been made to infer the shape of the dark halo. Some of these attempts at examining the halo have made use of velocity measurements of stars which, until quite recently, have been limited in sample size and coverage. Additionally, because of the Sun's position within the galactic disk, confidently identifying a large number of halo stars in all directions has been a rather challenging task. One might easily identify many halo stars out-of-plane, but what about at lower latitudes? If halo stars are thought to contribute $\mathcal{O}(1)\%$ of the stars in the disk (Jurić et al., 2008), false positives and false negatives from the filtering that is necessary to remove disk stars are potentially devastating. Indeed, metallicity is an important discriminant, but spectroscopic data lacks the sheer statistical strength of its astrometric counterpart. A full picture of the geometry of the halo via direct observations is as yet fraught with completeness and stellar identification issues. Nonetheless, Conroy et al. (2021) attempts to examine the shape of the halo, including wakes and its dynamical response with a extremely small sample of 1301 stars at large Galactocentric radii (many tens of kpc from the sun) and find some evidence for a wake behind the LMC. However, given the possible systematics and the extremely low number of stars over such an immense volume, their result is not all that compelling.

Instead, there have been many clever, indirect ways of assessing the shape of the halo in which our disk exists. For example, Helmi (2004) leverage the orbit of the Sgr dSph in order to constrain the ellipticity of the galactic halo by using a modified NFW potential for the halo that includes flattening or elongation along the z-direction. While the author found that the Sagittarius stream is too dynamically

young to trace the halo's potential effectively, they were able to show that both oblate and prolate models were still consistent with the data available at the time.

An N-body study by Law and Majewski (2010) also used the Sgr dSph orbital information in order to infer the shape of the dark halo, and found that a triaxial halo best explains their simulation results. Their favored halo geometry is roughly oblate and shares a common axis with the disk's z-axis, and Law and Majewski (2010) explain that the particular orientation they find may need additional explanation, such as perturbations due to the Magellanic Clouds. Such a finding agrees with recent results (Erkal et al., 2019; Erkal, Belokurov, and Parkin, 2020; Gardner, Hinkel, and Yanny, 2020; Conroy et al., 2021; Vasiliev, Belokurov, and Erkal, 2021).

More recently, Erkal et al. (2019) have included the Magellanic Clouds in their halo fits having fully realized that equilibrium models tend to understate the significant sway the LMC holds upon the Milky Way (Erkal, Belokurov, and Parkin, 2020) halo, as evidenced by bulk motions in the outskirts of the Galaxy. In particular, Erkal et al. (2019) explain the misaligned stream-track motions of Orphan Stream stars via a Milky Way that is responding reflexively to the pull of the LMC, with a dark matter halo that may be oriented freely in space, without the forced assumption of a common axis with the disk. After examining various halo geometries, they find a prolate halo which is more or less pointed at the Magellanic Clouds. Vasiliev, Belokurov, and Erkal (2021) also find that the reflex motion of the Galaxy towards the LMC is important for describing the Sagittarius stream. Erkal et al. (2019) describe the distorted halo's potential in terms of the traditional NFW concentration, c, radial scale length, $r_{\rm s}$, and mass, M:

$$\Phi_{\rm Erkal} = \frac{-GM}{\tilde{r}} \frac{\log(1+\frac{\tilde{r}}{r_{\rm s}})}{\log(1+c) - \frac{c}{1+c}}, \tag{4.1}$$

where a modified version of the spherical radial coordinate is used:

$$\tilde{r}^2 = x^2 + y^2 + z^2 + \left(\frac{1}{q^2} - 1\right)(\hat{n} \cdot \vec{x})^2. \tag{4.2}$$

The form above explicitly breaks axial symmetry, as the unit vector $\hat{n}$ allows the symmetry axis of the oblate or prolate halo (determined by the q parameter), to point in any direction[2].

Interestingly, Vasiliev, Belokurov, and Erkal (2021) offer tantalizing but tentative results demonstrating that the halo may vary radially in its orientation, with an oblate inner halo and a prolate outer halo, even if the 6D data used is limited in number. This is of particular note, as a radially-varying ellipsoidal geometry would allow for the dark halo to warp the Galactic disk in a way that allows for long-lived warps (Dekel and Shlosman, 1983). The Galactic warp (Kerr, 1957; Burke, 1957; Djorgovski and Sosin, 1989; Chen et al., 2019b; Skowron et al., 2019) appears to be oriented in such a way that the line of anti-nodes, or the direction of the most warping, is aligned fairly well with the best fit, reflex prolate halo of Erkal et al. (2019), lending credence to the findings of Weinberg and Blitz (2006) and Ideta et

[2]Note that $\vec{x} = (x, y, z)$.

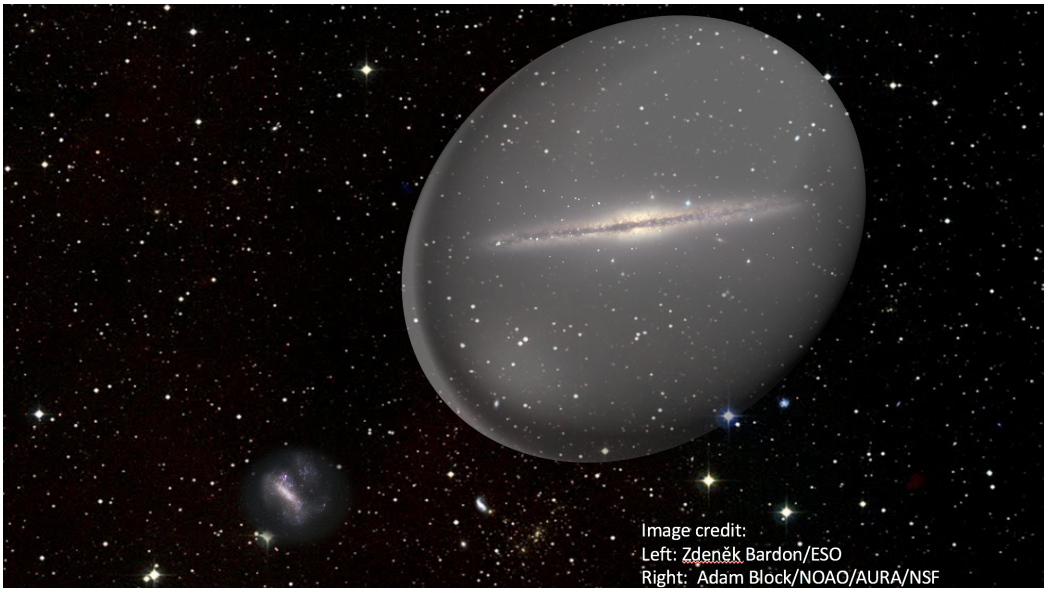

Figure 4.1: An illustration/composite image of the Milky Way halo, encompassing the Galactic disk, pointing in the direction of the Large Magellanic Cloud. The illustration is not to scale, as the Milky Way's Virial Radius is some four times larger than the distance to the LMC. The halo is drawn in this manner to illustrate the alignment of the halo with the LMC as determined by Erkal et al. (2019) and Gardner, Hinkel, and Yanny (2020).

al. (2000), but is in some tension with Vasiliev, Belokurov, and Erkal (2021). As mentioned previously, this halo geometry matches the observed axial asymmetry well (Gardner, Hinkel, and Yanny, 2020), concretely connecting the LMC, the halo, and the warp.

Now, the ellipsoidal models for the halo described above are a start, but the halo may be more complicated still. Indeed, wakes are predicted to exist in the dark matter of the halo on account of dynamical friction, induced by passing objects like the LMC (Chandrasekhar, 1943). To this end, Garavito-Camargo et al. (2019) simulate the Milky Way's dark matter halo subject to an in-falling LMC, and find significant wake structure. Cunningham et al. (2020) quantify the wake structure in velocity space for the simulations of Garavito-Camargo et al. (2019) using spherical harmonics, but note that hypothetical dark substructure may wash out some of the wake.

Moreover, depending on the particular nature of dark matter, there may or may not be entirely dark substructure within the Milky Way's dark matter halo. If dark matter interacts only via gravity and thus does not collapse into the gravitational potential as readily as baryonic matter, any passing satellite tends to shed its dark matter first, potentially leaving trails of dark structure throughout the halo (e.g. O'Hare et al., 2020). Additionally, dark "subhalos" may exist throughout the Milky Way's halo, and their distribution of sizes depends on the mass of the particular subhalo. In fact, the subhalo mass function for Cold Dark Matter (CDM), Warm

Dark Matter (WDM), and Fuzzy Dark Matter (FDM) all disagree at smaller ($< 10^8 M_\odot$) mass (and length) scales (Schutz, 2020, e.g.), and this subhalo mass function is determined by the particular nature of the dark matter candidate, so that structure searches in the Galaxy's halo may help to set limits on various dark matter models. As mentioned previously, a Two-Point Correlation Function analysis comparing the Milky Way halo to a smooth model might help to point to dark matter substructure, helping to clarify which models best describe the structure of the Galaxy. It is also important to note that if the halo is subject to an asymmetry, any dark matter direct detection experiment would have to account for the potentially non-isotropic nature of the dark matter when setting limits, as terrestrial experiments sample only one small volume of the Galaxy (Evans, O'Hare, and McCabe, 2019).

Ultimately, the shape of the Galaxy's halo could be different from that inferred from our axial asymmetry analysis if we are indeed sampling a more local asymmetry due to complex super-positions of different waves (Bland-Hawthorn and Tepper-Garcıa, 2021), as opposed to a global asymmetry. To complicate matters even further, it has been suggested that the Galactic warp could be due to gravitational wakes from the in-fall of Sagittarius (Bailin, 2003). Bar buckling has also been suggested as a warping mechanism (Łokas, 2019). If the warp is indeed not of Magellanic origin as Bailin and Łokas suggest, then our interpretation is less compelling. A potential test of the latter view could simulate bar buckling and determine the duration of the warp. Along with an estimate for the time since a buckling event, this could help provide clarity on whether or not the bar is indeed behind the behavior. As spectra become more widely available, the Sgr in-fall view might be testable as well via a metallicity analysis.

4.4 Resonances of the Galactic Bar

As a brief glance at a review of measurements of the Galactic properties reveals, there is widespread and persistent disagreement as to the precise pattern speed, Ω_p, of the Galactic bar (Bland-Hawthorn and Gerhard, 2016), or how fast the central bar rotates in an inertial reference frame. Because of this wide array of values for the bar's pattern speed, there is also a disagreement regarding the locations of the resonances of the Galactic Bar, including whether or not moving groups near the Solar neighborhood are due to the Outer Lindblad Resonance (OLR) or the Co-rotation Resonance (CR). In what is perhaps a cosmic accident, the rotation curve of the Milky Way just so happens to connect the two problems: if one favors a fast bar ($\Omega_p \gtrsim 40$ $^{\mathrm{km}}/_{\mathrm{s\ kpc}}$), the moving groups near the Solar neighborhood appear to be due to the OLR, while if one favors a slow bar ($\Omega_p \lesssim 40$ $^{\mathrm{km}}/_{\mathrm{s\ kpc}}$), the moving groups appear to be due to the CR, and thus the two camps seem firmly entrenched.

For example, Dehnen (1999) find that the pattern speed of the Galactic bar is about $\Omega_p = 53.3 \pm 3$ $^{\mathrm{km}}/_{\mathrm{s\ kpc}}$ by comparing a velocity distribution bi-modality in nearby stars to bar simulations. Additionally, Monari et al. (2017) also favor a fast bar, with an inferred pattern speed of $\Omega_p \gtrsim 50$ $^{\mathrm{km}}/_{\mathrm{s\ kpc}}$, inferring this value from the Hercules moving group and models of the bar. Indeed, dynamical studies of this kind all seem to point to a fast bar.

On the other hand, direct observations of the Galactic center region suggest a slower bar. For example, Portail et al. (2016) find that dynamical models made to match observations near the bar tend to yield pattern speeds of about $\Omega_p = 39.0 \pm 3.5$ $^{km}/_{s\ kpc}$, while separate, earlier studies found even slower speeds in the vicinity of $\Omega_p = 25 - 30$ $^{km}/_{s\ kpc}$ (Portail et al., 2015). In other words, assessments of the pattern speed span about a factor of 2: a literature review range of $\Omega_p = 43 \pm 9$ $^{km}/_{s\ kpc}$ by Bland-Hawthorn and Gerhard (2016) illustrates this well.

Further complicating the issue and perhaps partially driving the disagreement is the fact that the Galactic center is so densely packed with stars and shrouded by gas and dust. Because of these facts, direct measurements of the bar's pattern speed through astrometric means are challenging due to mounting uncertainties, and Sanders, Smith, and Evans (2019) finds additional systematics of 5-10 $^{km}/_{s\ kpc}$ when one adds in observations of the far side of the Galactic center region. On top of the observational uncertainties, Hilmi et al. (2020) suggests that the pattern speed of the Galactic bar might fluctuate due to attachment and detachment to nearby spiral arms, an effect also suggested by Sanders, Smith, and Evans (2019). In this view, astrometric measurements of the pattern speed would reveal an instantaneous value, albeit subject to systematics, while dynamical inferences would reveal a time-averaged effect (Hilmi et al., 2020).

Our work in Hinkel, Gardner, and Yanny (2020a) offers a novel, model-independent way of assessing the pattern speed of the Galactic bar via the radial dependence of the axial asymmetry (Gardner, Hinkel, and Yanny, 2020), which in the framework of Hilmi et al. (2020) would be a time-averaged assessment of this observable. In Hinkel, Gardner, and Yanny (2020b) and Hinkel, Gardner, and Yanny (2020a) we measure a sign-flip in the axial asymmetry observable and interpret this in terms of the orbital orientation flip associated with resonances of the bar. The sign change observed is consistent with an OLR of the bar, and the radius at which the sign flip is found is then used in conjunction with the rotation curve of Eilers et al. (2019) in order to compute the inferred pattern speed of the bar through indirect means.

This approach is an effort to avoid the observational difficulties of the Galactic center region and also does not necessitate comparing moving groups to computer simulations. However, the measurement relies on the flip in orbital alignments near resonances of the bar, which may be small in magnitude and potentially complicated by other effects including the pattern speed of the spiral arms as well as non-steady-state effects. Indeed, vertical effects from the spiral arms, or perhaps complex corrugations from density and bending waves (Bland-Hawthorn and Tepper-Garcıa, 2021) could potentially be alternative explanations for the vertical-axial coupling we find. Further, the pattern speed assessment relies on an assumption of $m = 2$ symmetry for the bar, but the "boxy-bulge" region of the Galactic center could presumably have a significant $m = 4$ component, leaving the door open to a potential 4:1 resonance. (For reference, higher order OLR resonances are theorized to be at smaller radii than the $m = 2$ OLR, and so both could be detectable with a larger analysis footprint, should they exist). Regardless, the sign-flip observed in the axial asymmetry appears to be inconsistent with a Co-rotation Resonance of the Galactic bar, and so our results favor a faster bar.

Our result is in tension with an analysis by Khoperskov et al. (2019a), which suggests a slower bar with an OLR radius of about 9 kpc. Khoperskov et al. (2019a) use the Gaia Radial Velocity data set and a "guiding coordinate space" analysis to show that distinct ridges exist in the Gaia data when the data is transformed to their guiding coordinate space. Spiral arms and resonances are identified via specific characteristics of these ridges when compared against Milky Way-like simulations and the authors suggest that two of the ridges reveal the locations of the Co-rotation and Outer Lindblad Resonances. Recent work by Hunt et al. (2020), however, suggests that the ridges are actually just moving-groups that are already known to the astronomy community.

Nonetheless, some of these moving groups may still be from resonances, and Laporte et al. (2020) connect a few of the moving groups to various resonances from a slow bar model. Clarke and Gerhard (2021) also attribute various moving groups to resonances, but pair different groups with different resonances than Laporte et al. (2020). Critically, neither analysis models the effects of Sagittarius along with the bar, an effect that can *entirely reverse* velocity structure near the sun (Carrillo et al., 2019). Additionally, Clarke and Gerhard (2021) and Laporte et al. (2020) do not take into account the upward revision and potential time-dependent nature of the pattern speed suggested by Hilmi et al. (2020) and Sanders, Smith, and Evans (2019). The asymmetry analysis in this dissertation presumably absorbs all of these considerations into a time-averaged effect, while also not relying on velocity structure.

More recent results from Trick et al. (2021) uncover a number of resonance candidates in the Gaia data, which seem to indicate that the bar could be either fast or slow, depending on the particular resonance signatures that one interprets as the OLR. The action space analysis of Trick et al. (2021) finds that significant coupling of vertical and radial motions, not unlike those found by Hinkel, Gardner, and Yanny (2020a), might help identify the OLR, but they cannot rule out most of their candidate resonances. Upon adding in phase-angle information for each star in addition to the actions of each star, Trick (2020) claim to rule out a fast bar and thus a relatively close-in OLR radius. This is in tension with our result, and favors an OLR that is in the vicinity of $R = 9 - 11$ kpc.

However, the method of Trick (2020) relies upon measuring a sort of axial asymmetry with a sample that is not uniform on the sky: the Gaia radial velocity data set's completeness varies across the Galaxy, in ways that are not symmetric about the $\phi = 180^\circ$ ray. Trick (2020) dismiss the possibility of incompleteness biasing their assessment of resonant radii by showing that an artificially induced incompleteness of 30% does not change their conclusions, but critically do not consider the precise geometric patterns of any incompleteness on the sky, simply opting for a 30% reduction in the number of stars on one half of the *already* presumably incomplete sample.

Regardless, the richness of ridges in action and angle space, along with the fact that no particular picture could explain all of the ridges found by (Trick et al., 2021; Trick, 2020), seems to suggest that the resonant structure of the Milky Way may be more complicated than previously appreciated. Similarly, Monari et al. (2017) have suggested the need for additional effects, perhaps from spiral arms, in order to reconcile observations, and Hilmi et al. (2020) have suggested a time-varying pattern

speed also due to spiral arm effects. Ultimately, the issue remains very much unsettled, though recent results have seemingly trended toward a fast bar (e.g. Li et al., 2021; Sanders, Smith, and Evans, 2019; Hilmi et al., 2020; Hinkel, Gardner, and Yanny, 2020a), or at the very least a slightly faster slow bar interpretation (Laporte et al., 2020; Clarke and Gerhard, 2021; Trick, 2020) as compared to previous, much slower, slow bar estimates (Portail et al., 2015).

Chapter 5 Applying Noether's theorem to matter in the Milky Way: evidence for external perturbations and non-steady-state effects from Gaia Data Release 2

5.1 Introduction

The stars of isolated galaxies in steady state have distribution functions that obey the Poisson and collisionless Boltzmann (Vlasov) equations and are controlled by particular integrals of motion, as dictated by Jeans theorem (Jeans, 1915; Binney and Tremaine, 2008). In axisymmetric galaxies these integrals include the total energy E and the component of angular momentum parallel to the symmetry axis L_z, and the axially symmetric distribution functions are also reflection symmetric about the galactic mid-plane (An, Evans, and Sanders, 2017). The ubiquity of flat galactic rotation curves (Sofue and Rubin, 2001) are commonly interpreted as galaxies embedded in a spherical halo of dark matter (DM), for which E and $\mathbf{L}$ are also integrals of motion. Here we scrutinize how these expectations are borne out in our Galaxy using observations of stars from *Gaia* Data Release 2 (DR2) (Prusti et al., 2016; Brown et al., 2018).

In our Galaxy, the estimated stellar relaxation time is far longer than the age of the Universe, making the neglect of stellar collisions an excellent approximation. This, in turn, allows us to model the collection of its stars as a continuous mass distribution, as essential to the use of the distribution function (DF) formalism. The continuous symmetries of that mass distribution become key probes of its dynamics, for Noether's theorem links the existence of an integral of motion to that of a continuous symmetry (Noether, 1918; Olver, 1993). Thus to test the extent to which the angular momentum L_z serves as an integral of motion, we can study whether the stellar mass distribution is axially symmetric. Of course the Galaxy possesses features that break axial symmetry, such as spiral arms (Chen et al., 2019a; Reid et al., 2019) or dust (Kh et al., 2018), so that to test axial symmetry we select regions so as to minimize such effects. For example, we avoid the immediate Galactic mid-plane ($z = 0$) region, choosing stars at vertical heights z with $0.2 \leq |z| \leq 3$ kpc, noting that the the dust has a vertical scale height H_d of 94 ± 22 pc at the Sun's location (Drimmel and Spergel, 2001)[1] — and the latest three-dimensional dust map considers $|z| < 100$ pc (Kh et al., 2018). With this, and our other selections, we also avoid vertical structure in the spiral arms (Camargo, Bonatto, and Bica, 2015). That

This chapter was originally published in the *Astrophysical Journal*, and is reproduced with permission. The published article can be found here: Gardner, Susan, Austin Hinkel, and Brian Yanny. "Applying Noether's theorem to matter in the Milky Way: evidence for external perturbations and non-steady-state effects from Gaia Data Release 2." The *Astrophysical Journal* 890.2 (2020): 110. doi: https://doi.org/10.3847/1538-4357/ab66c8

[1] This result is 2 times smaller than what one would extract from Table 1 of Drimmel and Spergel (2001), because we define the vertical scale height from the behavior of the dust density, $\rho_{\rm dust} \sim \exp(-|z|/H_d)$, as $|z|$ grows large.

our selection is also north-south reflection symmetric is important to establishing the origin of the symmetry-breaking effects we find. We test axial and reflection symmetry by comparing the number of stars "left" and "right" of the anti-center line at a Galactocentric azimuth of $\phi = 180°$, running from the Galactic Center through the sun, so that "left (right)" refers to $\phi > (<)180°$ with $|180° - \phi|$, and we do this both for stars in the north ($z > 0$) and south ($z < 0$). The appearance of axial-symmetry breaking would reveal that the matter in the Milky Way (MW) is subject to external and/or time-varying forces. By comparing axial symmetry breaking in the north and south we can separate time-varying forces from external ones. Particularly, we find that the axial symmetry breaking of the north and south combined is much smaller than that of their difference. Since An, Evans, and Sanders (2017) have shown that an axially symmetric galaxy in steady state must be north-south symmetric, it is the breaking of axial symmetry as a north-south difference that emerges as a predominantly non-steady-state effect. Indeed, from our study we discover a correlated left-right, north-south asymmetry in stellar number counts. We interpret the smaller left-right axial symmetry breaking in the combination of star counts, north and south, as evidence of external or non-isolating forces, though that such forces may also be time-dependent is not excluded.

Considerable evidence exists for imperfections throughout the Galactic disk. The disk is warped and flared in HI gas (Levine, Blitz, and Heiles, 2006; Kalberla et al., 2007) and in stars (Alard, 2000; Ferguson, Gardner, and Yanny, 2017), with striking evidence for the latter emerging recently from three-dimensional maps of samples of 1339 and 2431 Cepheids respectively (Chen et al., 2019b; Skowron et al., 2019). Rings (Newberg et al., 2002; Morganson et al., 2016) and ripples (Price-Whelan et al., 2015; Xu et al., 2015) have been noted, and vertical, wave-like asymmetries have been observed in main-sequence stars near the Sun's location from the Sloan Digital Sky Survey (SDSS) (Widrow et al., 2012; Yanny and Gardner, 2013; Ferguson, Gardner, and Yanny, 2017) and from *Gaia* DR2 (Bennett and Bovy, 2018). Evidence for axial-symmetry breaking of out-of-plane main-sequence stars in the north with SDSS has also been observed (Ferguson, Gardner, and Yanny, 2017). Studies of the DF have been greatly enriched by the astrometry of *Gaia* DR2 (Prusti et al., 2016; Brown et al., 2018). Notably Antoja et al. (2018) have discovered striking "snail shell and ridge" correlations within the position and velocity components of the DF that speak to both axially asymmetric and non-steady-state behavior, and, as they note, is attributable to the existence of the Galactic bar, spiral arms, as well as external perturbations.

The particular origins of these various effects are not well-established. Galactic warps have been thought to have a dynamical origin, appearing and disappearing on time scales short compared to the age of the universe, due to interactions with the halo and its satellites (Nelson and Tremaine, 1995; Shen and Sellwood, 2006), though it has also been suggested that the warp in HI gas is due to the presence of the Large Magellanic Cloud (LMC) (Weinberg and Blitz, 2006). The vertical asymmetries in the stellar density may be due to an ancient impact, possibly by the Sagittarius dwarf galaxy (Widrow et al., 2012), with support for the impact hypothesis coming not only from theoretical investigations (Purcell et al., 2011; Gómez et al., 2012b),

but also from an observed vertical wave in mean metallicity (An, 2019), inferred from SDSS photometry, with features similar to the observed density wave. The novel phase-space structures noted by Antoja et al. (2018) also offer support to the impact hypothesis, as such features had been predicted as a consequence (Purcell et al., 2011; Gómez et al., 2012a; D'Onghia et al., 2016; Fux, 2001). Recently, too, the discovery of stars with retrograde motion in the disk has led to determination of a previously unidentified ancient impact, from Gaia-Enceladus (or the Gaia-Sausage) in the inner halo (Helmi et al., 2018b; Belokurov et al., 2018). Also Koppelman, Helmi, and Veljanoski (2018) have noted significant merger debris, and streams, in the halo, which are also an expected consequence of ancient impacts — and a stellar stream has been discovered in the solar neighborhood as well (Necib et al., 2019). The velocity ellipsoid (Hagen et al., 2019) and DM distribution (Posti and Helmi, 2019) are not spheroidal either, with the evidence favoring a prolate matter distribution. Studies of flaring HI gas in the outer galaxy also support a prolate DM distribution (Banerjee and Jog, 2011); these authors note that a prolate halo can support long-lived warps (Ideta et al., 2000), which would help to explain why they are commonly seen (Banerjee and Jog, 2011). It has also been suggested that some of these features could arise from a dynamically active disk (Chequers, Widrow, and Darling, 2018) in isolation. Others note that ridges in phase-space may also connect to the Galactic bar (Mühlbauer and Dehnen, 2003; Fragkoudi et al., 2019).

Recent studies of the Orphan stream appear to challenge but also perhaps clarify much of this picture. It has been shown that stars in that stream have velocities that misalign with the stream track (Koposov et al., 2019; Fardal et al., 2019), and Erkal et al. (2019) have shown that it is possible to explain these offsets by the gravitational interaction with the LMC system if its mass (including an associated LMC dark matter halo) is $1.38\ ^{+0.27}_{-0.24} \times 10^{11} M_{\odot}$, some 30 times more massive than its mass in stars (van der Marel, 2011) and 10 times more massive than an analysis of its rotation curve would suggest (Marel and Kallivayalil, 2013) — though other authors have also noted the need for a more massive LMC (Peñarrubia et al., 2015; Laporte et al., 2018a; Moster, Naab, and White, 2013; Behroozi, Wechsler, and Conroy, 2013) from very different viewpoints. Erkal et al. (2019) have also used the motion of stars within the Orphan stream to fit for the distorted shape of the matter DF in the MW from the interaction with the LMC. In contrast to the distributions discussed earlier (Banerjee and Jog, 2011; Posti and Helmi, 2019) — the shapes they determine are axially *asymmetric*, with some preference for a prolate geometry.

We note the phase space studies of Antoja et al. (2018) were made from a sample of some 6 million stars. In this paper we consider a sample of up to 14.4 million stars, carefully selected for sensitive studies of the axial and vertical symmetry breaking patterns, to enable a determination of the most likely origin of the observed effects. Remarkably we find that the distorted matter DFs found by Erkal et al. (2019) and the asymmetries that we determine in our stellar data set can confront and discriminate between their offered solutions. In particular, we find strong preference for a prolate form, in loose agreement with earlier work (Helmi, 2004; Banerjee and Jog, 2011) — yet stemming from a completely different origin.

5.2 Theory

Noether's theorem reveals that each continuous symmetry of a Hamiltonian system has an associated integral of motion (Noether, 1918). In this paper we evaluate the extent to which MW stars out of the Galactic mid-plane region are axially symmetric, with the implication that axial-symmetry breaking would speak to the violation of the conditions under which L_z holds as an integral of motion. Strictly speaking, this association requires that the converse of Noether's theorem holds; that, specifically, if L_z is an integral of motion, then the system is invariant under rotations about the z axis. This holds here, noting Theorem 5.58 of Olver (1993), with explicit demonstrations extant in the context of the stellar DF. For example, an isolated stellar system with an ergodic DF — so that f is a non-negative function of H — is spherical (Binney and Tremaine, 2008). Here non-zero L_z would imply that rotational symmetry about the $\hat{z}$ direction should be manifest. Thus if axial symmetry is broken, external, and possibly time-dependent, forces must be at work.

In contrast, testing axial symmetry above and below the Galactic plane probes time-dependent interactions. That is, Theorem 6 of An, Evans, and Sanders (2017) states that an axially symmetric galaxy in steady state must have north-south reflection symmetry, where we note Schulz et al. (2013) for a slightly less general proof of north-south symmetry in steady state. Thus a symmetry-breaking pattern in which axial symmetry is broken differently above and below the Galactic plane speaks to the existence of non-steady-state effects within and possibly on the MW. To test axial symmetry, we count the number of stars on either side of $\phi = 180°$, the anti-center line with ϕ the Galactocentric longitude, and compute the asymmetry parameter $\mathcal{A}(\phi)$:

$$\mathcal{A}(\phi) = \frac{n_L(\phi) - n_R(\phi)}{n_L(\phi) + n_R(\phi)}\,, \tag{5.1}$$

where $n_L(\phi)$ and $n_R(\phi)$ are defined as the number of stars at $|180° - \phi|$, left and right of the anti-center line, respectively. The functions $n_{L,R}(\phi)$ subsume integrals over regions in the in-plane radial coordinate R from the Galactic center (GC) and the vertical distance z from the mid-point of the Galactic plane. We note that Eq. (5.1) implies that $A(\phi)$ for the north plus south sample is not given by sum of the asymmetry in the north and that in the south. For a perfectly axially-symmetric system, $\mathcal{A}(\phi) = 0$.

External Torques from Nearby Masses

Our Galaxy possesses very massive satellite galaxies and is in the Local Group. The torques exerted by these external bodies could cause L_z to be appreciably time-dependent, spoiling axial symmetry. Non-steady-state forces could also exist *within* our sample, but in this section we consider torques stemming from forces external to it. In order to determine the most important contributions, we estimate the torques from the most massive and nearby objects beyond the MW, such as the Large and Small Magellanic Clouds (LMC & SMC) and the M31 (Andromeda) galaxy, as well as the Galactic bar, as it is not axially symmetric. We treat the Magellanic

Clouds as a single system because they are bound together if the mass is in excess of $\sim 10^{11} M_\odot$ (Kallivayalil et al., 2013), and, moreover, its mass appears to be DM dominated, though we shall usually refer to this system as the LMC henceforth in this work. We also evaluate the impacts of a few other prominent objects and show them to be relatively negligible. We assume the external sources are faraway point masses, ignoring the corrections that come from their finite extent. For the Galactic bar/bulge system we must be more careful. If the center of the MW is co-located with the center of mass (CM) of the bar/bulge, symmetry constrains the torque from the CM to be zero. If its CM is at the mid-point of its length, its net dipole moment vanishes, yet it can still exert a non-zero torque because it has a small tilt with respect to the anti-center line. To compute the torques, we use the object locations tabulated in SIMBAD (Wenger et al., 2000). The Sun is taken to be at (-8,0,0) kpc in Galactocentric xyz-coordinates. The Galactic bar/bulge system consists of a box/peanut-shaped bulge and a long bar (Bland-Hawthorn and Gerhard, 2016), and we assume that the torque it exerts is dominated by the first, more massive object. Portail et al. (2015) have found its dynamical mass to be $1.87 \pm 0.4 \times 10^{10} M_\odot$ within a box of $\pm 2.2 \times \pm 1.4 \times \pm 1.2$ kpc in volume. The bar angle ϕ_{bp} made by its semi-major axis with respect to the anti-center line has been found from a study of red-clump giants to be $27 \pm 2^\circ$ (Wegg and Gerhard, 2013), noting that the near side of that axis points in the first quadrant, $0^\circ < l < 90^\circ$ (Wegg and Gerhard, 2013; Bland-Hawthorn and Gerhard, 2016). This crudely implies that the half length of the peanut bulge is 1.4 kpc long, and for reason of estimate we suppose a quarter of the dynamical mass is associated with the end of that half-length. This gives our numerical value for the torque. We compile these results in Table 5.1, where M is the mass of the external source, or perturber; d is the distance of its CM from the Sun, which is the approximate center of our sample; and τ_z is the torque exerted by the CM on the Sun in the $\hat{z}$ direction. Our estimate for the Galactic bar is admittedly crude, but it should suffice for our rough rank ordering.

From Table 5.1, it is apparent that the largest effect comes from the LMC system. Other significant perturbers include the Galactic bar and M31, though the uncertainties are such that their relative roles could be reversed. The net torque from these sources impacts both the shape and magnitude of $\mathcal{A}(\phi)$. Nevertheless our particular accounting shows that the LMC system grossly outweighs the other perturbers. However, if the shape of $\mathcal{A}(\phi)$ does not match that expected from the LMC, say, then this could speak to matter effects, possibly from DM, that clandestinely torque our sample. Conversely, if we can account for the shape of $\mathcal{A}(\phi)$ we may well be able to constrain such structures. Thus far we have focused on external perturbations, which act to break the axial symmetry of our stellar sample, north plus south. However, non-steady-state effects *within* our sample may also exist and stem from different sources, such as from the passage of ancient satellites that perturb and excite the disk. Indeed, the interaction of the Sagittarius (Sgr) dwarf spheroidal (dSph) with the Galactic disk has been suggested as the origin (Widrow et al., 2012; Gómez et al., 2012b) of the vertical, wave-like perturbations we noted earlier (Widrow et al., 2012; Yanny and Gardner, 2013; Bennett and Bovy, 2018), and the effect can also give rise (Darling and Widrow, 2019; Laporte et al., 2019) to the Gaia phase space spiral

Table 5.1: Nearby external objects that torque the stars in our sample, with torque reported in units of $M_\odot$/pc. The errors in the inputs are such that the LMC system undoubtedly gives the largest effect.

Object	Mass ($M_\odot$)	distance (kpc)	M/d^2 ($M_\odot$/pc^2)	τ_z ($M_\odot$/pc)
LMC (& SMC)	$1.4(3) \times 10^{11}$ [a]	52(2) [b]	51	340,000
M31	$1.3(4) \times 10^{12}$ [c]	772(44) [d]	2	-14,000
Triangulum	6×10^{10} [e]	839(28) [f]	0.1	-420
Galactic Bar/bulge	$1.87(0.4) \times 10^{10}$ [g]	8 [h]	288	-47,000
Sagittarius	$2.5(1.3) \times 10^{8}$ [i]	28 [i]	0.3	-240
Fornax	$1.6(1) \times 10^{8}$ [j]	138(8) [j]	0.01	23
Carina	$2.3(2) \times 10^{7}$ [j]	101(5) [j]	< 0.01	16
Sextans	$4.0(6) \times 10^{7}$ [j]	86(4) [j]	0.01	29
Sculptor	$3.1(2) \times 10^{7}$ [j]	79(4) [j]	0.01	5
Gaia-Enceladus	$\mathcal{O}(10^9)$ [k]	-	-	-

[a] Erkal et al. (2019)
[b] Panagia (1999)
[c] Peñarrubia et al. (2015)
[d] Ribas et al. (2005)
[e] Within 17 kpc from center as per Corbelli (2003)
[f] Gieren et al. (2013)
[g] Portail et al. (2015)
[h] Assumed
[i] Law and Majewski (2010)
[j] Łokas (2009)
[k] Helmi et al. (2018b) and Belokurov et al. (2018)

(Antoja et al., 2018).

5.3 Data Selection and Analysis

We use data from the European Space Agency's *Gaia* space telescope, via the online *Gaia* archive (Prusti et al., 2016; Brown et al., 2018). The success of our analysis demands that we select stars, left and right, north and south, in a very balanced way. Our selections were made from stars with measured parallaxes (Lindegren et al., 2018), though we choose to apply an intermediate offset of 0.07 mas (noting evidence for Gaia DR2 parallax zero points ranging from -0.029 to -0.083 mas depending on reference population in Zinn et al. (2019), Stassun and Torres (2018), and Lindegren et al. (2018)), to add to all parallax measurements. With the shift applied, we keep only stars with measured parallaxes, $\varpi > 0$ mas, though this shift is a trivial one for our data set, because no stars are added as a result. We also require $|b| > 30^\circ$ to avoid the extinction effects characteristic of lower latitudes. To avoid selection bias, we remove all stars in the directions of the LMC and SMC, as well as their reflections across the mid-plane, across the anti-center line, and across both the mid-plane and anti-center line. The LMC and SMC are removed by requiring $b > -39$, $l \in [271, 287]$ and $b \in [-41, -48]$, $l \in [299, 307]$ respectively. The other 6 box cuts are constructed with suitable reflections. Considering the completeness of our data set in magnitude, color, $|z|$, and R we see no clear evidence of incompleteness or of obvious, systematic biases if we choose $G_{\rm BP} - G_{\rm RP} \in [0.5, 2.5]$ mag, $G \in [14, 18]$ mag, $|z| \in [0.2, 3]$ kpc, $|b| > 30^\circ$, $\varpi > 0$ mas, and $R \in [7, 9]$ kpc. If we choose $|180^\circ - \phi| < 12^\circ$, these cuts yield a sample of 14.4 million stars. The key cuts which ensure completeness are restricting the Gaia data sample to brighter limits ($G < 18$) and avoiding crowded low latitude regions. Tests involving restrictions to an even brighter limit $G < 17$, while lowering significance with a smaller sample, does not change our asymmetry findings (see Figure 1) and gives us confidence that we are not probing incomplete Gaia DR2 samples as a function of azimuth. We defer more discussion of the completeness studies that motivate these choices to a future paper (Hinkel et al. in prep.), though we find it pertinent to highlight a key result of that work: as a result of our selections in G-band magnitude and color, we find the average relative parallax error of our stars to be reduced to some 10%, even though we have not directly restricted that parameter, because the distance distributions would become skewed as a result (Luri et al., 2018; Bailer-Jones et al., 2018). Moreover, noting Fig. 7 of Arenou et al. (2018), we have also explicitly studied the impact of more crowded fields on our results. We find, e.g., that making additional restrictions on our data set in the direction of the Galactic Center has negligible impact on the results we report here.

Table 5.2 shows that our data selections are well matched, north and south, as well as left and right, showing no sign that spatial asymmetries in the dust observed in the mid-plane region (Schlegel, Finkbeiner, and Davis, 1998) impact our results. The left and right samples, north and south, are matched to within about 0.06%. The larger, but still very small, number count asymmetries we observe in the north *or* south turn out to match more poorly, but its source may stem from the physics that makes $A_{N,S}(\phi)$ so much larger. As the ϕ dependence of $A(\phi)$ is our key result,

we have also studied completeness within the $x-y$ plane carefully to determine that we should limit $|180-\phi| \leq 6^\circ$ for our R selection, implying, roughly, that we choose a reach in x and in y which is about ± 1 kpc of the Sun's location, yielding a sample of 11.7 million stars.

Table 5.2: The number of stars found in each quadrant of the analysis, with $|180^\circ - \phi| < 12^\circ$. Totals for the left and right are also shown. The sample is very evenly distributed, left and right, with an aggregate asymmetry of $\mathcal{A} \approx 6 \times 10^{-4}$.

	Left	Right	Asymmetry (%)
North	3,376,969	3,471,980	-1.39
South	3,815,477	3,729,647	1.14
TOTAL:	7,192,446	7,201,627	-0.06

Data Analysis

The results of our asymmetry analysis of star counts left-right of the anti-center line are shown in Fig. 5.1, with panel a) revealing that axial symmetry in the north plus south (N+S) sample (blue diamonds) is significantly broken at a level up to 0.5% out to angles $|180-\phi| < 6^\circ$, though the symmetry breaking effects in the north (N) only (black up triangles) or south (S) only (red down triangles) samples can be much larger. Remarkably the N and S left-right asymmetries are also anti-correlated in sign, so that the difference in the N and S asymmetries can be grossly larger than that of the N+S sample as shown in Fig. 5.1b. This comparison shows that the symmetry-breaking effects from non-steady-state interactions within and beyond the Galaxy are grossly larger than those resulting from a steady, external perturbation. In panels c) and d) we reinforce the results of panel a) by noting that the asymmetry trend persists when only keeping stars with $16 < G < 18$ (panel c) and when making a very conservative faint end cut, keeping stars with $14 < G < 17$ (panel d). Luri et al. (2018) note that the *Gaia* DR2 catalogue is "essentially complete between $G \approx 12$ and ~ 17 mag," though it also extends significantly beyond $G = 20$ mag. Parallax measurements are, however, quite incomplete for $G > 18$ in Gaia DR2, and Luri et al. (2018) also remark that the faint end limit is "fuzzy" in that it can depend on object density and on the filtering on data quality prior to publication. Nevertheless we do not observe any significant changes in our results with changes in the G-band selection so long as we choose $G < 18$ magnitude cuts. Thus we opt for the largest selection we can make. If we restrict to a brighter limit than $G < 17$, then substantially decreased number counts do more strongly begin to compromise the significance of especially N (only) and S (only) studies of the asymmetry.

Although the asymmetries we have found are small, they are nevertheless significant. For the N+S result shown in Fig. 5.1a, a linear fit to the data shows that both the constant and linear term are non-zero beyond 5σ significance: $A(\phi) = (-2.0963 \pm 0.0003 + |180-\phi|(-0.45050 \pm 0.00003)) \times 10^{-3}$. The N+S asymmetry is

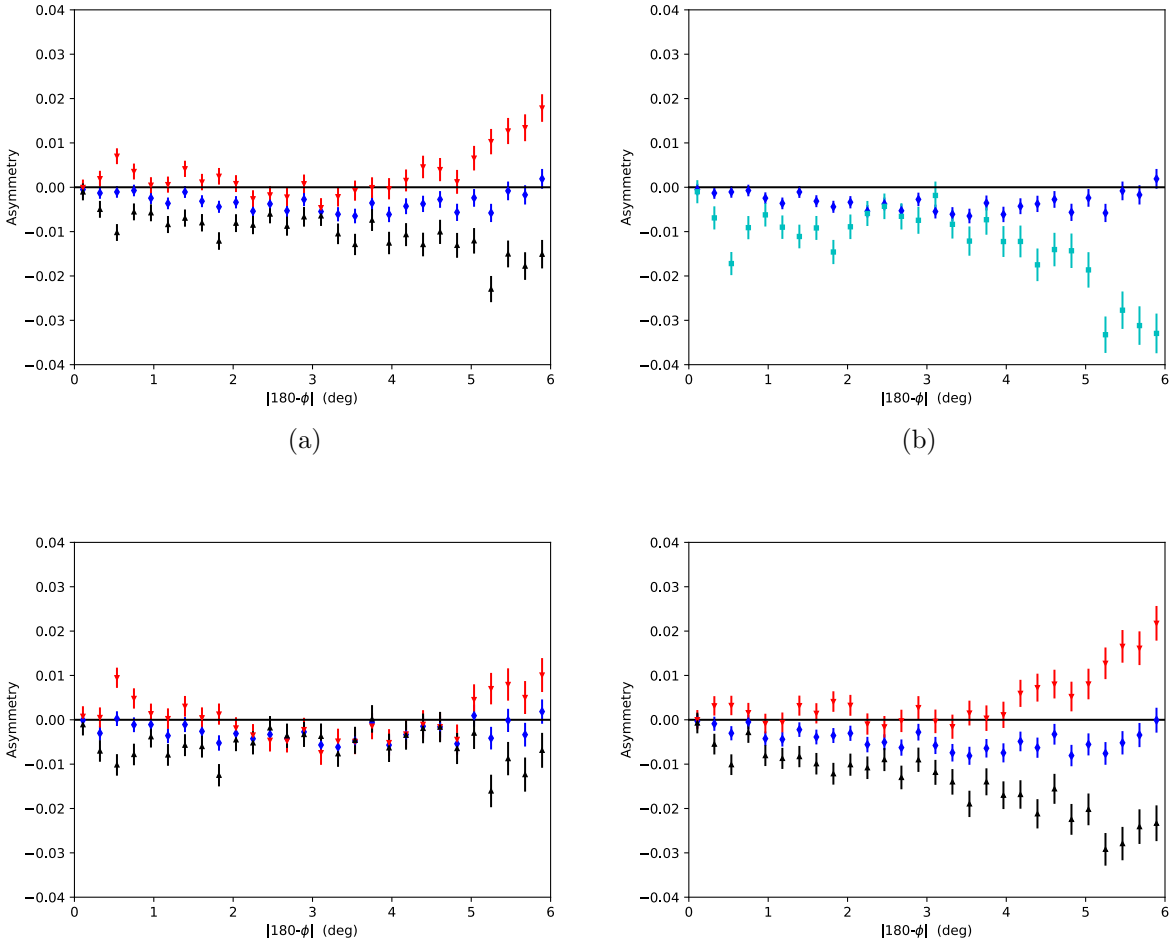

Figure 5.1: The asymmetry $A(\phi)$ with ϕ for (a) our selected data set, with red, downward pointing triangles (S); black, upward pointing triangles (N); and blue diamonds (N+S). (b) We compare $A(\phi)$ in the N+S sample with the difference of $A(\phi)$ in the north and $A(\phi)$ in the south (N-S) (squares). We compare these results with different G-band magnitude selections, in (c) $16 < G < 18$ mag, noting that by doubling the size of our magnitude window, we do not appreciably change our result, and (d) $14 < G < 17$ mag, minding (Luri et al., 2018), where we note the text for further discussion. Here, too, there is no significant, qualitative change when we include stars with $G < 18$.

larger than the aggregate raw number count asymmetry of our data selection, shown in Table 5.2. Were we to repeat the raw number count comparison for a maximum value of $|180 - \phi| = 6°$ we would find a value of -0.0032, so that our fit result is also significantly different from that. It is thus apparent that none of the asymmetries — N, S, or N+S — are constant with ϕ. Morever, an anti-correlation of the asymmetries N and S is also present, noting that at values of $|180° - \phi| \sim 0.5°, 1.8°$, and $> 5°$

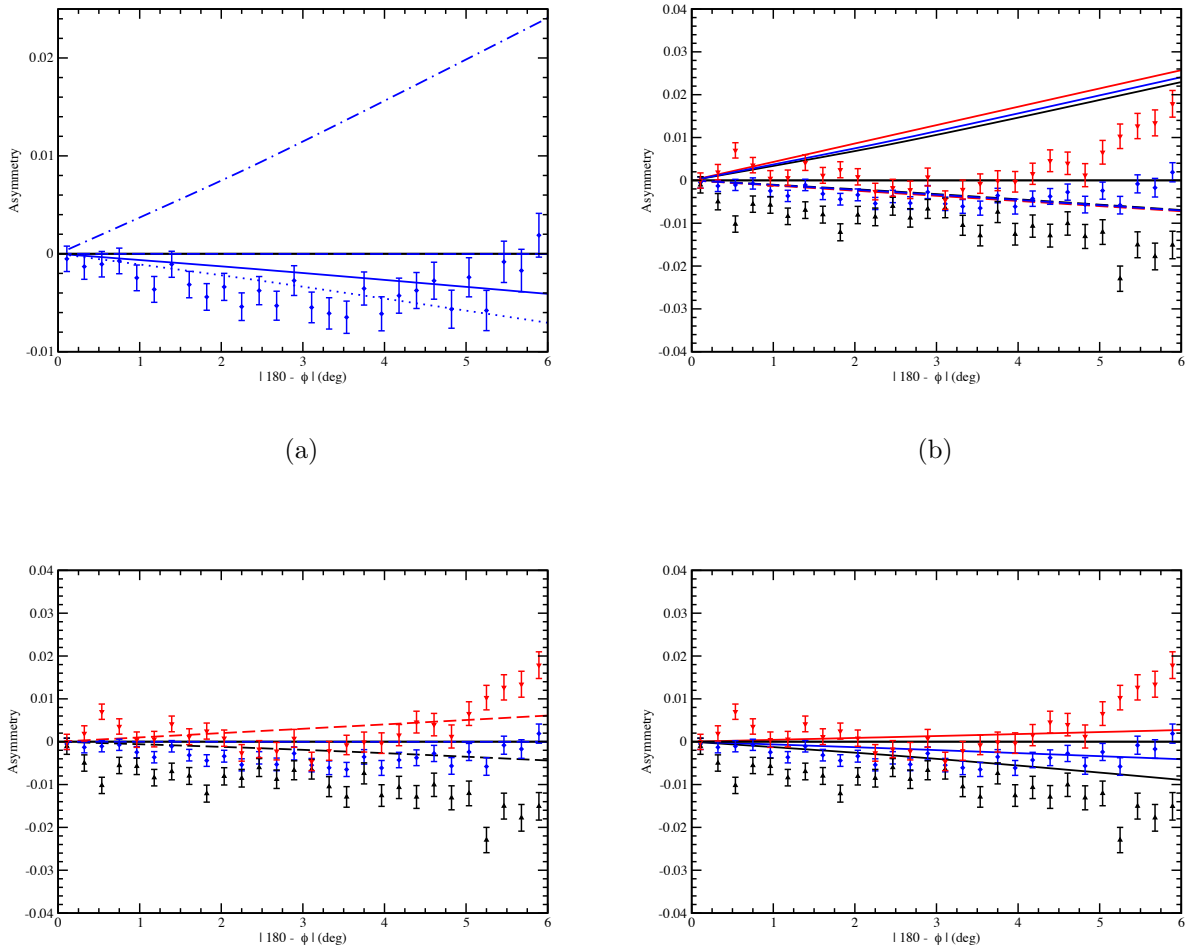

Figure 5.2: Asymmetries, as in Eq. (1), computed for the geometry of our sample using the distorted MW halo models of Erkal et al. (2019) from fits of the LMC on the Orphan stream, with and without the reflex motion of the MW, are compared with the results of Fig. 5.1a). In (a) we show the N+S asymmetry of Fig. 5.1 with the oblate (dot), reflex oblate (dot-dash), and reflex prolate (solid). The prolate result has also been included, but its asymmetry is so small that it is indistinguishable from the horizontal axis. In (b) we compare the asymmetries from Fig. 5.1a with those for the oblate (dash) and reflex oblate (solid), for S (red), N (black), and N+S (blue) — and use these latter assignments throughout. We compare with the prolate (dash) results in (c) and the reflex prolate (solid) results in (d).

(Fig. 5.1b), an increase in the asymmetry in the N is matched by a more negative asymmetry in the S. We comment on these smaller scale asymmetries briefly below.

Asymmetries from Mass Distribution Models Deduced from Orphan Stream Fits

Erkal et al. (2019) have computed the relative likelihoods of several different MW mass distribution models that were used to fit out-of-stream velocities in the entire Orphan stream in the presence of the LMC. They adopt a generalized form of "MW-Potential2014" from Bovy (2015), which consists of bulge, disk, and halo components, though they keep the bulge and disk components fixed and allow only the mass and shape of the halo to vary. Erkal et al. (2019) find that the LMC induces a flattening of the halo in a direction away from the z axis, though they caution against interpreting this as an intrinsic property of the disk; we revisit this in the face of our asymmetry results below. The distortion of the halo, which they assume is of NFW form (Navarro, Frenk, and White, 1997), yields either an oblate or prolate shape, and they allow for the reflex motion of the MW in the presence of the LMC, though they have not allowed the shape of the LMC itself to vary. (For reference, we note that the scale height in their disk model (Miyamoto and Nagai, 1975) is 280 pc.) We have taken the various best fit parameters from Table A1 of Erkal et al. (2019) and have computed an additional observable: the asymmetry in left-right star counts versus Galactocentric azimuth (in N, S, and N+S versions) that would result from each of the distorted halo models that they tabulate in their Table A1 — oblate, prolate, and with and without the reflex action of the MW halo. We have not used their spherical halo solution, which their fits strongly disfavor, because that would yield a vanishing left-right asymmetry. That we expect these asymmetries to be pertinent to our asymmetry results stem from the torques estimated in Table 5.1 — it is apparent that the LMC must dominate any N+S asymmetry today. Moreover, although (Erkal et al., 2019) fit for a distorted halo only, the outcome of their work is a distorted *matter* distribution, which we probe near the Sun through the distribution of stellar number counts. The results of these analytical computations are shown in straight lines in Figure 2, overlaid with the star count results from Figure 1.

The data in panel a) of Fig. 5.2 clearly show a significant large scale trend in the left-right asymmetry of combined N+S star counts (blue diamonds) extending from the $\phi = 180°$ anti-center line to $\sim 6°$ left or right. Evaluating the χ^2 statistic for these computed models compared with the data, noting that the Erkal et al. (2019) fits contain 5 parameters: the halo mass and scale radius, and the magnitude and orientation (in (l, b)) of the flattening, we find for our 28 data points that $\chi^2/(n = 23)$ is 3.64 (reflex prolate, solid blue with a downward tilt), 6.40 (oblate, dotted with downward tilt), 7.11 (prolate, solid, hugging $A \sim 0$), and 201 (reflex oblate, dot-dash, upward tilt). Although no one model describes the N+S asymmetry data well, the preference for the reflex prolate or possibly the oblate (though see below) description is clear. That is, of the models considered by Erkal et al. (2019), an LMC torque which distorts the halo of the MW, while accounting for its reflex motion, into a prolate ellipsoid with its major axis aligned roughly along the line between the Galactic center and the LMC provides the best match to our solar-neighborhood star-count asymmetries. An oblate model which is not corrected for reflex motion can also fit the combined $N+S$ data, but once we consider the N and S samples separately the oblate

halo models are clearly ruled out. All the models are more strongly distinguished once the N and S results are also considered, and we show these comparisons in panels b), c), and d) of Fig. 5.2. There we compare our asymmetry count results with those of the model fits in the N, S, and N+S, where we consider oblate (dashed) and reflex oblate (solid) in b), prolate in c) and reflex prolate in d). The problem with matching the data to an oblate model becomes apparent when looking at the N, S, and N+S asymmetries in Fig. 5.2 b): The three curves are nearly coincident, but order of the lines is reversed, with S slightly below N in the model calculations, whereas the N-only asymmetry is much more negative than the S-only in the data counts, in clear contradiction with the data. Additionally, the split in N-only and S-only tracks is not reflected in the nearly coincident model lines. Comparing with the reflex oblate model, we see that the N, S, and N+S asymmetries split slightly, but they all very much diverge from the data. In panels c) and d), we see that the prolate and reflex prolate models have asymmetries that strongly differentiate N and S, as do the data points from Fig. 5.1. The prolate model has a near null N+S asymmetry; this results because its major axis points very nearly in the $l = 90°$ direction, so that in summing N and S there is no left-right asymmetry. We thus see that the reflex prolate model describes the data better. These conclusions are very much born out by a χ^2 analysis; for N, S, and N+S, respectively, $\chi^2/(n = 23)$ is 15.8, 21.2, and 6.40 (oblate); 143, 88.7, 201 (reflex oblate); 18.7, 12.2, 7.11 (prolate), and 15.0, 9.82, 3.64 (reflex prolate), We thus conclude that a oblate shape in which the flattened direction is in the orbital plane of the LMC, needed to fit the Orphan stream data (Erkal et al., 2019) is ruled out. Thus, by showing that a prolate, reflex halo model is best fit (amongst the small set of models here) and by ruling out oblate models, we demonstrate the power of asymmetries to make new and significant constraints on the distribution of dark matter in and around our MW.

While tying this overall $\pm 6°$ trend in ϕ to the influence of a massive LMC and demonstrating its influence on the dark matter halo of our MW, distorting it into a prolate spheroid, is our main result, we also note several smaller scale "blips" in the asymmetries of Fig. 5.2b) which may be attributed to some of the other substructures listed in Table 5.1. We discuss this further in § 5.4.

5.4 Results

Evidence for External Perturbations

The LMC appears to be the dominant external influence on the Galaxy. Erkal et al. (2019) find a galactic potential that incorporates the LMC (& SMC)'s effect on the MW, and we note that it explicitly breaks axial symmetry. Upon integrating their models over the same volume of space as that used in Fig. 5.2 a), we find that the "reflex prolate" model of Erkal et al. (2019) is the most consistent with the observed axial asymmetries.

While detailed model explanations are beyond the scope of this work, we note three further possible connections between the LMC and non-axisymmetric structure in the disk and halo, which have already been suggested in the literature:

1. As first pointed out in Law and Majewski (2010), the pole of the Magellanic stream is aligned within 1° of the tilted triaxial MW halo needed to reproduce the orbit of the Sagittarius stellar stream. Increasing the mass by a factor of a few as suggested by Erkal et al. (2019) makes the apparent unusual alignment and shape of the MW halo compared with its disk quite plausible.

2. An analysis by Iorio and Belokurov (2018) of the distribution of RR Lyrae associated with the Gaia-Enceladus structure (Helmi et al., 2018b; Belokurov et al., 2018) have been shown to point to a MW halo elongated in the direction to the LMC.

3. The line of anti-nodes for bending modes in the HI gas disk (Levine, Blitz, and Heiles, 2006) is at $\phi \sim 270°$ and for the Cepheid-traced outer stellar disk (Skowron et al., 2019; Chen et al., 2019b) is in the range $\phi \in [245°, 255°]$, not far from $\phi_{\rm LMC} \sim 269°$. The orientation of the long axis of the prolate halo geometry we favor coincides with this direction as well and could support this $m = 1$ bending mode as suggested by Dekel and Shlosman (1983), Sparke and Casertano (1988), and Ideta et al. (2000), helping to explain its long-lived nature (Ideta et al., 2000). Linking the LMC to the warp also supports the results of Weinberg and Blitz (2006).

Evidence for Non-steady-state Effects

We argue that the largest MW perturber is a heavy LMC system having some 10% of the MW's mass (Erkal et al., 2019). That system, assumed to be on first passage by the MW, has a typical median in-fall time of ∼1.4 Gyr for MW and LMC masses similar to what we assume here (Patel, Besla, and Sohn, 2016). This timescale is long enough to be considered quasi-steady-state and results in unobservably slow adiabatic changes (Binney and Tremaine, 2008). Nevertheless, we regard the observed distortions not as long-term properties of the disk, keeping in mind that it is difficult to realize a stellar disk that is misaligned with the halo (Debattista et al., 2013; Erkal et al., 2019), but rather as a response to the LMC infall. Yet, there are regions where the left-right asymmetry is much larger, particularly if we consider the asymmetry N-S rather than N+S, as in Fig. 5.1b) near $|180° - \phi| \sim 0.5°, 1.8°, > 5°$. According to Theorem 6 from An, Evans, and Sanders (2017), the approximate azimuthal symmetry here means than the north-south difference we see is indicative of a departure from steady-state dynamics on smaller time — and length — scales.

Given that the effect that causes these "blips" should be appreciably time dependent, the Galactic bar is a great candidate, with a pattern speed known to be roughly 39 ± 3.5 $^{\rm km}/_{\rm s \cdot kpc}$ (Portail et al., 2016). This pattern speed corresponds to a period of roughly 160 Myr, much shorter than the dynamical timescale of the LMC infall and is comparable with the crossing time near the solar neighborhood (∼ 300 Myr). This hypothesis is bolstered by the fact that the Outer Lindblad Resonance is thought to be near the solar circle (Dehnen, 2000), where we also note Fragkoudi et al. (2019).

Generally the emergence of features that differentiate N from S supports our interpretation of the halo distortion, which we also observe through axial asymmetries in our stellar sample, as a response to the LMC infall.

5.5 Summary

We have discovered statistically significant left-right and north-south asymmetries in Gaia DR2 star counts in the Solar neighborhood, which are all consistent with a large scale perturbation caused primarily by the LMC system — and its associated DM. Previous discussions of the relative influence of the LMC on MW disk asymmetries (Hunter and Toomre, 1969) would underestimate the LMC's relative influence due to early, lower-mass estimates of the LMC and tidal force approximations which may not work well when the larger LMC/MW mass ratio of some 10% is used. Now, recent work by Erkal et al. (2019), with its significantly larger and more accurate LMC mass, gives significant credence to the suggestion by Weinberg and Blitz (2006) that the LMC could in fact be nearly entirely responsible for the long observed HI gas warp of the MW disk. Moreover, when then modeling the LMC's influence, a non-reflex model which assumes $M_{LMC} << M_{MW}$, is insufficient, and one that can include reflex reactions of the MW due to the LMC, such as that in Erkal et al. (2019), is more appropriate. We find now, that not only can the LMC's influence explain the HI gas warp, but it also appears to induce a substantial asymmetry in the star counts left vs. right and north vs. south in the solar neighborhood of the correct sign and magnitude. Looking at other possible perturbers, the effect of the LMC is dominant compared to that of the Galactic bar (in most scenarios), the Sagittarius dwarf and stream, and finally also the more massive but much more distant perturbers, such as M31 (see Table 1). The odd, tipped triaxial shape of the MW's dark halo suggested by Law and Majewski (2010) based on the orbit of the Sagittarius stream and the elongation of the Gaia-Enceladus structure (Helmi et al., 2018b; Belokurov et al., 2018) can also both be potentially more simply understood by the graviational interaction with the LMC — though detailed modeling remains to confirm that these additional suggestions do operate in detail.

Deviations from symmetry in the case of star counts near the sun (at only the sub-percent level!), combined with results related to Noether's theorem associating a conserved angular momentum with rotational symmetry are shown here to be powerful probes of the influence of satellite torques on the overall distribution of mass in and around the MW.

Chapter 6 Probing Axial Symmetry Breaking in the Galaxy with Gaia Data Release 2

6.1 Introduction

Models of the Galaxy are often motivated by the assumption that it is isolated and thus has certain integrals of motion. It is, moreover, commonly regarded as a superposition of its disk, halo, bulge, and bar components (Robin et al., 2003; Robin et al., 2012). Each component i can be modelled by a distribution function f_i (Binney and Tremaine, 2008; Binney, 2012; Bovy and Rix, 2013; Piffl et al., 2014; Piffl, Penoyre, and Binney, 2015), which, in steady-state, is characterized by its integrals of motion, as predicated by Jeans' theorem (Jeans, 1915). It is useful to model $f_i(\mathbf{J})$, where $\mathbf{J}$ has as components the action integrals J_r, J_ϕ, and J_z, in radial, azimuthal, and vertical coordinates r, ϕ, and z with respect to the plane of the Galactic disk. Notably J_ϕ (or "L_z") is the angular momentum about the symmetry axis of an axisymmetric disk. Each $f_i(\mathbf{J})$ is a supposed invariant under the slow evolution of the Galaxy. Although the Galaxy has features that are notably axially asymmetric, namely, the spiral arms and Galactic bar, it is nevertheless the case that $f(\mathbf{J})$ modelling (Binney et al., 2014) gives a very good description of the velocity distributions observed by the RAVE survey. With the advent of *Gaia* DR2 data (Prusti et al., 2016; Lindegren et al., 2018) it has become possible to determine the structure of the dark halo from the stars alone (Binney and Piffl, 2015), in that the circular speed curve with the in-plane Galactic radius R from the reconstructed Galactic potential is compatible with the circular speed from Cepheids (Mróz et al., 2019; Binney, 2019).

An integral of motion used to model the Galactic distribution function should also correspond to a continuous symmetry, as the converse of Noether's Theorem (Noether, 1918) holds if the integral of motion is non-zero (Olver, 1993). Thus, in regions nominally described by just a disk and spheroidal halo, we expect the angular momentum about the z-axis, L_z, to be an integral of motion and thus axial symmetry should be manifest. However, we know structures such as the Galactic bar and spiral arms do not exhibit axial symmetry, and there are also satellite galaxies which may influence the Milky Way. It is thus interesting to assess the degree to which the galaxy is truly axisymmetric away from these known asymmetric sources, as doing so can provide insights into the validity of the above assumptions and help to determine which perturbers may be most relevant.

In practice, to test axial symmetry, one simply needs to count the stars in a given range of galactocentric longitude, ϕ, and then compare the counts of that bin with the

This chapter was originally published in the *Astrophysical Journal*, and is reproduced with permission. The published article can be found here: Hinkel, Austin, Susan Gardner, and Brian Yanny. "Probing Axial Symmetry Breaking in the Galaxy with Gaia Data Release 2." The *Astrophysical Journal* 893.2 (2020): 105. doi: https://doi.org/10.3847/1538-4357/ab8235

bin corresponding to a galactocentric longitude range that has been reflected across the $\phi = 180°$ line. With the star counts of the left (n_L, $\phi > 180°$) and right (n_R, $\phi < 180°$) bins, one is able to compute the asymmetry, as defined in Gardner, Hinkel, and Yanny (2020):

$$\mathcal{A}(\phi) = \frac{n_L(\phi) - n_R(\phi)}{n_L(\phi) + n_R(\phi)}, \tag{6.1}$$

where the functions $n_{L,R}(\phi)$ contain integrals over the other coordinates as appropriate. Computing axial asymmetries for the Galaxy would, in theory, be possible with respect to any Galactocentric longitude, but due to observational constraints driven by the heliocentric nature of our $|b| > 30°$ latitude cuts and the limited reach of the *Gaia* telescope, we use the $\phi = 180°$ line as our baseline and limit our probe to galactocentric longitudes within 6° of this baseline and within galactocentric in-plane distances of $7 < R < 9$ kpc, where the Sun is assumed to be at $R = R_0 = 8$ kpc, though we note the recent result of 8.178 ± 0.026 kpc from Abuter et al. (2019), and vertical distances of no more than 3 kpc above or below the plane. A schematic depiction of the (in-plane projected) geometry involved in this process can be found in Fig. 6.1. If tests of axial symmetry about other "fold" lines were ever to become practicable, our ability to probe dynamical effects, such as from the presence of the Galactic bar, would be greatly heightened.

To our knowledge, a test of axial asymmetry in stars out of the Galactic mid-plane region is first employed in Gardner, Hinkel, and Yanny (2020). In this companion paper we carefully develop the data selection procedures that make the studies of Gardner, Hinkel, and Yanny (2020) possible. There we conclude that significant asymmetries in the left versus right star counts combined with North and South sub-counts clearly imply the influence of massive objects which break the axial symmetry of the Milky Way's stellar and overall matter distributions. Comparing the relative torques due to well-known "perturber" candidates, we found the influence of the LMC to be dominant. However, due to uncertainties in the mass distributions, including those from unseen dark matter, we cannot rule out that some fraction of the mismatch in counts left and right and north and south could be due to other structures, such as the Sagittarius (Sgr) dwarf tidal stream and the Galactic bar. Gardner, Hinkel, and Yanny (2020) was further able to distinguish between oblate and prolate mass distributions by looking at not only "global" several degree scale (in ϕ) axial asymmetries, but also how these asymmetries differed north and south of the mid-plane. In Gardner, Hinkel, and Yanny (2020) we considered the analysis volume we develop in this paper, namely, the selection $7 < R < 9$ kpc, $0.2 < |z| < 3$ kpc, $|b| > 30°$ as a whole, along with brightness and color selections and particular sight-line exclusions. Here, we sub-divide the data further in an attempt to find out if the LMC is responsible for the entirety of the asymmetries, and we discover important asymmetric effects from the Galactic bar. In what follows we carefully delineate our data selection and analysis procedures before turning to a discussion of the axial asymmetries, in aggregate and in various subspaces of our analysis data set.

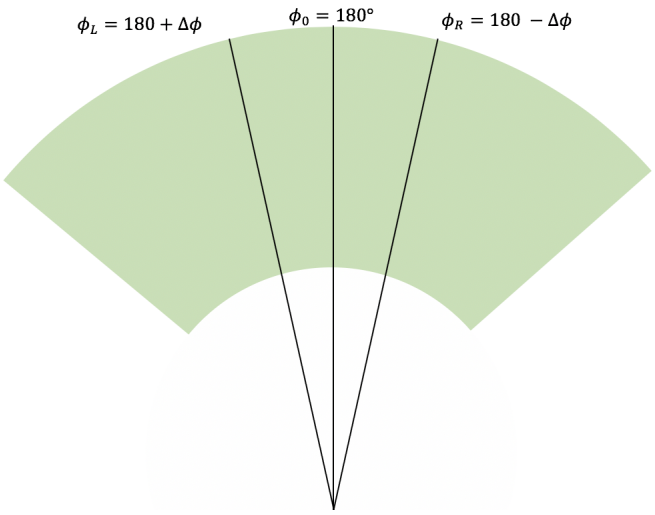

Figure 6.1: A schematic depiction (i.e., not to scale) of the method of computing an axial asymmetry. To construct $\mathcal{A}(\phi)$, one counts the number of stars, $n_{\rm R}$, in a range $\delta\phi$ about an angle $\phi_{\rm R}$ to the right of the $\phi = 180°$ line, that is, in a bin centered on $\phi_{\rm R}$, and then counts the number of stars, $n_{\rm L}$, in a bin of width $\delta\phi$ centered on the angle $\phi_{\rm L}$ to the left of the $\phi = 180°$ line, chosen such that $\phi_{\rm L} = 180° + \Delta\phi$, where $\phi_{\rm R} = 180° - \Delta\phi$ and $\Delta\phi > 0$. The asymmetry can be computed from $n_{\rm L,R}$ via Eq. 6.1. Note we choose uniform bins in $\delta\phi$ across the region of interest, so that we can assess $A(\phi)$ with ϕ.

6.2 Data Selection and Completeness Studies

The *Gaia* documentation and supporting publications (Luri et al., 2018; Bailer-Jones, 2015) suggest using a Bayesian approach to estimate distances, particularly if the relative errors in parallax are large. We do not use such an approach here, as we do not need to know a precise distance to a star, just the correct azimuthal bin into which it falls. Thus we estimate the distance to each object as the inverse of its parallax, ϖ, throughout. Additionally, we do not see any evidence that the measured parallaxes are systematically correlated with a star's location left or right of the $\phi = 180°$ line.

As noted by Luri et al. (2018), using small relative parallax error quality cuts introduces artifical asymmetries, or biases, into a data set, because the parallax error is a function of position on the sky due to the *Gaia* scanning law's non-uniform sampling of different regions of the sky. This would irreparably bias the study of symmetries over an appreciable extent of the galaxy, as shown in Fig. 6.2 a). Instead, we outline here a method for selecting a set of stars which appears to be free of any obvious biases (Fig. 6.2b) and is smoothly distributed in multiple parameter spaces, indicating that no chunks of data are missing or significantly afflicted by observational biases. To wit, we use the photometric and astrometric data to effect cuts which preserve a smooth distribution of stars in G-band magnitude, $G_{\rm BP} - G_{\rm RP}$ color, in-plane radius from the GC, and height above the plane over a range of

Galactocentric longitudes centered on the anti-center line, $\phi = 180°$. The logic of the alternative method we propose is as follows: if there is an artificial bias in the *Gaia* data set, it would manifest itself as some aberration from the expected smoothly varying distributions in at least one parameter space. In the subsections that follow, we outline each parameter space checked and use the plots generated in this study to motivate a maximal angular reach to which we can safely test axial symmetry with strong statistics.

Data Acquisition

The relevant data for this analysis was obtained from the European Space Agency's *Gaia* space telescope (Prusti et al., 2016), via the online archive[1]. Selections were made in windows of (l, b) with $\varpi_{\rm unshifted} > -0.07$ mas and $|b| > 30°$. The latter cut is made in order to stay above the dust and gas close to the mid-plane while the former was made so that after a global shift of 0.07 mas is applied to the parallax, we have only stars with physical parallaxes, so that in the shifted parallax, $\varpi > 0$ mas. We assume this shift in all that follows. The particular value for the parallax zero-point shift was chosen from a wide array offered in the literature (Lindegren et al., 2018; Stassun and Torres, 2018; Zinn et al., 2019) such that our value is a "middle-ground" choice. The particular choice of shift has no bearing on the final results as our data is quite close (the mean distance to a star in our sample is 0.94 kpc, with ∼60% of the stars within 1 kpc), and thus does not bring previously negative parallaxes into the analysis. Additionally, our analysis requires that a distance estimate via a parallax is available, so that we use only data for which the full five-parameter astrometric solution is available, as the two-parameter solution does not specify a distance (Luri et al., 2018). After the analysis of the following two subsections, we conclude that elimination of the stars with the 2-parameter "fallback" solution does not bias our result.

Masking toward select anomalous lines of sight

In order to ensure our sample is not biased in the North vs. South or for $\phi > 180°$ or $\phi < 180°$, we are forced (see below) to cut out the Large and Small Magellanic Clouds, as well as their reflections across the mid-plane, the reflections across the anti-center line, and reflections across both the mid-plane and anti-center line, as in Fig. 6.2 b). We note here that we choose not to apply relative parallax error quality cuts as suggested by Luri et al. (2018), as it is clear from Fig. 6.2 a) that such cuts actually fail to remove the LMC and SMC from the data. Additionally, visible streaks appear in the completeness data if we apply these parallax error cuts, preventing an unbiased assessment of axial symmetry.

The excision of the LMC & SMC was checked in a series of (l, b) plots with the G, $G_{\rm BP} - G_{\rm RP}$, $|b|$, and $|z|$ restrictions outlined below already in place. Thus, these selections act as an effective distance cut, which helps with the elimination of the LMC/SMC contamination caused by poor parallax assessments in the dense

[1] https://gea.esac.esa.int/archive/

field. The LMC & SMC sight lines, along with the appropriate reflections we have mentioned, are removed by excising all the data that fit the following criteria:

$$|b| \in [30°, 39°] \wedge \Big(l \in [271°, 287°] \vee l \in [73°, 89°] \Big) \tag{6.2}$$

$$|b| \in [41°, 48°] \wedge \Big(l \in [299°, 307°] \vee l \in [53°, 61°] \Big) \tag{6.3}$$

for the LMC & SMC, respectively.

Although some dust seems to survive our $|b|$ and $|z|$ cuts in the region beyond the Sun's radius, we have checked that our asymmetry results do not change appreciably if that region is excised from our data set.

In order to assess the completeness of our sample after the implementation of the above "box" cuts, the distribution of stars with respect to the angle $|180° - \phi|$ was examined for multiple different parameters. Beginning with the color and G-band magnitudes of our sample, as depicted in Fig. 6.3 a) and b) respectively, we see that there are various ranges of both parameters where we simply lack enough stars to probe very far from the $\phi = 180°$ line. In the interest of obtaining both a large number of stars and a non-negligible reach in $|180° - \phi|$, we choose to keep stars for which $G_{\rm BP} - G_{\rm RP} \in [0.5, 2.5]$ mag and $G \geq 14$ mag. We also note that the distribution shows no signs of any obvious incompleteness.

Limits on G magnitude, $G_{\rm BP} - G_{\rm RP}$ color, R, and $|z|$

Although Fig. 6.3b) suggests that one may probe larger values of $|180° - \phi|$ for fainter stars, one runs into unreliable parallax measurements for $G > 18$ mag, as the majority of stars in the trend from Fig. 6.4 with $G > 18$ mag have ${}^{\sigma_\varpi}/_{\varpi} > 0.2$. As such, we consider only the window $G \in [14, 18]$ mag. While similar to the suggestion of Luri et al. (2018) that relative parallax error cuts be used, we instead rely on the magnitude as a rough proxy for the relative parallax error. Because we are looking away from the gas and dust of the plane due to our requirement that $|b| > 30°$, we expect that the magnitudes observed by *Gaia* will not dramatically fluctuate over small scales like a hard cut on ${}^{\sigma_\varpi}/_{\varpi}$ did in Fig. 6.2 a). We are mindful that Luri et al. (2018) suggest cutting out all stars with $G > 17$ mag due to incompleteness in crowded fields, the scan-law pattern, and filtering during the data reduction process. We show later in Fig. 6.12 that the quantitative result found for the smaller, recommended magnitude window is not very different than the $G \in [14, 18]$ mag window result. Since we have cut out the regions with crowding issues (i.e., low latitudes and the LMC and SMC), using $G < 18$ mag appears to be a valid option for our particular set of cuts. By using this faintness limit, we are adding statistical strength to our analysis.

One possible alternative is using the Astrometric Excess Noise (AEN), available in the *Gaia* data (Lindegren et al., 2012), rather than the relative error in parallax, as it is not explicitly a function of the number of observations (Lindegren et al., 2018), which are known to be different in different parts of the sky (Lindegren et al., 2018). However, as Fig. 6.5 illustrates, there is a significant bias incurred from restricting the

values of the AEN. As such, we forgo any restrictions on the AEN, and instead check that our final data set results in a relatively small average AEN. For our particular latitudes, the mean AEN, $\langle \text{AEN} \rangle$, is about 1.034 mas for the entire *Gaia* database, whereas a similar yet slightly larger volume of space to our analysis (i.e., $\varpi > 0.3$ mas and $|b| > 30°$) with stars having similar magnitudes and colors yields an upper bound value of $\langle \text{AEN} \rangle \approx 0.141$ mas, nearly an order of magnitude better.

Additionally, the distribution of our data set is checked over a range of in-plane radius, R, in Fig. 6.6 a). From this examination, we cut on $R \in [7, 9]$ kpc in order to circumvent sampling a region of low statistical strength. To avoid the stars too close to the plane with known axially asymmetric features (e.g. spiral arms), we make a cut of $|z| > 0.2$ kpc. Also, to avoid straying too far from the disk into incomplete regions of $|z|$, we require $|z| < 3$ kpc as motivated by Fig. 6.6 b), where we admittedly push the data to its limits in order to sample more halo stars.

With all of the above constraints applied, we are left with a data set which is free of artificial biases left and right of the $\phi = 180°$ line. Not only is the data set well-matched, the stars themselves are, on average, very well measured with a mean relative uncertainty in parallax of about 8.6% (see Table 6.1 for relative uncertainty in parallax for each quadrant). In order to visualize this resulting data set, we show the in-plane projection of our data in Fig. 6.7 a). The geometry of the data in the $R - |z|$ plane, on the other hand, is depicted in Fig. 6.7 b). Figs. 6.7 c) and d) show the in-plane reach for red and blue stars respectively, where one can see that the maximal reach in $|180° - \phi|$ is reduced slightly for the redder population.

Table 6.1: The relative uncertainty in parallax, σ_ϖ/ϖ, for each quadrant of the analysis after applying the standard set of cuts enumerated in Fig. 6.4 with $R \in [7, 9]$ kpc and $z \in [0.2, 3]$ kpc — and as also employed in Gardner, Hinkel, and Yanny (2020).

	Left	Right	Total
North	0.101	0.074	0.087
South	0.072	0.098	0.085
Total	0.086	0.086	0.086

Consideration of Systematics

In order to assess the impact of various systematic effects on our data, we explore a number of different possibilities and estimate the degree to which they could cause a false asymmetry signal. First, due to the fact that we use Galactic azimuth values for each star, this necessitates that a parallax and thus a distance is known for the star. As such, this requirement eliminates all sources in the *Gaia* database which have a 2D "fall-back" astrometric solution only. Further, as we require color cuts for the completeness arguments we have outlined, we also miss stars with null entries for $G_{\text{BP}} - G_{\text{RP}}$. We have explicitly checked via a statistical query of the *Gaia* database that the asymmetry such an effect could cause would be $|\mathcal{A}_{\text{null } \varpi \text{ \& color}}| \approx 0.0017$

for our G and $|b|$ requirements. However, the preponderance of these stars lie outside our sample volume. Indeed, in a Bayesian analysis to associate a distance with the 2D fallback solution, a prior used for the stars with poor astrometric measurements assumes a small parallax (Michalik et al., 2015), and therefore a large distance. Moreover, as we discuss further below, a Hubble Space Telescope comparison study suggests our sample is essentially 100% complete. Therefore, the value given above is a gross overestimate, and taking the estimated incompleteness conservatively into account suggests that the estimated size of this systematic effect to be no more than $|\mathcal{A}| \sim 2 \times 10^{-4}$.

Next, it is a well known feature of the *Gaia* telescope that its orbital motion corresponds to certain parts of the sky being imaged more than others (Lindegren et al., 2018), hence the streaks seen when relative parallax error restrictions are made (Luri et al., 2018). However, this discrepancy in the number of observations does not affect whether or not a relatively close star is seen at all. In fact, the completeness of the *Gaia* data for relatively close stars has been checked against 2MASS and has been found to be about 99% complete for data selections not too dissimilar from ours (Bennett and Bovy, 2018).

Further, the completeness of the *Gaia* data has been checked against the Hubble Space Telescope for dense fields in Arenou et al. (2018) and, for the range of magnitudes and latitudes considered here, is essentially 100% complete. In other words, by cutting away the densest regions of the sky and the dimmest stars, we are not affected by the completeness issues that often plague stars with such parameters.

Although the average angular densities considered in our analysis are all well within the range of safe values suggested by Arenou et al. (2018), one might worry that very localized lines of sight could exceed these density limits and result in small incomplete regions. We explicitly check this by zooming into the distribution of stars in l, b to search for small over-densities. We do find such regions, but we estimate that the impact of the stars missed in such cases on $\mathcal{A}$ to be extremely small. We study a worst case scenario by studying stars near $|b| = 30^\circ$ near the GC, gauging the expected level of completeness as detailed by Arenou et al. (2018). We find very localized areas with source densities near 4×10^5 stars per square degree. Such a missing population of stars cannot possibly account for the symmetry breaking we see, as simply counting the overdense regions on each side of the $\phi = 180^\circ$ line yields an estimated asymmetry of $|\mathcal{A}| \approx 0.000013$.

Another possible systematic comes from the parallax offset. To first order, the parallax offset is assumed to be the same for stars in all directions, magnitudes, colors, etc. As such, there would be no differences left or right, and thus no contribution to the asymmetry. If instead the shift varies slightly on the sky, a small, $\mathcal{O}(0.01)$ mas correction to nearby stars would correspond to a distance shift of about 10 pc, or about 1% of the typical distance to a star in our sample. If this effect were truly an issue, the completeness checks we have performed would likely have exhibited some sort of noticeable fluctuation as stars with a different, true offset would have shifted into or out of our sample; we see no evidence of this.

Finally, the *Gaia* data obviously exhibits scan lines when relative parallax uncertainty quality cuts are implemented, so that one may be tempted to think that

scan lines may also be hidden in the completeness plots at a level not detectable to the human eye. To test this possibility, a number of tests were devised. First, upon zooming into small regions of l, b in our data where there are known streaks of incompleteness in the separate, relative parallax error data, as in Fig. 6.2 a), we see no signs of any scan lines. Further, we numerically test this possibility by examining the expected asymmetry in our data set along the lines of sight toward a known streak in the relative parallax error data. The local, worst-case asymmetry is $|\mathcal{A}| = 0.007$, and since the "would-be" streaks constitute a small fraction of the sky and are on both sides of the $\phi = 180°$ line, the expected, total asymmetry from any such effect is smaller still, perhaps something like a tenth of the worst case local measurement, $|\mathcal{A}| = 0.0007$.

Tallying the impact of the various systematic effects we have considered we estimate the total systematic error to be no larger than $|\mathcal{A}_{\rm sys}| \sim 0.0009$. We note that this is substantially smaller than the asymmetry effects we have observed.

Splitting the sample into three radial bins

Since Gardner, Hinkel, and Yanny (2020) studied the axial asymmetries for our aggregate sample and argued for a dominant role by the LMC & SMC in interpreting the results seen, we first split the sample into three R bins, $7 < R < 7.7$, $7.7 < R < 8.3$, and $8.3 < R < 9.0$ kpc in order to see if the asymmetry is constant with R. If the asymmetry were due entirely to the LMC, which because of its distance, would act over a relatively large coherent area on mass in the Milky Way, we would expect the $\mathcal{A}$ trends with ϕ to be similar in the three bins. Perhaps surprisingly, after dividing the sample into three radial bins, one instead notices marked differences in the shapes of the various asymmetry curves in Fig. 6.8 with ϕ. These marked differences can potentially be understood as a superposition of two effects. First, given that the disk scale length is $R_s \approx 2$ kpc (Bovy and Rix, 2013), the contribution of the halo to the total, N+S asymmetry (blue diamonds) is less pronounced in the inner region with more disk stars. The second effect we resolve is in only the two lowest R bins. In the innermost case, the left-heavy asymmetry differs in sign from the model matter distribution with a distorted halo(Erkal et al., 2019) that can confront the shape of the aggregate data fairly well (Gardner, Hinkel, and Yanny, 2020). Interestingly, such a R variation in the asymmetry could qualitatively be an expected signal from an Outer Lindblad Resonance (OLR) of the Galactic bar, where we note Figure 1 of Dehnen (2000) and the explanations of Contopoulos and Papayannopoulos (1980), or perhaps the Co-rotation resonance (CR) of the Galactic bar — as we discuss further below. Given that such effects are not axially symmetric, our method is sensitive to them and thus we may be able to discriminate between these two possibilities.

Masking out the GC and Removing Dimmer Stars

Given that the GC direction has an extremely high number of stars per solid angle, the *Gaia* telescope may have issues accurately measuring parallaxes and correctly identifying stars in this region. With this thought in mind, we check our radially-

separated results by cutting away the stars most likely to be biased by such an effect. Namely, we do this via three alternative methods: lowering our faintness cut to $G < 17$ mag, excising the GC via "box" cuts in l and b, and utilizing both of the aforementioned cuts in tandem.

For the first method, we see from Fig. 6.9 that the two outermost radial bins do not change appreciably, which matches what one would expect given that the crowded regions of the sky do not subtend a large portion of the geometry there. For the innermost R bin in panel a), however, the GC is behind nearly all of the data. Minding the "hazy" G-band magnitude completeness limits of the *Gaia* telescope (Lindegren et al., 2018), we cut out the dimmest stars in order to test whether or not incompleteness affects the data. The N+S (blue diamonds) data does not change appreciably, while the N and S only curves become only slightly closer to zero.

For the second method, we choose to excise the densest region of the l, b plot in Fig. 6.2 b). To wit, we cut out all stars within 20° of the $l = 0°$ line, which also satisfy $|b| < 45°$. The results of this check are shown in Fig. 6.10, where it is apparent that there is no appreciable change in any of the bins. Additionally, Fig. 6.10 d) shows the altered xy footprint with the GC-masking l, b cuts employed.

For the third and final method of checking that our result is not appreciably afflicted by completeness and stellar identification issues in the dense GC region, we implement both the magnitude and "box" cuts mentioned above and show these results in Fig. 6.11. Clearly, the largest R bin is unaffected by the l, b cuts and is identical to Fig. 6.9 c). The intermediate R bin (Fig. 6.11 b)) shows no appreciable change. Interestingly, the innermost R bin appears to exhibit a wave-like N+S asymmetry[2], a feature that was not as easily identifiable with the likely more poorly measured GC-direction stars and dim stars included. Otherwise, the general trend remains mostly similar to the main result and the other tests.

Comparison of stricter cuts on the aggregate asymmetry result

In order to assess if the additional cuts outlined in § 6.2 appreciably change the resulting, aggregate asymmetry found in Gardner, Hinkel, and Yanny (2020), we apply the same GC masking to the aggregate data set in Fig. 6.12. Clearly, the results do not change qualitatively at all, and there is only a negligible quantitative change in the signal we find for each set of cuts. This fact allows us to conclude that potentially poorly measured stars in the denser regions of the sky near the GC are not responsible for the asymmetry we see.

Red and blue color cut analysis

Using only the nearest volume subset of our sample in order to isolate color-dependence (see Fig. 6.13 caption for cuts), we see that the behavior of the red stars (Fig. 6.13a) and the blue stars (Fig. 6.13b) are both consistent with a downward trend in the N+S

[2]Although the asymmetries associated with innermost and outermost radial bins of Fig. 6.11 appear to suggest wave-like features, a reduced chi-squared analysis reveals that Fig. 11 a) contains the only statistically significant wave-like effect.

(blue diamonds) data, lending support to an overall distortion of the shape of the potential which is affecting all stars. There are, however, slight differences between the red and blue stars for the N-S data. This may be due to some effect seen only in the older, redder population, but we do not speculate on the specific cause.

Height above the plane analysis

Finally, upon dividing the sample into subsets above and below $|z| = 0.5$ kpc, as in Figs. 6.14 a) and b), respectively, one notices that the downward trend in the N+S data set (blue diamonds) appears to be much more marked for the low $|z|$ stars, seemingly revealing behavior at odds with what one would expect if a distorted halo were the main cause of the asymmetry. However, we have carefully removed the spiral arms via our b and z cuts. We note, however, that the low-z stars preferentially sample the region of R close to the Sun due to the geometry of the latitude cuts imposed on the sample. Indeed, this behavior is completely consistent with a picture in which the OLR is inside the solar circle, as one would expect the low-$|z|$ stars near $R = R_0$ to exhibit negative values of the asymmetry, due to the tendency of orbits to align with the bar just outside of the OLR (Binney and Tremaine, 2008). In contrast, the more marked N-S difference for the high-$|z|$ stars is consistent with a tilted prolate halo.

6.3 Results

As evident from Figs. 6.12 and 6.8, our results do confirm the findings of Gardner, Hinkel, and Yanny (2020), interpreted as an overall effect due to the LMC & SMC system, but also reveal R-dependent features. In particular, the sign flip in the asymmetry in Fig. 6.8 as one looks closer to the GC suggests that another object contributes in that region. Given that the second most significant perturber noted by Gardner, Hinkel, and Yanny (2020) is the Galactic bar, and that the signal occurs at smaller R, the Galactic bar is the most likely culprit.

In fact, due to the non-axisymmetric, time-dependent nature of the Galactic bar potential, resonances can occur at very specific galactocentric radii (Binney and Tremaine, 2008). While the existence of a family of stars in bar-resonant orbits depends strongly on the relative strength of the Galactic bar, it is the case for all but the strongest of bars that resonant orbits between the Co-rotation Resonance (CR) and the Outer Lindblad Resonance (OLR) orbit with trajectories perpendicular to the bar, and beyond the OLR the resonant orbits tend to be elongated along the bar's orientation (Contopoulos and Papayannopoulos, 1980; Binney and Tremaine, 2008). This non-axisymmetric behavior could easily be responsible for the sign-flip we see in Fig. 6.8, as there has long been a notion that a resonance occurs just interior to the solar circle (Mishurov and Zenina, 1999; Dehnen, 2000, e.g.). Interestingly, given that the location of the Galactic bar is known, we believe that the pattern of axial asymmetries we see, that $\mathcal{A}$ flips sign from positive to negative, rather than from negative to positive, indicates that the effect is an Outer Lindblad Resonance.

Finally, given the importance of Sagittarius in exciting vertical motions in the Galactic disk (Widrow et al., 2012; Yanny and Gardner, 2013; Laporte et al., 2018b), one might ask if it, too, could have an effect axially on our sample. However, due to the alignment of the perturber and stars in our sample, the z-component of the torque would be very small, as the displacement vector and force vector are very nearly aligned, yielding a severely less significant torque. We expand upon the possible impact of the evolutionary history of the Sgr dwarf and stream below.

Thus the axial asymmetry profiles we have found appear consistent with two overarching effects: first, a matter distribution warped by the LMC & SMC, as suggested by the distorted halo model determined from studies of the Orphan stream by Erkal et al. (2019), and second, an asymmetry associated with an Outer Lindblad Resonance driven by the Galactic bar.

In the distorted halo model, the dark halo of the Milky Way is stretched by the LMC/SMC system, causing an elongation in the direction of the Magellanic clouds (Erkal et al., 2019). With the Miyamoto-Nagai disk (Miyamoto and Nagai, 1975) and distorted NFW halo profile (Navarro, Frenk, and White, 1997) of Erkal et al. (2019) integrated over the same region as our data set, the N only, S only, and N+S data sets all qualitatively match a reflex prolate distribution much better than the other halo geometries offered (Gardner, Hinkel, and Yanny, 2020). As we have mentioned in Gardner, Hinkel, and Yanny (2020), this halo geometry is also consistent with the galactic warp picture of Weinberg and Blitz (2006) and Dekel and Shlosman (1983).

It is perhaps disconcerting, though, that upon dividing the data set into radial or vertical bins, the allegedly global asymmetry effect of a distorted matter distribution is not seen at the same level in each bin. Indeed, the vertical-axial correlation and N+S trend of Fig. 6.8 a) is reversed from what is expected, while panels b) and c) still fit well with this picture. Additionally, as can be seen from Fig. 6.14 the axial asymmetry is largely seen in stars close to the plane, the opposite of what one would expect for a halo-driven effect. However, due to the nature of the $|b|$ cuts implemented here, different bands of $|z|$ sample different values of R, as can be understood from Fig. 6.7 b). Thus, it is possible that the z-dependence is confounded by sampling different values of R. Regardless, the picture of Magellanic cloud influence alone cannot explain the innermost R bin, and thus requires some additional effect. This effect is likely from the Galactic Bar as it is only seen at the innermost R bin. Indeed we believe it to be the result of the presence of the Outer Lindblad Resonance (OLR). This effect, believed to be just inside the solar circle (Dehnen, 2000), can cause perturbations to stars just inside (outside) the OLR which causes them to align themselves in a perpendicular (parallel) sense with respect to the bar (Contopoulos and Papayannopoulos, 1980; Dehnen, 2000). Given that the Galactic Bar is known to point at approximately $13 - 27°$ from the Sun's location (Robin et al., 2012; Portail, 2016), this orbital alignment configuration would give rise to an axial asymmetry which is Left-heavy ($\mathcal{A} > 0$) for values of R just inside the OLR, and Right-heavy ($\mathcal{A} < 0$) for values of R just outside the OLR, and no net effect well beyond the OLR. This qualitatively matches the results of Fig. 6.8. Note that if the effect were a Co-Rotation resonance, the asymmetry ought to flip from negative to positive.

It is unclear exactly how the stars near the OLR can behave in such a way to

also cause a N-S asymmetry, but it has been noted that the vertical resonance from a central bar can have significant effects on the vertical amplitudes of orbits near the Inner Lindblad Resonance (Quillen, 2002; Hasan, Pfenniger, and Norman, 1993), so that such an effect near the OLR could well also occur.

Upon consideration of the above effects, it seems most likely that both Magellanic torque and bar induced resonances are operative in the local star count data. The OLR creates a Left-heavy asymmetry in the innermost R bin and constructively interferes with the LMC & SMC-driven (halo) effect in the middle R bin. Finally, the OLR ceases to play a large role at higher R and the halo effect is the lone cause of the signal we see.

We have determined the location of the in-plane radius at which the axial asymmetry, N+S, flips sign as follows. We compute the asymmetry $\langle \mathcal{A}(\phi) \rangle$, making an error-weighted average over azimuthal angles such that $|180° - \phi| < 6°$, where $\mathcal{A}(\phi)$ itself counts up stars in a wedge of width ΔR, for various choices of starting radius R_i. We refine the determined radius at which $\langle \mathcal{A}(\phi) \rangle$ flips sign through an iterative procedure. That is, we begin with wedges of width $\Delta R = 500$ pc and move outward in R_i by 200 pc increments, to determine where the average asymmetry changes sign. After observing a sign flip, the radial width of each bin is decreased, and the scan repeated over a smaller range of R_i to sharpen the determination of the radial location of the sign flip. The uncertainty is derived from the smallest radial wedge, of 200 pc, which still reveals a sign flip in the asymmetry at a magnitude larger than the combined uncertainty in $|\langle \mathcal{A}(\phi) \rangle|$, where the statistical error in $\langle \mathcal{A}(\phi) \rangle$ and the systematic error $|\mathcal{A}_{\rm sys}| = 0.0009$ have been combined in quadrature. Noting Table 7.1, and picking the midpoint of the $R_i - R_f$ bin with the smallest asymmetry for a ΔR of 200 pc we have determined that $R_{\rm flip} = (0.95 \pm 0.03) R_0$. Our sign flip analysis uses the data set of Gardner, Hinkel, and Yanny (2020) and implicitly assumes that only one effect is operative in the data. However, we also expect the distorted halo to make some contribution as an overall negative offset to the asymmetry. This offset, determined at larger R, is small and implies $R_{\rm OLR} > R_{\rm flip}$. This effect, as well as other refinements in our determination of $R_{\rm OLR}$, and its implications, we plan to analyze in a future paper (Hinkel, Gardner, and Yanny, 2020a)

The OLR picture allows for a number of follow-up studies. First, if the outer Lindblad resonance is responsible for the behavior we observe at smaller R, we should be able to connect the asymmetry to a radial velocity difference between stars on the left and right of the $\phi = 180°$ line. Studying the axial asymmetry about values of ϕ other than $\phi = 180°$ could also be revealing, as the stellar orbits just within and beyond the OLR have crossing points in ϕ. Moreover, in this picture we would also not expect to find significant variation of the axial asymmetry with R beyond the Sun's location, which we hope to investigate further, including with the upcoming *Gaia* DR3 data set.

Finally, we consider whether past effects of the Sgr. dwarf galaxy's collision with the Milky Way could cause an appreciable signal in our data set. Since the mass used

Table 6.2: Axial asymmetries, N+S, averaged over azimuth angles about the anti-center direction up to $|180° - \phi| = 6°$, computed for a wedge of size ΔR for different choices of starting radius R_i, with $R_f = R_i + \Delta R$, to reveal the sign change in the average asymmetry as $R_i - R_f$ changes. We refine the location of the sign flip iteratively by computing the average asymmetry with R_i for smaller ΔR.

$R_i - R_f$ (kpc)	ΔR (kpc)	$\langle \mathcal{A}(\phi) \rangle$	$\sigma_{\langle \mathcal{A} \rangle}$	Sign
7.0 - 7.5	0.5	+0.0071	0.0012	+
7.2 - 7.7	0.5	+0.0035	0.0011	+
7.4 - 7.9	0.5	-0.0027	0.0011	-
7.3 - 7.6	0.3	+0.0049	0.0012	+
7.4 - 7.7	0.3	+0.0017	0.0012	+
7.5 - 7.8	0.3	-0.0019	0.0012	-
7.45 - 7.65	0.2	+0.0030	0.0013	+
7.5 - 7.7	0.2	+0.0005	0.0013	+
7.55 - 7.75	0.2	-0.0019	0.0012	-

in Gardner, Hinkel, and Yanny (2020) referred to the present day core of the Sgr dwarf spheroidal, it is interesting to ask if its more massive past self (estimated by Purcell et al. (2011) to have a mass of roughly $10^{10.5} - 10^{11} M_\odot$) could torque the disk appreciably. While it is true that Sgr would have applied a significant torque on the galaxy, the axial dispersion velocities of approximately 30 $\mathrm{km s^{-1}}$ (Purcell et al., 2011) ensure that any asymmetry incurred from the original impact before the significant mass losses of nearly 2 Gyr ago (Purcell et al., 2011) will have been diluted to cover an arc over 50 times larger, reducing the magnitude of any axial asymmetry signal to irrelevance for our volume of space in the present time. That the vertical motions of stars can be affected by Sagittarius, suggested in Widrow et al. (2012), Yanny and Gardner (2013), and Ferguson, Gardner, and Yanny (2017) is an entirely different matter.

With regard to the possible influence of the Sgr dwarf tidal stream of the present day we note that a recent impact of Sgr with the disk is very perpendicular to the plane of the disk and at roughly $\phi \approx 180°$, thus giving, as we have noted, nearly zero azimuthal torque on the stars in our sample. This leads us to argue that the LMC, while at a significantly greater distance from the sun than the Sgr tidal stream, induces a much larger left-right asymmetry than Sgr (or the bar if $R \lesssim 8$ kpc).

6.4 Conclusions

We support and expand upon the findings of Gardner, Hinkel, and Yanny (2020) regarding the existence and origin of axial asymmetries in star counts, strongly correlated with mass density in the solar neighborhood, using the Gaia DR2 data set. After making appropriately conservative cuts, we arrive at a complete, distance-error limited sample of stars, in matched left-right and North-South volumes, which show residual asymmetries in the counts of between 0.5% to 3%. We explore and rule out

possible incompleteness due to reddening, lines of sight polluted by regions of high stellar density, significant errors in parallax, magnitude and color limits, and other geometric cuts. Based on the estimated azimuthal torques applied to density in the solar neighborhood from Galactic and local group structure, we isolate the Magellanic Cloud system as capable of inducing the largest asymmetry for radii $7.7 < R < 9$ kpc, as shown in Gardner, Hinkel, and Yanny (2020). Recent increases in mass estimates for the LMC & SMC system (Erkal et al., 2019) give this perturber an outsized influence, compared with earlier estimates. Going beyond Gardner, Hinkel, and Yanny (2020), subdividing the data into three radial bins, we note that the lowest radial bin, $7 < R < 7.7$ kpc, exhibits a sign flip in the asymmetry incompatible with the Magellanic Cloud influence, but consistent with that expected from a bar-induced Outer Lindblad Resonance located slightly beyond $R = 7.6$ kpc ($R_{\rm flip} = (0.95 \pm 0.03)R_0$). While a detailed model which includes several perturbers simultaneously and which considers reflex back-reaction is needed to fully model the detailed asymmetries seen here, we have demonstrated the potential for precision studies of symmetry breaking to constrain and inform our knowledge of the overall mass distribution in and around our Milky Way.

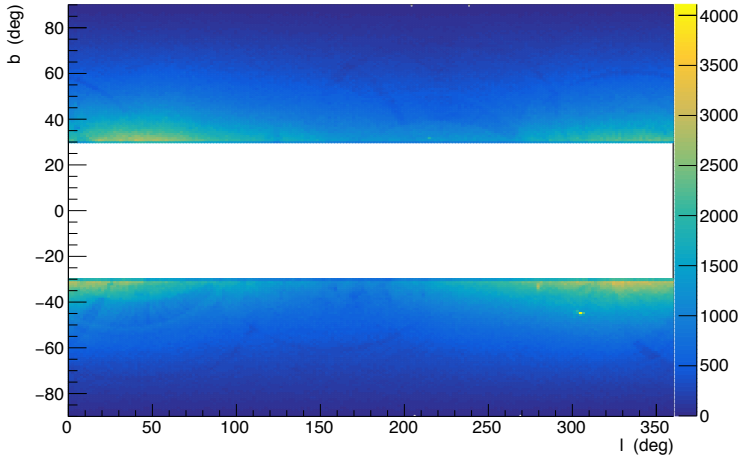

(a)

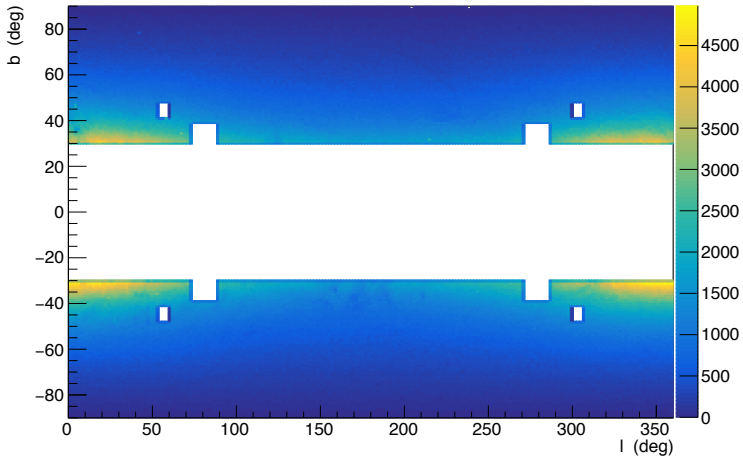

(b)

Figure 6.2: (a) A selection of data in (l, b) with relative parallax error cuts of $\sigma_\varpi/\varpi < 0.2$ applied. Notice the LMC and SMC "bleed" through, even though their stars are at significantly greater distances than expected from a simple lower limit cut on the parallax with its error; stellar identification issues in the crowded field may be the cause of this issue. There are also streaks of incompleteness in the data, a sign that *Gaia* did not measure stars in some regions of the sky with the same accuracy as others. (b) A selection of data in (l, b) with the LMC and SMC removed, as well as all reflections of the two satellite galaxies to prevent any bias in an assessment of L/R and N/S symmetry. The cuts used are as follows: $14 < G < 18$ mag, $0.5 < G_{BP} - G_{RP} < 2.5$, $\varpi > 0$ mas, $|b| > 30°$, $0.2 < |z| < 3$ kpc, and the LMC/SMC excisions as outlined in Eqs. 6.2 and 6.3. We note that some dust seems to survive the $|b|$ and $|z|$ cuts near the anti-center direction. We have checked our final result with and without excisions of this region and there appears to be no appreciable effect.

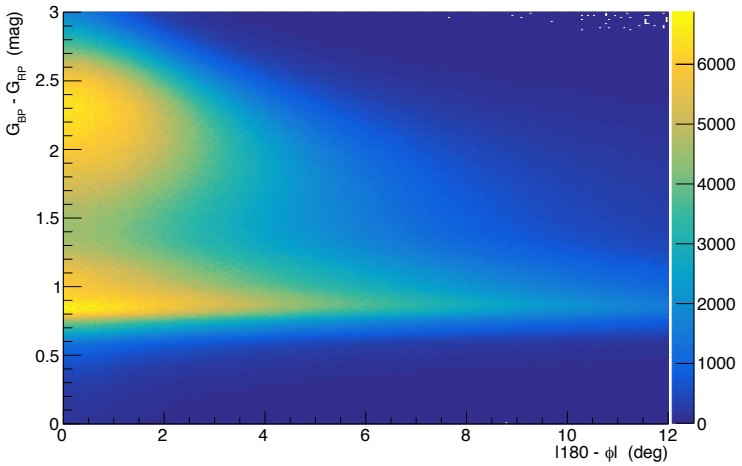

(a)

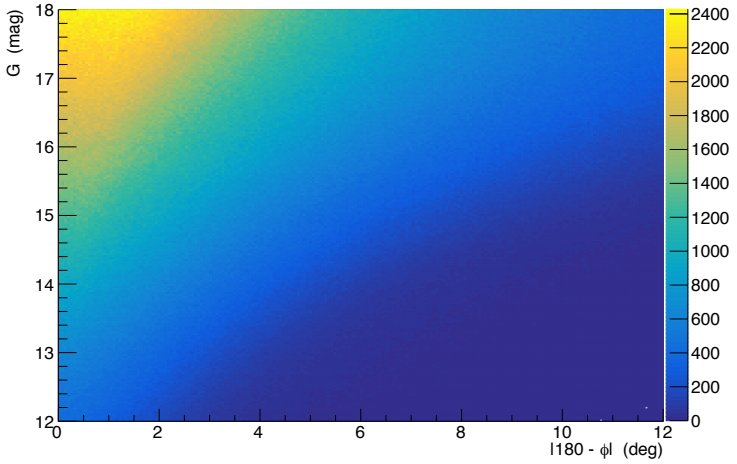

(b)

Figure 6.3: (a) $G_{\rm BP} - G_{\rm RP}$ versus $|180^\circ - \phi|$. For $0.5 < G_{\rm BP} - G_{\rm RP} < 2.5$ there appears to be significant statistical strength out to $|180^\circ - \phi| \approx 6^\circ$. The cuts used are as follows: $\varpi > 0$ mas, $|b| > 30^\circ$, and the LMC/SMC excision outlined in Eqs. 6.2 and 6.3. We note that the final results do not change appreciably upon changing the color cut from $G_{\rm BP} - G_{\rm RP} < 2.5$ mag to $G_{\rm BP} - G_{\rm RP} < 2.3$ mag. (b) G band magnitude versus $|180^\circ - \phi|$. For $G > 14$ mag there appears to be significant statistical strength out to $|180^\circ - \phi| \approx 6^\circ$. The cuts used are as follows: $0.5 < G_{\rm BP} - G_{\rm RP} < 2.5$ mag, $\varpi > 0$ mas, $|b| > 30^\circ$, and the LMC/SMC excision outlined in Eqs. 6.2 and 6.3.

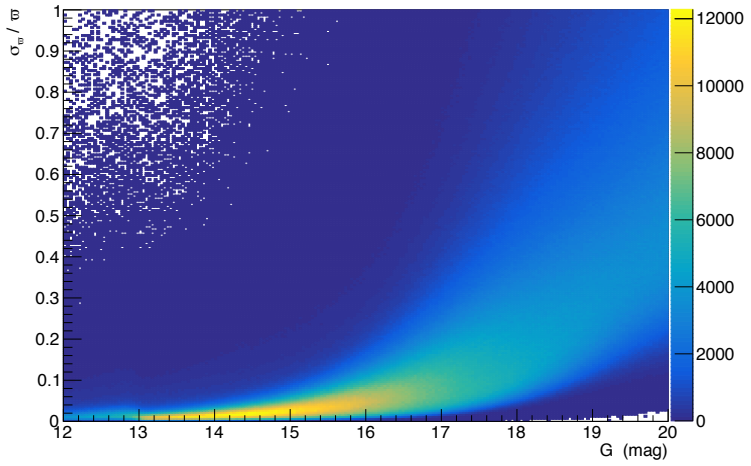

(a)

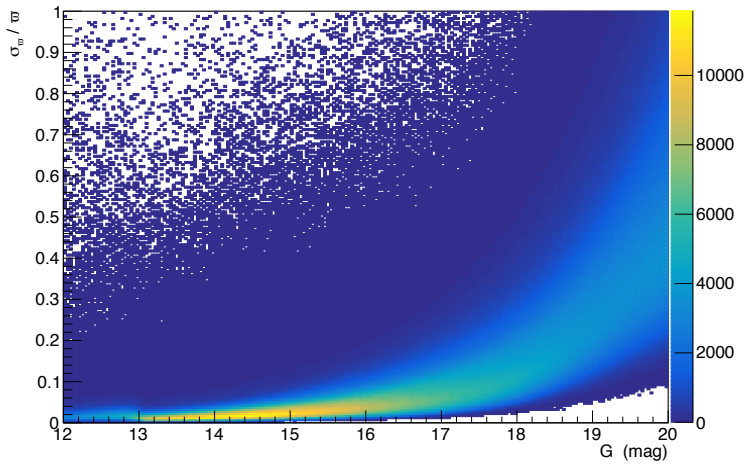

(b)

Figure 6.4: (a) The majority of stars with magnitude G have a relative parallax error that is reasonably small for $G < 18$ mag. The *Gaia* documentation mentions incompleteness in crowded fields and due to data processing and "filtering" for stars with $G > 17$ mag in crowded regions (Arenou et al., 2018); however, we avoid these regions and can thus extend our reach to fainter stars, as motivated in the text. The cuts used are as follows: $0.5 < G_{\rm BP} - G_{\rm RP} < 2.5$ mag, $\varpi > 0$ mas, $|b| > 30°$, and the LMC/SMC excision outlined in Eqs. 6.2 and 6.3. These are the "standard cuts" that we employ throughout our analysis. (b) The relative error in the parallax for our selection of stars, though without G restrictions. We manage to select stars with relatively well measured parallaxes without incurring the bias of cutting on relative parallax error explicitly. The cuts used are as follows: $0.5 < G_{\rm BP} - G_{\rm RP} < 2.5$ mag, $\varpi > 0$ mas, $|b| > 30°$, $7 < R < 9$ kpc, and the LMC/SMC excision outlined in Eqs. 6.2 and 6.3.

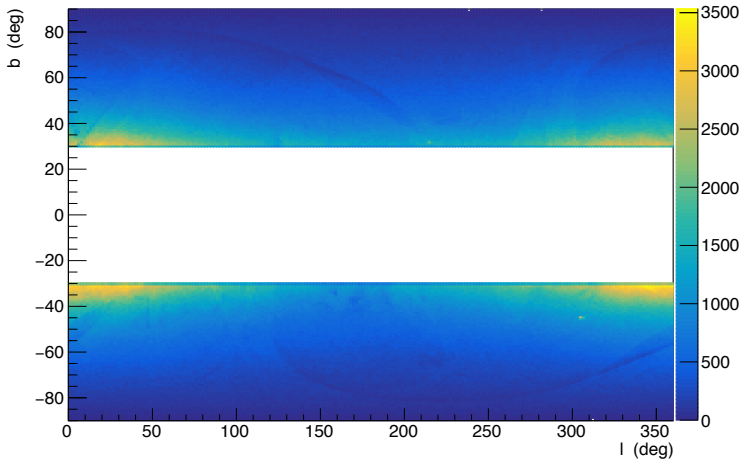

Figure 6.5: A study of stars within $\lesssim 3$ kpc with $|b| > 30^\circ$ and $G \in [14, 18]$ mag, but with restrictions on Astrometric Excess Noise (AEN) in place. All stars with an AEN value larger than 0.2 mas have been excised. Clearly, requiring such a quality cut would leave the sample with artificial asymmetries due to the streaks seen in many portions of the sky.

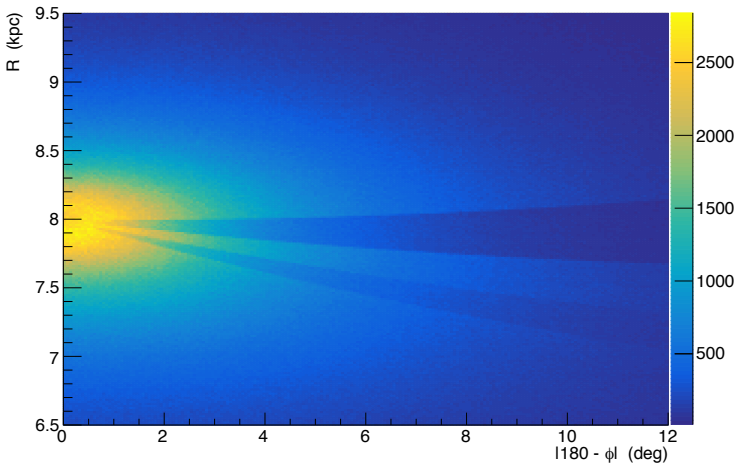

(a)

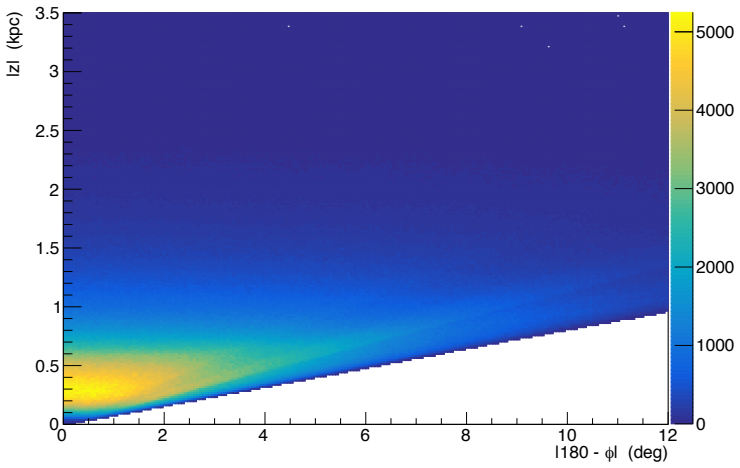

(b)

Figure 6.6: (a) R, ϕ completeness for the selected data. We choose to cut on $7 < R < 9$ kpc in order to achieve the best angular reach possible without compromising completeness. The cuts used are as follows: $14 < G < 18$ mag, $0.5 < G_{\rm BP} - G_{\rm RP} < 2.5$ mag, $\varpi > 0$ mas, $|b| > 30°$, and the LMC/SMC excision outlined in Eqs. 6.2 and 6.3. (b) Test of vertical completeness over ϕ. Cuts used: $14 < G < 18$ mag, $1.5 < G_{\rm BP} - G_{\rm RP} < 2.5$ mag, $7 < R < 9$ kpc, $\varpi > 0$ mas, and the LMC/SMC excision outlined in Eqs. 6.2 and 6.3.

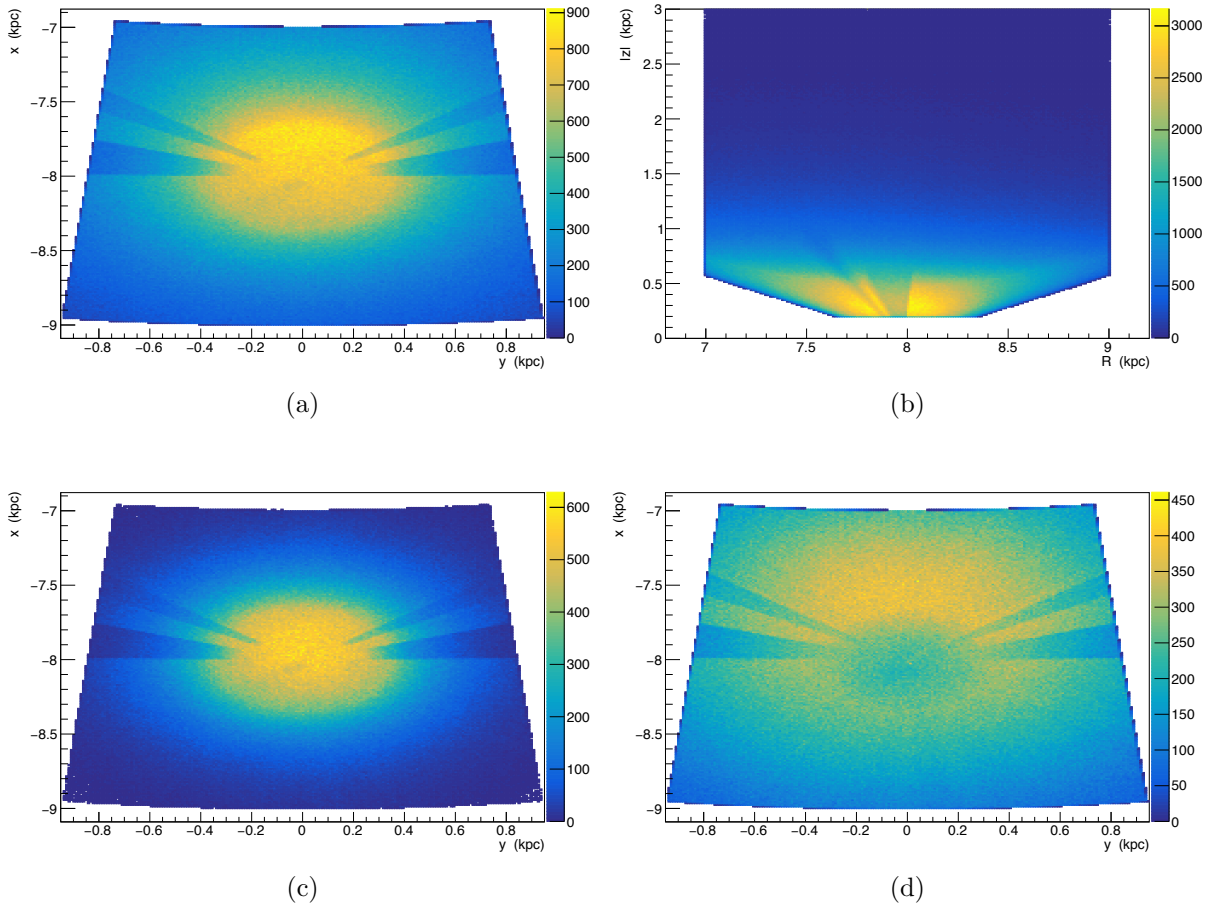

Figure 6.7: (a) The in-plane projection of our data with the cuts motivated above, as viewed from the South side of the plane. The data extends out to 6 degrees in galactocentric azimuth. (b) The geometry of our data selection in the $R - |z|$ plane. (c) The in-plane projection for red stars ($1.5 < G_{\rm BP} - G_{\rm RP} < 2.5$ mag). (d) The in-plane projection for blue stars ($0.5 < G_{\rm BP} - G_{\rm RP} < 1.5$ mag). All panels have the following cuts unless noted otherwise: $0.5 < G_{\rm BP} - G_{\rm RP} < 2.5$ mag, $14 < G < 18$ mag, $\varpi > 0$ mas, $|b| > 30°$, $7 < R < 9$ kpc, $0.2 < |z| < 3.0$ kpc, $|180° - \phi| \leq 6°$, and the LMC/SMC excision outlined in Eqs. 6.2 and 6.3.

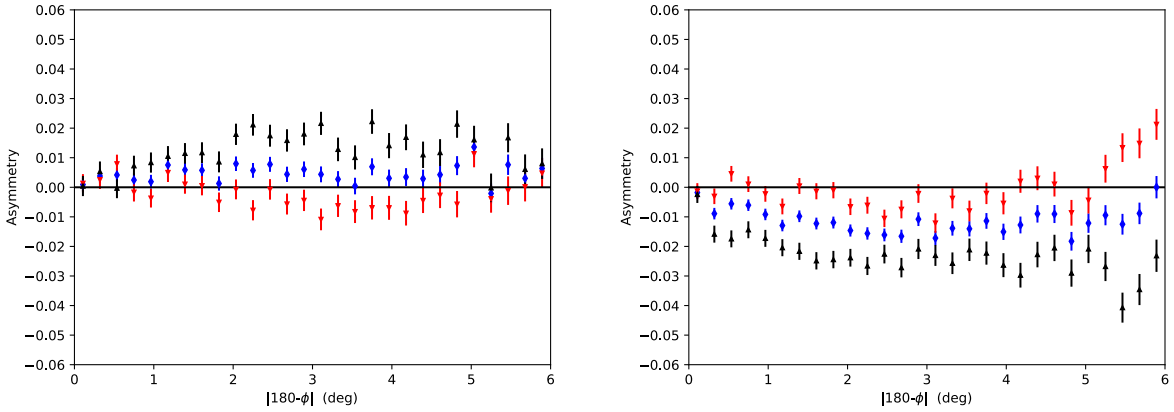

(a)

(b)

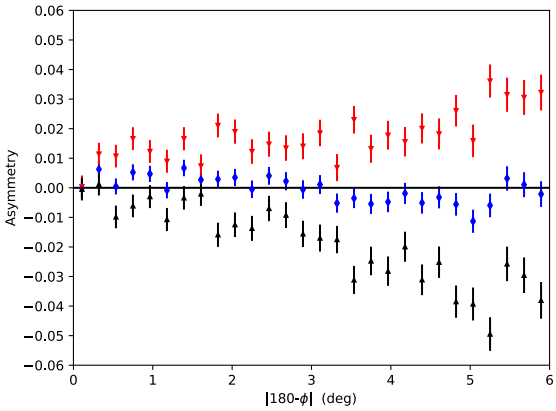

(c)

Figure 6.8: Dividing the data set into radial bins unveils a radial dependence for the North + South (blue diamonds), North only (black upward triangles), and South only (red downward triangles). (a) The axial symmetry test for stars with $R \in [7, 7.7]$ kpc. (b) The axial symmetry test for stars with $R \in [7.7, 8.3]$ kpc. (c) The axial symmetry test for stars with $R \in [8.3, 9]$ kpc. Additional cuts used in all panels are: $0.5 < G_{\rm BP} - G_{\rm RP} < 2.5$ mag, $14 < G < 18$ mag, $\varpi > 0$ mas, $|b| > 30°$, $0.2 < |z| < 3.0$ kpc, $|180° - \phi| \leq 6°$, and the LMC/SMC excision outlined in Eqs. 6.2 and 6.3.

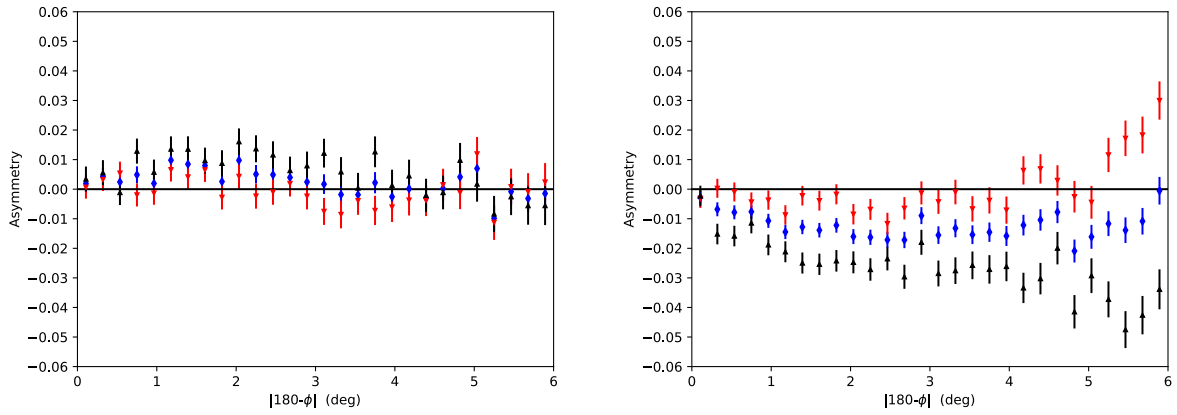

(a)

(b)

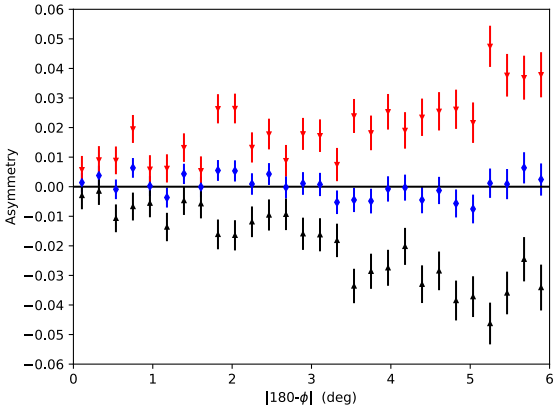

(c)

Figure 6.9: The radial study of the data set which include a stricter faintness limit of $G < 17$. (a) The axial symmetry test for stars with $R \in [7, 7.7]$ kpc. (b) The axial symmetry test for stars with $R \in [7.7, 8.3]$ kpc. (c) The axial symmetry test for stars with $R \in [8.3, 9]$ kpc. Additional cuts used in all panels are: $0.5 < G_{\rm BP} - G_{\rm RP} < 2.5$ mag, $14 < G < 17$ mag, $\varpi > 0$ mas, $|b| > 30°$, $0.2 < |z| < 3.0$ kpc, $|180° - \phi| \leq 6°$, and the LMC/SMC excision outlined in Eqs. 6.2 and 6.3.

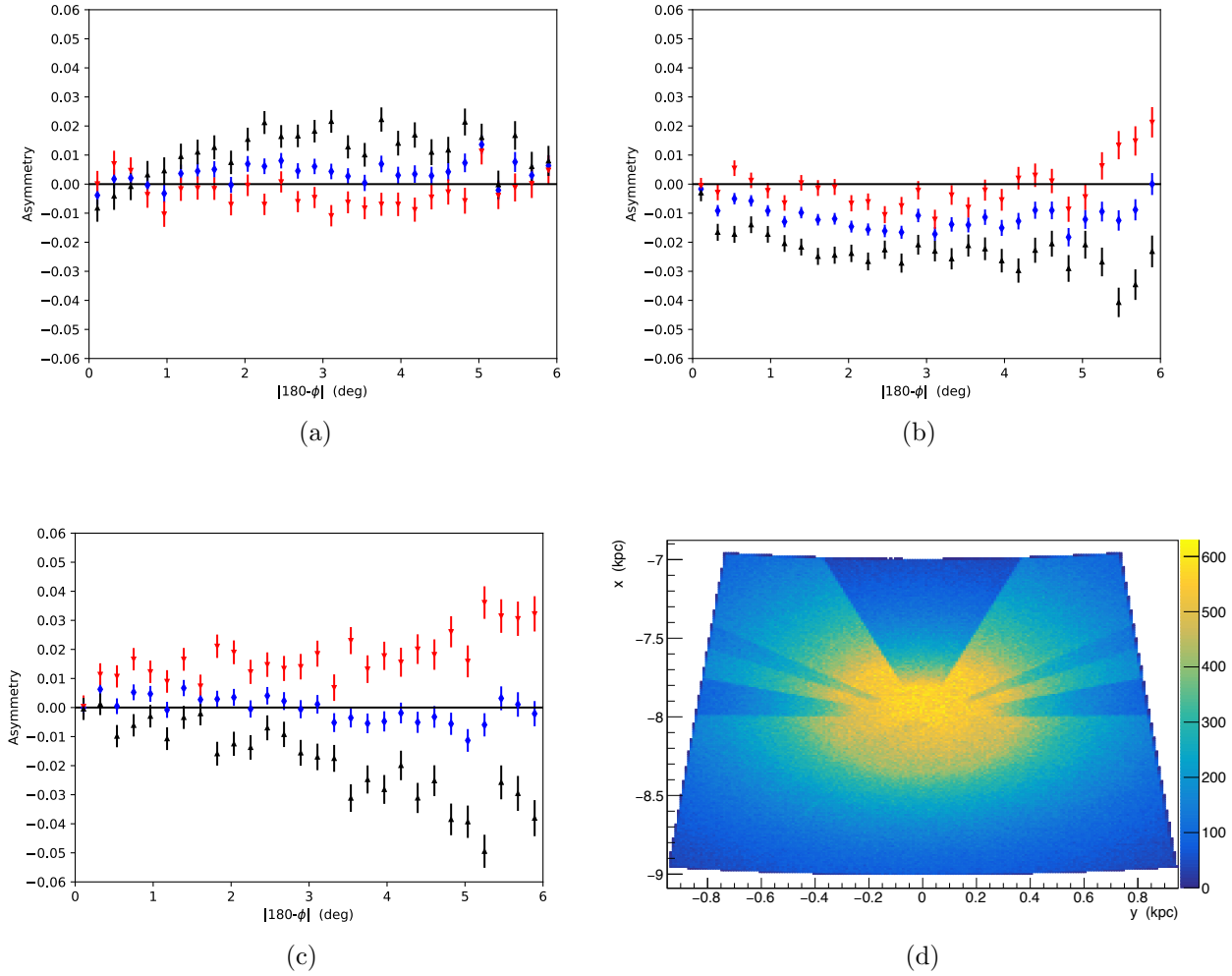

Figure 6.10: The radial study of the data set which has had the GC excised. (a) The axial symmetry test for stars with $R \in [7, 7.7]$ kpc. (b) The axial symmetry test for stars with $R \in [7.7, 8.3]$ kpc. (c) The axial symmetry test for stars with $R \in [8.3, 9]$ kpc is not affected by the GC excision and thus this is the same plot as Fig. 6.8 c). (d) The xy footprint of the data when the GC excision is included. Additional cuts used in all panels are: $0.5 < G_{\rm BP} - G_{\rm RP} < 2.5$ mag, $14 < G < 18$ mag, $\varpi > 0$ mas, $|b| > 30°$, $0.2 < |z| < 3.0$ kpc, $|180° - \phi| \leq 6°$, and the LMC/SMC excision outlined in Eqs. 6.2 and 6.3.

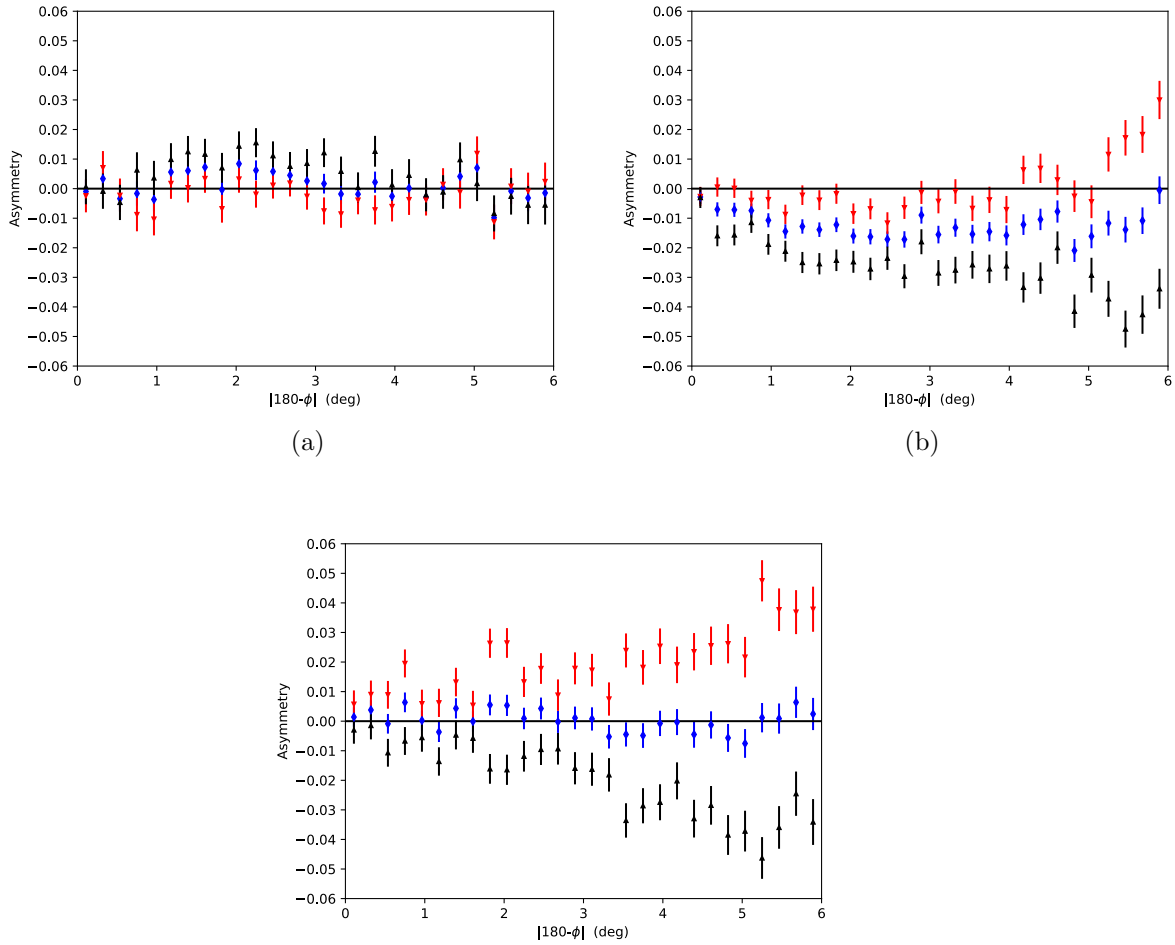

(a) (b)

(c)

Figure 6.11: The radial study of the data set which include a stricter faintness limit of $G < 17$ mag and the GC excision. (a) The axial symmetry test for stars with $R \in [7, 7.7]$ kpc. (b) The axial symmetry test for stars with $R \in [7.7, 8.3]$ kpc. (c) The axial symmetry test for stars with $R \in [8.3, 9]$ kpc is not affected by the GC excision and thus this is the same plot as Fig. 6.9 c). Additional cuts used in all panels are: $0.5 < G_{\rm BP} - G_{\rm RP} < 2.5$ mag, $14 < G < 17$ mag, $\varpi > 0$ mas, $|b| > 30°$, $0.2 < |z| < 3.0$ kpc, $|180° - \phi| \leq 6°$, and the LMC/SMC excision outlined in Eqs. 6.2 and 6.3.

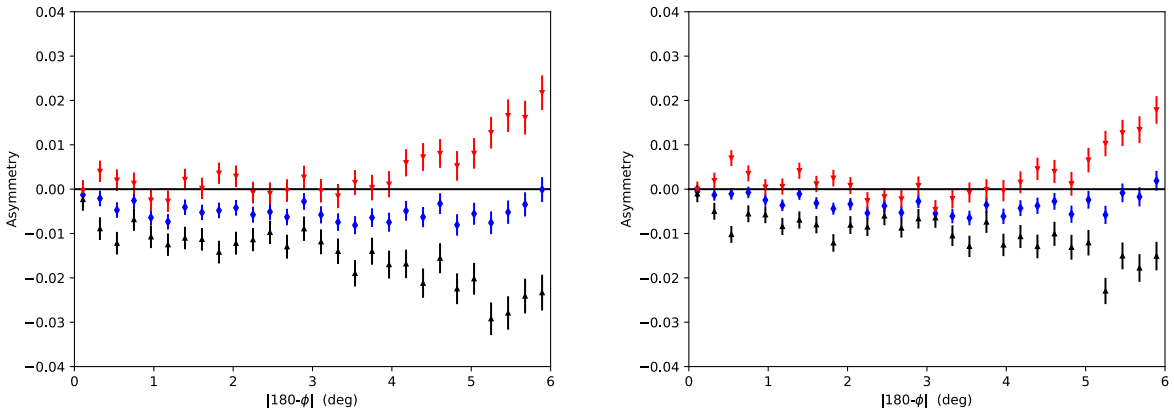

(a)

(b)

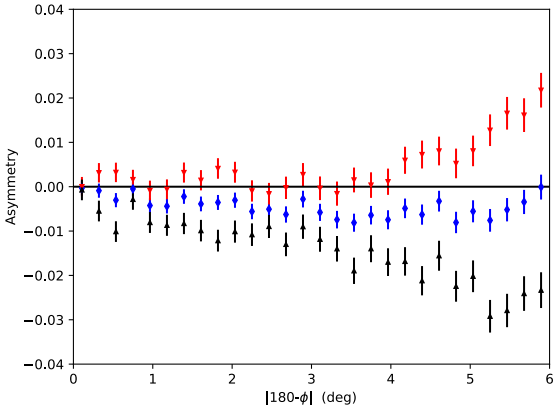

(c)

Figure 6.12: (a) Aggregate study of axial symmetry with $G < 17$ mag and the GC cuts of the above tests. (b) Aggregate study of axial symmetry from Gardner, Hinkel, and Yanny (2020) with $G < 18$ mag. (c) The same as panel (b), but with $G < 17$ mag. Additional cuts used in all panels are: $0.5 < G_{\rm BP} - G_{\rm RP} < 2.5$ mag, $\varpi > 0$ mas, $|b| > 30°$, $0.2 < |z| < 3.0$ kpc, $|180° - \phi| \leq 6°$, and the LMC/SMC excision outlined in Eqs. 6.2 and 6.3.

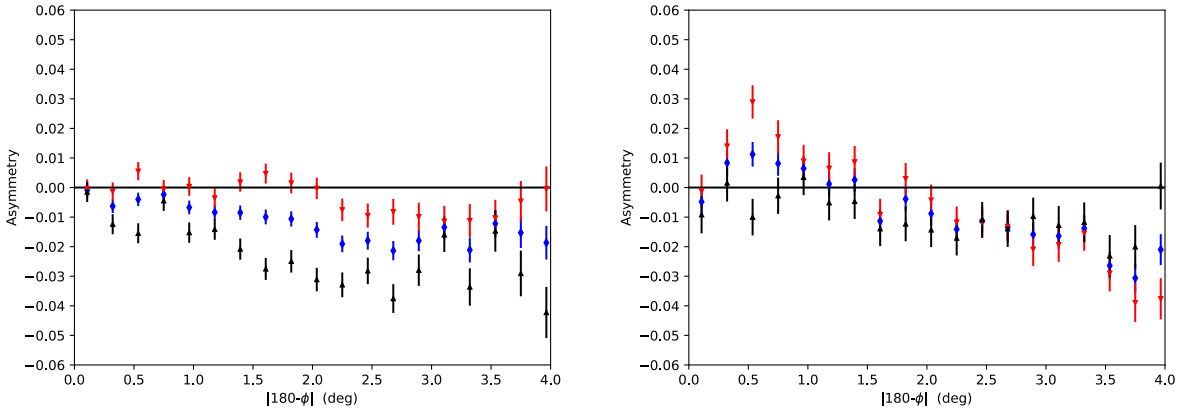

(a) (b)

Figure 6.13: (a) Test of axial symmetry with red ($1.5 < G_{\rm BP} - G_{\rm RP} < 2.5$ mag) stars only over a small volume of nearby space: $0.2 < |z| < 0.5$ kpc and $R \in [7.5, 8.5]$ kpc. (b) Test of axial symmetry with blue ($0.5 < G_{\rm BP} - G_{\rm RP} < 1.5$ mag) stars only over the same volume of space as panel a). Additional cuts used in both panels are: $\varpi > 0$ mas, $|b| > 30°$, $|180° - \phi| \leq 4°$, and the LMC/SMC excision outlined in Eqs. 6.2 and 6.3.

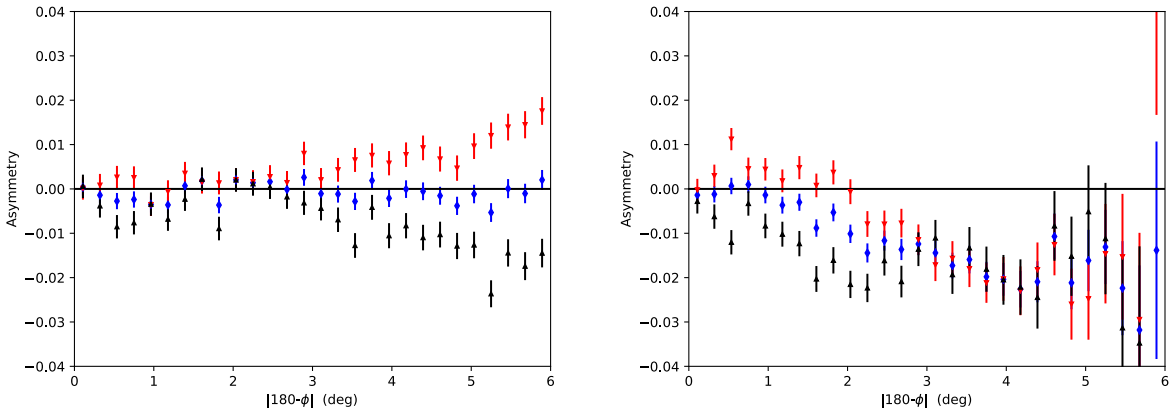

(a) (b)

Figure 6.14: (a) Far from plane sample, $0.5 < |z| < 3$ kpc. (b) Close to plane sample, $0.2 < |z| < 0.5$ kpc. Additional cuts used in both panels are: $0.5 < G_{\rm BP} - G_{\rm RP} < 2.5$ mag, $\varpi > 0$ mas, $|b| > 30°$, $7 < R < 9$ kpc, $|180° - \phi| \leq 6°$, and the LMC/SMC excision outlined in Eqs. 6.2 and 6.3. As the $|b|$ cuts cause these panels to sample very different swaths of R, this figure does not show z-dependence alone. The low-z stars preferentially sample the region of R close to the Sun due to the geometry of the latitude cuts, which is consistent with the asymmetry expected from the region just beyond the OLR.

Chapter 7 Axial Asymmetry Studies in Gaia Data Release 2 Yield the Pattern Speed of the Galactic Bar

7.1 Introduction

It is well established that there is a bar at the center of the Galaxy (Gerhard and Wegg, 2015) and that this structure rotates in a manner such that its stars and dust have net motion in the bar rest frame (Binney and Tremaine, 2008). The pattern speed, Ω_p, is the assessment of this rotation of the bar's potential, and models of that unknown potential are ordinarily needed in order to explain the motion of certain stellar populations to infer properties of the bar. This theoretical barrier, along with observational issues associated with high source densities, extinction, and reddening in the central region of the Galaxy, have resulted in a wide array of values, differing by more than a factor of two, for Ω_p (Bland-Hawthorn and Gerhard, 2016). To illustrate, various methods (Dehnen, 2000; Debattista, Gerhard, and Sevenster, 2002; Chakrabarty, 2007; Minchev, Nordhaus, and Quillen, 2007; Antoja et al., 2014) favor a fast bar, such as the pattern speed of $\Omega_p = 57.4^{+2.8}_{-3.3}$ km s^{-1} kpc^{-1} (Chakrabarty, 2007), whereas studies in the Galactic bar region (Portail et al., 2015; Portail et al., 2016; Sanders, Smith, and Evans, 2019; Bovy et al., 2019) can find considerably slower values, such as $\Omega_p = 25 - 30$ km s^{-1} kpc^{-1} (Portail et al., 2015). Bearing in mind the varied pictures and mechanisms employed in determining the pattern speed, the review of Bland-Hawthorn and Gerhard (2016) give a recommended range of $\Omega_p = 43 \pm 9$ km s^{-1} kpc^{-1}. A model-independent method of measuring the pattern speed that utilizes the continuity equation does exist, however, if the pattern is steady (Tremaine and Weinberg, 1984; Debattista, Gerhard, and Sevenster, 2002; Sanders, Smith, and Evans, 2019) but implementing it requires proper motion information for stars in the Galactic Bar. Recently Sanders, Smith, and Evans (2019) have used *Gaia* Data Release 2 (DR2) and VISTA Variables in the Via Lactea (VVV) data (Minniti et al., 2010) to find $\Omega_p = 41 \pm 3$ km s^{-1} kpc^{-1}, where the error is statistical only, with an additional suggested systematic uncertainty of $5 - 10$ km s^{-1} kpc^{-1}.

The wide range of reported pattern speeds is also partly responsible for the wide range of radii associated with resonant effects driven by the Galactic bar: that is, the radius of the Outer Lindblad resonance (OLR) and the radius of the corotation resonance (CR). As such, it is unclear whether the stellar streams seen in the solar vicinity (Raboud et al., 1998; Dehnen, 1999; Fux, 2001; Sellwood, 2010) are due to a CR (e.g. Mishurov and Zenina, 1999) or an OLR (e.g. Dehnen, 2000) or a $4:1$ OLR (Hunt and Bovy, 2018). Until recently (Hinkel, Gardner, and Yanny, 2020b), there

This chapter was originally published in the *Astrophysical Journal Letters*, and is reproduced with permission. The published article can be found here: Hinkel, Austin, Susan Gardner, and Brian Yanny. "Axial Asymmetry Studies in Gaia Data Release 2 Yield the Pattern Speed of the Galactic Bar." The *Astrophysical Journal Letters* 899.1 (2020): L14. doi: https://doi.org/10.3847/2041-8213/aba905

has been no model-independent way of discriminating between the possibilities in the existing data.

This lack of consensus regarding the pattern speed may come, in part, from the use of astrometric/photometric methods (Debattista, Gerhard, and Sevenster, 2002; Sanders, Smith, and Evans, 2019; Bovy et al., 2019) or of dynamical methods (Englmaier and Gerhard, 1999; Portail et al., 2015; Portail et al., 2016), and this spills over into the debate on the location of the resonances of the Galactic bar. Moreover, it has been suggested that the inconsistencies between the two sorts of methods can be reduced by having the bar rotate at a slower speed today than it has in the past (Monari et al., 2017). The findings of Sanders, Smith, and Evans (2019) may yield a simpler explanation: systematic effects from dust, e.g., tend to lower assessments of the pattern speed artificially, especially when observations of stars from the far side of the galactic center are used. Namely, Sanders, Smith, and Evans (2019) find $\Omega_{\rm p} = 41 \pm 3$ km s^{-1} kpc^{-1} and $\Omega_{\rm p} = 31 \pm 1$ km s^{-1} kpc^{-1} for stars in the near side of the bar and in both the near and far sides, respectively, providing the basis for their systematic error assessment. Alternatively, Hilmi et al. (2020) suggest that the bar's length and pattern speed can fluctuate by as much as 20% as the bar interacts with nearby spiral arms, perhaps explaining the different estimates of $\Omega_{\rm p}$ from different methods. Hilmi et al. (2020) note that the pattern speed as inferred from outer disk dynamics should reveal the time-averaged value of $\Omega_{\rm p}$, as opposed to instantaneous values measured in the central region via astrometric or photometric methods.

For a given galactic rotation curve, the pattern speed sets where these resonances are located. Thus, the determination of a resonant radius can also be used to fix the pattern speed, with information on additional resonant radii giving further information on the morphology of the bar. As motivated by leading order perturbation theory in the strength of the nonaxisymmetric bar potential (Binney and Tremaine, 2008), stars in resonant orbits between the Inner Lindblad resonance (ILR) and the CR are oriented along the bar, stars between the CR and the OLR orbit with trajectories perpendicular to the bar, and beyond the OLR the stellar orbits tend to be elongated along the bar's orientation (Contopoulos and Papayannopoulos, 1980). These features are expected to persist even as the bar potential grows strong, though the fractional number of stars following the particular orbits predicted by leading-order perturbation theory may grow small (Binney and Tremaine, 2008). Nevertheless, by using the change in sign of the axial asymmetry in star counts (Gardner, Hinkel, and Yanny, 2020; Hinkel, Gardner, and Yanny, 2020b) to determine the location of the OLR and using leading order perturbation theory to determine the pattern speed as well as the CR, we find that our determined CR is crudely commensurate with the length of the Galactic bar — this is expected if the Galaxy's bar is indeed weak (Aguerri, Beckman, and Prieto, 1998).

In this letter, we employ a novel, model-independent method for determining the bar's pattern speed and resonant effects by leveraging our ability to detect axially asymmetric orbits. From tests of axisymmetry of our galaxy (Gardner, Hinkel, and Yanny, 2020), Hinkel, Gardner, and Yanny (2020b) determine the radius of the OLR using *Gaia* DR2 data (Prusti et al., 2016; Brown et al., 2018; Lindegren et al., 2018), and here we use this measurement along with leading order perturbation theory

Binney and Tremaine (2008) and the rotation curve of Eilers et al. (2019) in order to obtain a measurement of the pattern speed. With this we can also determine the radius of the CR.[1] We also document an abrupt change in the vertical structure of the galaxy very near to the OLR; we believe this speaks to north-south differences in the Galactic bar or perhaps some interaction between the OLR and separate north-south differences in the plane (Widrow et al., 2012; Yanny and Gardner, 2013; Ferguson, Gardner, and Yanny, 2017; Bennett and Bovy, 2018). We note, for reference, that a significant north-south asymmetry has been recently suggested in the galactic center excess (Leane and Slatyer, 2020). Finally, we compare our results with those already in the literature, as well as with other established features of the bar, noting the additional possibility of non-steady-state and/or axial-symmetry-breaking effects in the bar region.

7.2 Theory

As motivated through the perturbation theory analysis of Binney and Tremaine (2008) and depicted graphically in Dehnen (2000), the Galactic bar drives the OLR, holding sway over the shape of stellar orbits despite the affected stars not being within the physical extent of the bar, at Galactocentric, in-plane $R < \ell_{\rm bar}$, where $\ell_{\rm bar}$ is the bar half-length. Due to the periodic nature of the bar's gravitational force on stars at $R > \ell_{\rm bar}$, stars may receive a pull from the bar at the same phase in their orbit, exciting the orbit into an elliptical shape. For stars just inside (outside) the radius of the OLR, orbits are elongated perpendicular (parallel) to the bar (Dehnen, 2000; Contopoulos and Papayannopoulos, 1980), which has been thought to point at $\sim 10^\circ - 70^\circ$ (Dehnen, 2000) away from the Sun-Galactic center line ($\phi = 180^\circ$), with more recent work (Robin et al., 2012; Portail, 2016; Anders et al., 2019) finding values within $13^\circ - \sim 40^\circ$.

Given that this effect has ϕ-dependence, it breaks axial symmetry and thus can result in a measurably non-zero value of the axial asymmetry, $\mathcal{A}$, about the anti-center line as defined in Gardner, Hinkel, and Yanny (2020). Indeed, one would expect that the stars "promoted" to higher R by the bar near the OLR would cause a very slight over-density over a small range in azimuth near the bar's principal axis at some value $R_{\rm OLR} + \Delta R$ and leave behind a commensurate, slight under-density at some $R_{\rm OLR} - \Delta R$. By scanning over various values of R we have found that $\mathcal{A}$ varies radially (Hinkel, Gardner, and Yanny, 2020b).

The orbital alignments due to the central bar in the OLR region break axial asymmetry in the manner illustrated schematically in Fig. 7.1. Just outside the resonant radius, we expect to find more stars to the right of the $\phi = 180^\circ$ line ($\phi < 180^\circ$), and expect to find more stars on the left ($\phi > 180^\circ$) when just inside the resonant radius. Thus, as one moves outward in R the expected axial asymmetry

[1] Our analysis uses the rotation curve of Eilers et al. (2019), which assumes $R_0 = 8.122(31)$ kpc (Abuter et al., 2018), whereas we employ a subsequent (and more precise) determination of the Sun–Galactic-center distance, $R_0 = 8.178(26)$ kpc (Abuter et al., 2019) as appropriate.

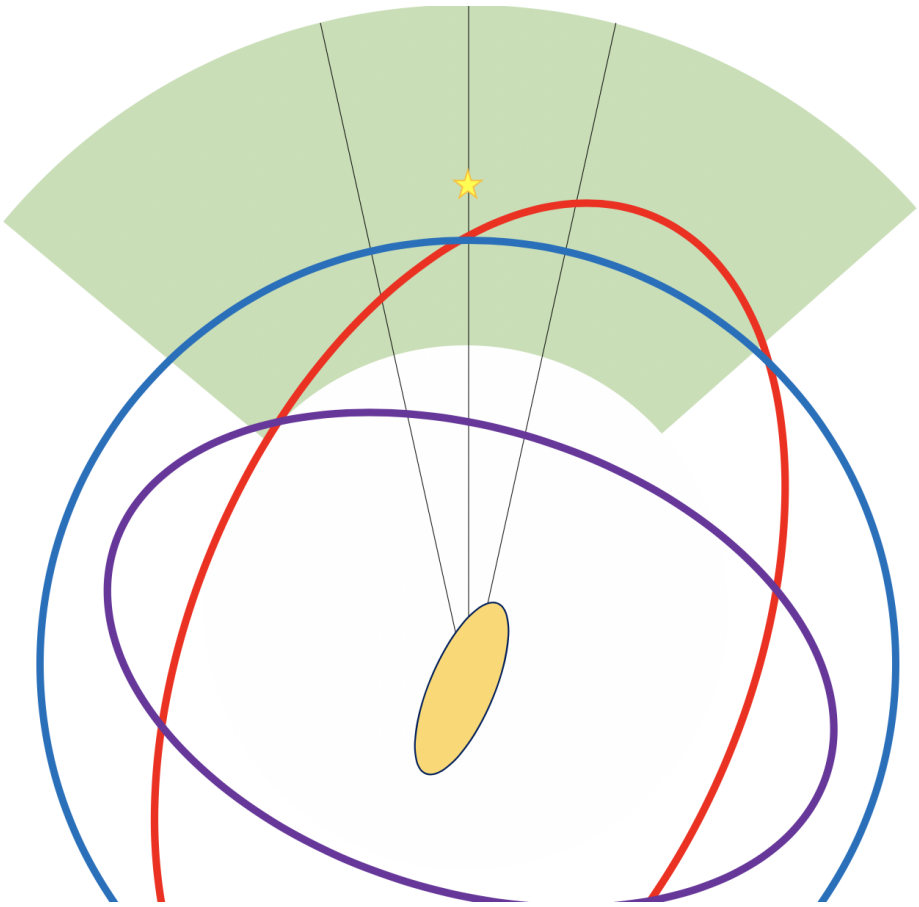

Figure 7.1: A schematic depiction of the orbital alignments due to the bar in the OLR region. The blue circle is the orbital radius of the OLR, the purple ellipse is an orbit interior to the OLR, and the red ellipse is an orbit exterior to the OLR. The green annular wedge region is our sample's in-plane footprint, with a star signifying the sun's position, and the yellow ellipse is the Galactic bar. Stellar orbits tend to align parallel (perpendicular) to the bar when the orbit is just outside (inside) the Outer Lindblad resonant radius. The geometry has been greatly exaggerated and we have shown closed orbits only, in order to illustrate the small effect we have found

.

would go from left-heavy to right-heavy, corresponding to a sign flip:

$$\mathcal{A}(R < R_{\rm OLR}) > 0 \;\longrightarrow\; \mathcal{A}(R > R_{\rm OLR}) < 0. \tag{7.1}$$

As such, the value of R that yields zero asymmetry is the location of the sign-flip and thus the location of the OLR. In contrast, if the axially asymmetric effect were, rather, a CR, then the sense of the sign flip would change from $\mathcal{A} < 0 \longrightarrow \mathcal{A} > 0$ as R increases.

Following the methods of Binney and Tremaine (2008), a non-axisymmetric contribution to the Galactic gravitational potential can be treated as a weak perturbation. Working in a reference frame rotating with the bar, at a steady pattern speed $\Omega_{\rm p}$, we have the Lagrangian

$$L = \frac{1}{2}\dot{R}^2 + \frac{1}{2}[R(\dot{\varphi} + \Omega_{\rm p})]^2 - \Phi(R, \varphi)\,, \tag{7.2}$$

where we employ cylindrical coordinates with $\varphi = 0$ aligned along its long axis. The potential can be broken into an unperturbed, axisymmetric potential and a non-axisymmetric correction:

$$\Phi(R, \varphi) = \Phi_{\rm u}(R) + \Phi_1(R, \varphi)\,. \tag{7.3}$$

In the absence of the perturbation, we find a circular orbit at R with $\dot{\varphi} = \Omega - \Omega_{\rm p}$, where the frequency

$$\Omega = \pm\sqrt{\frac{1}{R}\frac{d\Phi_u}{dR}}\,, \tag{7.4}$$

where $\Omega > 0$ corresponds to prograde rotation. Specifying the form of the perturbing potential as per (Binney and Tremaine, 2008) we have

$$\Phi_1(R, \varphi) = \Phi_{\rm bar}(R)\cos(m\varphi)\,, \tag{7.5}$$

where $m = 2$ for a Lindblad resonance. Now with $R(t) = R_{\rm u} + R_1(t)$ and $\varphi(t) = \varphi_{\rm u}(t) + \varphi_1(t)$, analyzing the equations of motion while working to leading order in $|\Phi_1/\Phi_{\rm u}| \ll 1$ and assuming $\varphi_1 \ll \varphi_{\rm u}$ yields

$$\ddot{R}_1 + \kappa_0^2 R_1 = -\left[\frac{d\Phi_{\rm bar}}{dR} + \frac{2\Omega\Phi_{\rm bar}}{R(\Omega - \Omega_{\rm p})}\right]_{R=R_{\rm u}} \cos(m(\Omega(R_{\rm u}) - \Omega_{\rm p})t)\,. \tag{7.6}$$

where κ_0 is the natural harmonic frequency for the oscillatory perturbation provided by the bar,

$$\kappa_0^2 = \left(\frac{d^2\Phi_{\rm u}}{dR^2} + 3\Omega^2\right)_{R=R_{\rm u}} = \left(R\frac{d\Omega^2}{dR} + 4\Omega^2\right)_{R=R_{\rm u}}\,, \tag{7.7}$$

and the general solution

$$R_1(t) = A\cos(\kappa_0 t + \alpha) - \left[\frac{d\Phi_{\rm bar}}{dR} + \frac{2\Omega\Phi_{\rm bar}}{R(\Omega - \Omega_{\rm p})}\right]_{R=R_{\rm u}} \left(\frac{\cos(m(\Omega - \Omega_{\rm p})t)}{\kappa_0^2 - m^2(\Omega - \Omega_{\rm p})^2}\right)\,, \tag{7.8}$$

so that open orbits appear with nonzero, arbitrary A for any α. Regardless, a resonance appears if $\kappa_0^2 - m^2(\Omega - \Omega_\mathrm{p})^2 = 0$, and it is an $m = 2$ OLR if

$$\Omega_\mathrm{p} - \Omega = \kappa_0/2\,. \tag{7.9}$$

Notice this condition can be combined with Eq. 7.7 to yield:

$$4(\Omega_\mathrm{p} - \Omega)^2\Big|_{R=R_\mathrm{OLR}} = \left(R\frac{d\Omega^2}{dR} + 4\Omega^2\right)_{R=R_\mathrm{OLR}}\,, \tag{7.10}$$

to give the pattern speed from R_OLR and the R-dependence of Ω:

$$\Omega_\mathrm{p} = \Omega(R_\mathrm{OLR}) + \frac{1}{2}\sqrt{4\Omega^2(R_\mathrm{OLR}) + R_\mathrm{OLR}\frac{d\Omega^2}{dR}\Big|_{R=R_\mathrm{OLR}}}\,. \tag{7.11}$$

Finally, the pattern speed determines the CR radius:

$$\Omega_\mathrm{p} = \Omega(R_\mathrm{CR})\,, \tag{7.12}$$

noting that we cannot also determine the location of the Inner Lindblad resonance (ILR) with these methods for want of information on Ω with R in the very inner portion of our galaxy.

To determine the numerical value of the pattern speed and more, we use an observational assessment of the Galactic rotation curve, which yields both Ω^2 and $d\Omega^2/dR$ with R. That is, the Galactic rotation curve is the circular speed v_c with R, where

$$\Omega \equiv \frac{v_\mathrm{c}(R)}{R} = \sqrt{\frac{1}{R}\frac{d\Phi_\mathrm{u}}{dR}}\,. \tag{7.13}$$

For this, we use the recent, high precision determination of Eilers et al. (2019), which uses an analysis of red-giant branch stars from *Gaia* DR2, cross-matched with APOGEE data, for refined distance assessments (Hogg, Eilers, and Rix, 2019). The analysis itself uses a Jeans equation framework in which the underlying Galactic distribution function $f(\mathbf{x}, \mathbf{v}, t)$ is assumed to be axially symmetric and in steady state. This yields

$$v_\mathrm{c}^2 = \langle v_\phi\rangle^2 - \langle v_R\rangle^2\left(1 + \frac{\partial \ln\langle \mathrm{v}_\mathrm{R}^2\rangle}{\partial \ln R} + \frac{\partial \ln\nu}{\partial \ln R}\right) + \delta \tag{7.14}$$

where $\nu(\mathbf{x}, t) = \int d^3\mathbf{v} f(\mathbf{x}, \mathbf{v}, t)$ and $\delta = 0$. We can, however, determine the modification of v_c^2 were all the neglected terms included. This gives

$$\delta = -R\frac{\partial}{\partial t}\left(\langle v_R\rangle \ln\nu\right) - \frac{\partial}{\partial \phi}\left(\langle v_R v_\phi\rangle \ln\nu\right) - R\frac{\partial}{\partial z}\left(\langle v_R v_z\rangle \ln\nu\right)\,, \tag{7.15}$$

where the additions reflect corrections for non-steady-state, axial-symmetry-breaking, and z-dependent effects, respectively. The z-dependent term also appears in Eilers et al. (2019) and is estimated to affect v_c at the $\sim$1% level at $R \sim 18\,\mathrm{kpc}$. The axial symmetry breaking term vanishes if $\nu(\mathbf{x})$ itself is axially symmetric. We will note a

possible role for these small terms, likely characterized in size by the non-steady-state term, later. Eilers et al. (2019) determines $v_c(R)$ over $5 \lesssim R \lesssim 25$ kpc, for which they report the linear parametrization

$$v_c(R) = (229.0 \pm 0.2)\mathrm{km\,s^{-1}} - (1.7 \pm 0.1)\mathrm{km\,s^{-1}\,kpc^{-1}} \cdot (\mathrm{R} - \mathrm{R}_0)\,, \tag{7.16}$$

where here $R_0 = 8.122(31)$ kpc (Abuter et al., 2018) has been employed. We employ this parametrization in what follows.

7.3 Analysis

As we showed in Gardner, Hinkel, and Yanny (2020), effects from the LMC and Galactic Bar are the two dominant contributors of axial symmetry breaking in the solar neighborhood. Further, in Hinkel, Gardner, and Yanny (2020b), we found a sign flip in the sense of the asymmetry that matches that expected from an OLR assuming the determined bar orientation (Robin et al., 2012; Portail, 2016; Anders et al., 2019) does indeed point in the third quadrant of the galactocentric rectangular coordinate system in which the positive x-axis points from the GC in the direction opposite the sun with y and z following from a right-hand coordinate system choice in which z increases from zero at the mid-plane to larger values toward the North Galactic Pole. Here, we refine the sign flip analysis in order to remove any background effects from the overall distortion of the galaxy due to the LMC's influence, which we found to be described by a prolate shape pointing towards the LMC (Gardner, Hinkel, and Yanny, 2020; Erkal et al., 2019). We expect this global background effect to be a constant offset over the volume of space we study, and we define this background asymmetry as $< \mathcal{A} >_\mathrm{B}$. As such, the precise value of R where the equality

$$< \mathcal{A}(R) > - < \mathcal{A} >_\mathrm{B} = 0 \tag{7.17}$$

corresponds to the radius of the OLR. We estimate the background asymmetry by integrating over the entire volume of the sample of Gardner, Hinkel, and Yanny (2020) and find that $< \mathcal{A} >_\mathrm{B} = -0.0032 \pm 0.0003$. This moves our measurement of the sign flip from Hinkel, Gardner, and Yanny (2020b), and thus R_OLR, slightly outward in R, as expected.

In practice, we repeat the radial scans of Hinkel, Gardner, and Yanny (2020b) and subtract the offset in order to find the bin with zero asymmetry. The results of this analysis are tabulated in Table 7.1. The resulting shift in the determined OLR location appears in Table 7.3. The OLR radius is defined as the center of the bin in Table 7.1 which, after accounting for the background asymmetry, yields an asymmetry that is within 1-σ from 0. Note that, after rounding, this yields $R_\mathrm{OLR} = (0.96 \pm 0.03)R_0 = 7.85 \pm 0.25$ kpc where the uncertainty in the OLR radius assessment is the first ΔR in the successively smaller ΔR scans in which a "zero" is no longer discernible in a single bin, rounded to one significant figure. The measured axial asymmetry just within and beyond the determined OLR location in R is shown in Fig. 7.2. We discuss its interesting north/south differences in the next section. Here we wish to focus on the size of the asymmetry $< \mathcal{A}(R) > - < \mathcal{A} >_\mathrm{B}$ itself

because this is reflective of the number of stars that populate the distorted orbits we have analyzed. As tabulated in Table 7.2, the flip in sign of the asymmetry is quite symmetric about the Outer Lindblad resonant radius, which is expected if the stars are excited to higher R and leave behind a dearth of stars at lower R. Additionally, Table 7.2 suggests that $\mathcal{O}(10^4)$ stars populate the distorted orbits that we analyze, corresponding to a small but statistically significant change in the sign of the asymmetry.

Table 7.1: Axial asymmetries, N+S, averaged over azimuthal angles about the anti-center direction up to $|180° - \phi| = 6°$, computed for a wedge of size ΔR for different choices of starting radius R_i, with $R_f = R_i + \Delta R$, to reveal the sign change in the average asymmetry as $R_i - R_f$ changes. We refine the location of the sign flip iteratively by computing the average asymmetry with R_i for smaller ΔR. Note that the distances are in units of R_0 and that the "Sign" is assessed by whether the magnitude of the asymmetry difference is in excess of its error. The uncertainty in the final asymmetry $\sigma_{\langle\mathcal{A}\rangle}$ has been computed by adding the systematic axial asymmetry of Hinkel, Gardner, and Yanny (2020b) and statistical errors in quadrature and then adding the uncertainty from the background subtraction.

$R_i - R_f$ (R_0)	ΔR (R_0)	$\langle\mathcal{A}(\phi)\rangle$ - $\langle\mathcal{A}\rangle_{\rm B}$	$\sigma_{\langle\mathcal{A}\rangle}$	Sign
0.8750 - 0.9375	0.0625	+0.0103	0.0015	+
0.9000 - 0.9625	0.0625	+0.0067	0.0014	+
0.9250 - 0.9875	0.0625	+0.0005	0.0014	0
0.9250 - 0.9625	0.0375	+0.0049	0.0015	+
0.9375 - 0.9750	0.0375	+0.0009	0.0015	0
0.9500 - 0.9875	0.0375	-0.0031	0.0014	-
0.9375 - 0.9625	0.0250	+0.0037	0.0016	+
0.9438 - 0.9688	0.0250	+0.0013	0.0015	0
0.9500 - 0.9750	0.0250	-0.0015	0.0015	0

7.4 Results

In this analysis, we have chosen the rotation curve of Eilers et al. (2019) as it represents the only highly precise assessment of the Galaxy's rotation curve in the region of $5 \lesssim R \lesssim 25$ kpc. As a check, we compute the Oort Constants, A and B, using the $v_{\rm c}(R)$ parametrization in Eq. 7.16 as given in Eilers et al. (2019) and find that $A = 14.95 \pm 0.43$ km s^{-1} kpc^{-1} and $B = -13.25 \pm 0.43$ km s^{-1} kpc^{-1}, where we have combined the statistical and $\pm 3\%$ systematic error in quadrature. These numbers are in very good agreement with the recent findings of Li, Zhao, and Yang (2019) using *Gaia* DR2 data within 500 pc of the Sun: $A = 15.1 \pm 0.1$ km s^{-1} kpc^{-1}

Table 7.2: Star counts and background-corrected axial asymmetries for bins of varying width, ΔR, probing just interior and exterior to the Outer Lindblad resonant radius, where the errors in the last digits are indicated in parentheses. The region designated 'inside' corresponds to $R \in [R_{\rm OLR} - \Delta R, R_{\rm OLR}]$ while 'outside' corresponds to $R \in [R_{\rm OLR}, R_{\rm OLR} + \Delta R]$. As we focus in on the OLR, the magnitude of the asymmetry becomes slightly smaller, perhaps suggesting the magnitude of the first order radial correction, $|R_1|$, (see Eq. 7.8) can be larger than a couple hundred parsecs. Also note that the radial bin external to the OLR has more stars due to the geometry of our stellar sample (Gardner, Hinkel, and Yanny, 2020; Hinkel, Gardner, and Yanny, 2020b).

$\Delta R\,(R_0)$	N(inside)	N(outside)	$\mathcal{A}(R < R_{\rm OLR})$	$\mathcal{A}(R > R_{\rm OLR})$
0.0625	3,070,836	4,241,269	+0.0075(14)	-0.0076(14)
0.0500	2,615,604	3,383,670	+0.0068(14)	-0.0065(14)
0.0375	2,087,432	2,524,189	+0.0058(15)	-0.0050(14)
0.0250	1,478,859	1,738,446	+0.0050(16)	-0.0047(15)

and $B = -13.4 \pm 0.1$ km s^{-1} kpc^{-1}, though there is some tension in the determination of B with respect to the earlier results of Binney and Tremaine (2008) ($B = -12.4 \pm 0.6$ km s^{-1} kpc^{-1}) and Bovy (2017) ($B = -11.9 \pm 0.4$ km s^{-1} kpc^{-1}).

This rotation curve, along with a precise measurement of the Sun-GC distance (Abuter et al., 2019) affords us the opportunity to use our OLR location determination to determine $\Omega_{\rm p}$ and also the location of the CR. Employing Eq. 7.11, we have $\Omega_{\rm p} = 49.3 \pm 2.2$ km s^{-1} kpc^{-1}. By using our determined value of $R_{\rm OLR}$ and the leading order perturbation theory as per Binney and Tremaine (2008), our pattern speed determination does not depend on any assumptions about the bar potential, other than its interpretation as a $m = 2$ resonance. Moreover, the pattern speed we find falls within the literature average given by Bland-Hawthorn and Gerhard (2016), though it tends to be on the higher end as shown amongst a sample of other findings in Table 7.3. We recall, though, that as in the case of Sanders, Smith, and Evans (2019), the pattern speed estimates can be biased low when including observations beyond the GC.

Using this determined pattern speed in Eq. 7.12, we estimate $R_{\rm CR} = (0.58 \pm 0.04)R_0 = 4.76 \pm 0.27$ kpc. Interestingly we determine that $R_{\rm OLR}/R_{\rm CR} \approx 1.7$ in agreement with the expectation of Dehnen (2000) if the bar is weak and the rotation curve is flat. This is a useful consistency check as our CR determination is just compatible (within 1-σ) with the lower R limit of the Eilers et al. (2019) range of validity. Additionally, this Corotation estimate is also just compatible within errors with the half-length of the bar, for which Wegg, Gerhard, and Portail (2015) find $\ell_{\rm bar} = 5.0 \pm 0.2$ kpc. We note that a weak bar should possess a CR at radii beyond the half-length of the bar (Aguerri, Beckman, and Prieto, 1998). If the parameter δ is positive, reflective of a driving effect from a slowing of the bar (Weinberg, 1993; Chiba, Friske, and Schönrich, 2021), then we can bring the picture into better agreement. The fluctuation of the bar's parameters suggested by Hilmi et al. (2020) could explain

Table 7.3: The literature offers a wide array of pattern speed assessments. The various assessments use differing assessments in the Sun-GC distance and the local rotation curve, which could result in small changes. Also, our CR and OLR estimates for each work use the rotation curve of Eilers et al. (2019) and the Sun-GC distance of Abuter et al. (2019).

Source	Ω_p (km s^{-1} kpc^{-1})	Estimate of R_{CR} (kpc)	Estimate of R_{OLR} (kpc)
Dehnen (1999)	53 ± 3	4.44	7.34
Sanders, Smith, and Evans (2019)	41 ± 3	5.69	9.32
Sanders, Smith, and Evans (2019) [a]	31 ± 1	7.43	12.01
Hunt and Bovy (2018) ($m = 4$)	$\lesssim 1.35\ \Omega_0$ [b]	> 6.15	> 10.04
Portail et al. (2015)	$25 - 30$	$7.66 - 9.10$	$12.37 - 14.54$
Portail et al. (2016)	39.0 ± 3.5	5.97	9.75
Monari et al. (2017)	$> 1.8\ \Omega_0$	< 4.66	< 7.69
Chakrabarty (2007)	$57.4^{+2.8}_{-3.3}$	4.11	6.81
This work (without LMC correction)	49.9 ± 2.2	4.71 ± 0.26	7.77 ± 0.25
This work (with LMC correction)	49.3 ± 2.2	4.76 ± 0.27	7.85 ± 0.25
Bland-Hawthorn and Gerhard (2016) [c]	43 ± 9	5.43	8.91

[a] Includes data from far side of the bar.
[b] $\Omega_0 \approx 28$ km s^{-1} kpc^{-1} is the rotational frequency at the solar circle.
[c] Approximate literature range adopted in a review of galactic properties.

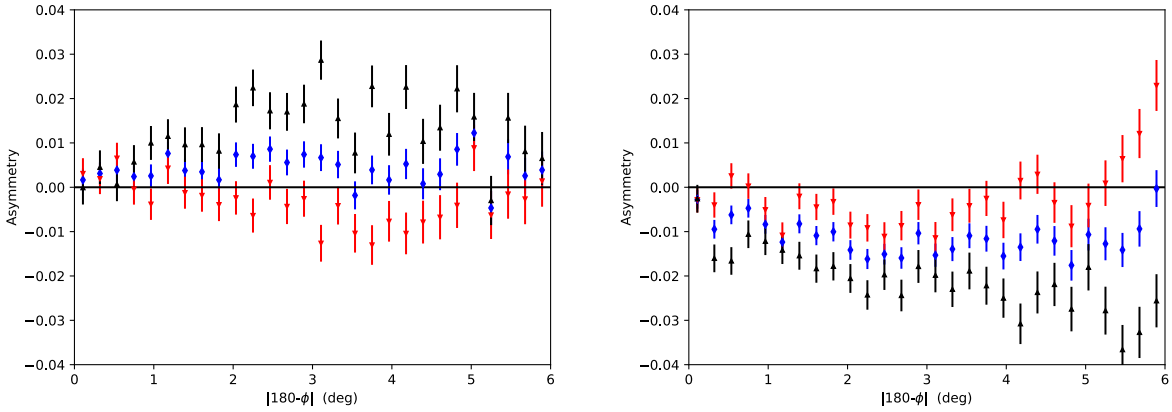

(a) a (b) b

Figure 7.2: (a) The axial asymmetry for $R \in [0.8975, 0.9600]R_0$. (b) The axial asymmetry for $R \in [0.9600, 1.0225]R_0$. The blue diamonds are the aggregate axial asymmetry and the black and red triangles are for the northern ($z > 0$) and southern ($z < 0$) halves respectively. The sign flip in the aggregate asymmetry is clearly visible here, which we attribute to the bar's OLR. In addition, the vertical structure changes just beyond the OLR, with a north-left correlation for $R < R_{\rm OLR}$ and a north-right correlation for $R > R_{\rm OLR}$.

the non-steady state effects we infer.

Given the diverse array of pattern speeds in the literature, as compiled in Table 7.3, it should perhaps come as no surprise that both the CR and the OLR have been argued to be near the solar circle. As such, the wide spread in pattern speed assessments inevitably means that there are correspondingly large ranges for $R_{\rm CR}$ and $R_{\rm OLR}$. Interestingly, though, a recent measurement of $R_{\rm OLR}$ by Khoperskov et al. (2019a) estimates the location of the OLR without assuming a pattern speed. They find that the OLR is near $R = 9$ kpc, though they rely on models that draw random distributions of Gaia data that are very close to the mid-plane, for which the effects of reddening and extinction from dust would seem to be important. As an additional effect, the Milky Way's spiral arms break axial symmetry, but we have taken care to ensure that our sample is sufficiently out of plane so as to minimize any confounding effects due to spiral structure (Gardner, Hinkel, and Yanny, 2020).

Finally, in addition to the pattern speed and the locations of the OLR and CR, we have found an unexpected, abrupt change in vertical structure near the OLR. By computing the axial asymmetry for $z > 0$ and $z < 0$, henceforth the north (N) and south (S) respectively, we find as R increases through the OLR, the asymmetry in the N goes from left-heavy to right-heavy, with a smaller effect of opposite sense in the S, as illustrated in Fig. 7.2. Speculatively, this could be due to a vertical resonance with the bar, a bar tilted slightly out of plane, or perhaps stem from a North/South asymmetry in the bar itself, where we note that a North/South effect has been found in the Galactic center excess (Leane and Slatyer, 2020). Alternatively, local N/S

differences have been noted in the solar neighborhood and have been attributed to the Sagittarius impact (Widrow et al., 2012; Yanny and Gardner, 2013; Ferguson, Gardner, and Yanny, 2017), so that the vertical effects seen near the OLR may come from a completely separate event. Indeed, Carrillo et al. (2019) have suggested that the Sagittarius impact could have significantly perturbed the Galactic bar, or could have even been responsible for its genesis. Detailed studies of the Galactic bar resonances in the presence of small vertical asymmetries in the bar or in the local disk, or subject to significant vertical perturbations could conceivably help explain this behavior.

We note that our assumption of an $m = 2$ OLR resonance can be tested through additional observational studies. An $m = 2$ OLR resonance implies axially asymmetric structures at $\phi = 0, 180°$, but the possibility of a $m = 4$ (Hunt and Bovy, 2018) OLR implies asymmetric structures at $\phi = 90, 270°$ also, so that over the longer term there is another observational test (Hunt and Bovy, 2018). Yet this is not the only possibility. Note that the existence of an $m = 4$ resonance would imply that an $m = 2$ resonance could appear (if it exists) at larger R as well, so that if our sign flip were interpreted as an $m = 4$ resonance, we would find $\Omega_{\rm p} \approx 39.3\,{\rm km\,s^{-1}\,kpc^{-1}}$ and a $m = 2$ resonance at $R_{\rm OLR} \approx 11.6$ kpc. This alternative possibility meshes well with the findings of Portail et al. (2016) and could be explored in future data releases.

7.5 Summary

We have shown that axial symmetry breaking orbital alignments are detectable at very small levels and that our analysis of this effect is consistent with leading order perturbation theory that models the Galactic bar as a weakly non-axially symmetric effect. Through this approach, we avoid the need to assume a form for the galaxy's potential, apart from the assumption of a $m = 2$ potential, and we only rely on the quadrant in which the bar points in order to interpret the sign flip we observe in the asymmetry. We have found that the OLR is situated at $R_{\rm OLR} = 7.85 \pm 0.25$ kpc, which implies the pattern speed of the bar is $\Omega_{\rm p} = 49.3 \pm 2.2$ km s^{-1} kpc^{-1}, and thus the radius of Corotation is $R_{\rm CR} = 4.76 \pm 0.27$ kpc. Additionally, we find evidence for a change in the vertical structure of the disk near the OLR, but we cannot resolve if this effect is due to a possibly tilted or asymmetric bar, or if the effect is local in nature, possibly due to the Sagittarius impact. Our approach is entirely novel, but our estimates for the pattern speed of the bar are very much consistent with the upward revision of the $\Omega_{\rm p}$ of Sanders, Smith, and Evans (2019) and Bovy et al. (2019) as suggested by the work of Hilmi et al. (2020), and our inferred resonance locations for the CR and the OLR are in remarkable agreement with the picture of Dehnen (1999), even if our assessments are much more precise. Thus we believe that our results are in support of a Galactic bar that is both weak and fast.

Chapter 8 Two-Point Correlation Function Studies for the Milky Way: Discovery of Spatial Clustering from Disk Excitations and Substructure

8.1 Introduction

Astronomy has long focused on the study of single, exceptional objects; with the advent of *Gaia* we can now focus on the broader picture. Indeed, the discovery of diffuse structure via a Two-Point Correlation Function study is now feasible with the number of stars with superb parallax measurements near the Sun numbering in the tens of millions. With data from the Gaia mission, we now have an unprecedented view of the patterns and structures in our Milky Way. In this thesis, we study these patterns and structures for new clues to the turbulent collision history of our Galaxy.

Currently, the Galaxy has largely cannibalized the Sagittarius Dwarf Spheroidal, which is estimated to have plunged through the Galactic disk in a near-perpendicular manner close to the anti-center ray within the last 1 Gyr or so (Purcell et al., 2011). Indeed, some simulations suggest that this impact may be behind the spiral arms (Purcell et al., 2011) and the vertical waves seen in the vertical distribution of stars (Gómez et al., 2012b), as discovered by Widrow et al. (2012) and later expanded upon by Yanny and Gardner (2013), Ferguson, Gardner, and Yanny (2017), and Bennett and Bovy (2018). Moreover, Ferguson, Gardner, and Yanny (2017) found that the particular wave-like perturbation observed changed when looking in various regions of the Galaxy, hinting at a complex vertical landscape filled with potential structural variations.

In addition to this picture of planar vertical waves in the Milky Way, Antoja et al. (2018) have shown that a "phase-space spiral" pattern in $z - v_z$ phase-space is evocative of phase-mixing effects, where perhaps the effect has not yet wound up tightly enough to be inconspicuous, indicating that it may be a fairly recent development in the Galaxy's history (Antoja et al., 2018). Moreover, Antoja et al. (2018) interpret this snail-shaped pattern in terms of an ad-hoc, anharmonic oscillator model in order to derive an approximate date for the perturbation which is thought to have caused it. They find a time-scale of approximately 300-900 Myr, which appears to be consistent with the Sagittarius Dwarf's last passage through the disk (Purcell et al., 2011).

Moreover, corrugations exist in the disk (Xu et al., 2015; Bland-Hawthorn and Tepper-Garcıa, 2021), which may be due to the impact of the Sagittarius Dwarf along with a modulating influence from the Large Magellanic Cloud (Laporte et al., 2018b), while the latter may also be warping the disk (Weinberg and Blitz, 2006; Gardner, Hinkel, and Yanny, 2020). Indeed, corrugations of a similar nature are observed in Milky-Way-like galaxies (Gómez et al., 2021), and those in the Milky Way may be a super-position of different wave-like effects (Bland-Hawthorn and Tepper-

This chapter is a partial draft in preparation for publication in collaboration with Susan Gardner and Brian Yanny.

García, 2021). Regardless, of the precise origins of the corrugations, it is becoming increasingly clear that ours is an excited disk; the Milky Way disk abounds with vertical structure.

While examining the one-body distribution of stars in the Galaxy has proven a useful tool for probing the above structures in the past, one can also examine the *two*-body density. More accurately, the Two-Point Correlation Function (2PCF) can be applied to Milky Way data in order to uncover structure. Despite a number of uses in nuclear and condensed matter physics, the 2PCF has essentially been confined to the extra-Galactic side of astrophysics. While Kamdar et al. (2020) and Lancaster, Belokurov, and Evans (2019) both employ the 2PCF on Milky Way scales, both rely on the scalar distances between stars and do not explore the vector nature of the arguments of the 2PCF.

In other words, one can examine the separations of stars in only one component of that separation, with each component providing additional insights into the structure of the Galaxy. As motivated in Chapter 3, this 2PCF analysis can help search for structure within the halo, potentially differentiating between various theories of dark matter based on the presence or lack of structure at small scales (Bose et al., 2016; Nadler et al., 2021; Gardner, McDermott, and Yanny, 2021). As these scales are too small for cosmological simulations to probe to, they offer an excellent complement to other studies, and benefit immensely from the high-quality, abundant data in the Gaia database.

With the Gaia data in hand, we have more than enough stars to effect a 2PCF analysis. There is, however, a fair degree of biases and regions of incompleteness in the Gaia data, which must first be accounted for. To this end, we choose the ultra-pure data set of Gardner, Hinkel, and Yanny (2020) and Hinkel, Gardner, and Yanny (2020b) in order to sample a complete, nearby, low-parallax-error data set well above the spiral arms so that we can be reasonably sure that any discovered structure is indeed real and not readily explainable via one-body analyses.

Furthermore, the data set employed here reaches up to $|z| = 3$ kpc from the Galactic mid-plane, allowing for the examination of structural differences in the Galaxy with z. This is of particular interest in the search for Dark Matter substructure, as the halo (presumably home to the bulk of this dark substructure) becomes a more dominant component of the distribution function at high $|z|$ and the disk's contribution to the total density falls off. Ultimately, though, discovery of substructure *or* lack of substructure in the halo would be interesting, given the constraints that either could have on various models of Dark Matter (Buckley and Peter, 2018). Namely, discovery of spatial clustering around dark matter structure is important in and of itself, while a lack of structure could indicate a Warm Dark Matter paradigm.

8.2 Theory

An isolated galaxy in steady-state is described by a distribution function in its stars in six-dimensional phase space: $f(\mathbf{x}, \mathbf{v}, t)$. This distribution function is determined by the simultaneous solution of the collisionless Boltzmann, or Vlasov, and Poisson

equations, where we emphasize that the Vlasov equation itself emerges only if correlations between the stars are neglected (Binney and Tremaine, 2008). Such a galaxy with a stellar disk is expected to be axially symmetric with respect to rotations about an axis through its center of mass, perpendicular to the plane of the disk, and thus is also reflection symmetric about the galactic mid-plane (An, Evans, and Sanders, 2017; Schutz et al., 2018).

We have determined that in our own Galaxy, however, that even if axial symmetry is very nearly conserved, reflection symmetry can be markedly broken (Gardner, Hinkel, and Yanny, 2020; Hinkel, Gardner, and Yanny, 2020b), implying that the Galaxy is not isolated and/or not in steady state. We interpret the small axial symmetry breaking we have found in our carefully selected sample of Gaia DR2 stars as arising, in part, from the torque exerted on our sample by the massive LMC/SMC system, yet the differences in axial symmetry breaking we find, north versus south, are larger still. Thus we think our results are particularly indicative of the presence of non-steady-state effects (Gardner, Hinkel, and Yanny, 2020; Hinkel, Gardner, and Yanny, 2020b). This and the appearance of striking wave-like features in stellar number counts north and south of the Galactic plane (Widrow et al., 2012; Yanny and Gardner, 2013; Bennett and Bovy, 2018) suggest that the stars are likely correlated as well, possibly on many different length scales (Kamdar et al., 2020).

To explore this concretely, we revisit the derivation of the Vlasov equation itself: we return to the Bogoliubov, Born, Green, Kirkwood, and Yvon (BBGKY) hierarchy which comes from the analysis of Liouville's equation in the presence of pairwise forces, relating the time-evolution of the s-particle distribution function f_s, such that $f_1 \equiv f$, to the $(s+1)$-particle distribution function f_{s+1} (Gardner, McDermott, and Yanny, 2021). Consequently, the s-particle distribution function is not simply proportional to $(f)^s$; rather, we introduce (Thorne and Blandford, 2017)

$$f_2(\mathbf{v}_1,\, \mathbf{x}_1,\, \mathbf{v}_2,\, \mathbf{x}_2,\, t) = f(\mathbf{v}_1,\, \mathbf{x}_1,\, t) f(\mathbf{v}_2,\, \mathbf{x}_2,\, t)(1 + \xi_{12})\,, \tag{8.1}$$

where ξ_{12} is the 2PCF, with the same arguments as that of the two-particle distribution function. In general, the 2PCF can either enhance or suppress the joint probability of finding a particle in a phase-space volume $d^3\mathbf{x}_1 d^3\mathbf{v}_1$ and another in $d^3\mathbf{x}_2 d^3\mathbf{v}_2$: the probability of finding one is no longer independent of the probability of finding the other. The BBGKY hierarchy links f_2 to f_3, where

$$f_3(\mathbf{v}_1,\, \mathbf{x}_1,\, \mathbf{v}_2,\, \mathbf{x}_2,\, \mathbf{v}_3,\, \mathbf{x}_3,\, t) = f(\mathbf{v}_1,\, \mathbf{x}_1,\, t) f(\mathbf{v}_2,\, \mathbf{x}_2,\, t) f(\mathbf{v}_3,\, \mathbf{x}_3,\, t) \Xi, \tag{8.2}$$

and

$$\Xi = (1 + \xi_{12} + \xi_{13} + \xi_{23} + \xi_{123})\,, \tag{8.3}$$

with $\xi_{ij} \equiv \xi_{ij}(\mathbf{x}_i, \mathbf{v}_i, \mathbf{x}_j, \mathbf{v}_j, t)$. If one neglects the possibility of the *three-particle* correlation function ξ_{123}, one can extract a single differential equation for the two-particle correlation functions and appropriate derivatives of the potentials arising from pairwise interactions. Exact solutions to this equation in simplified contexts exist, e.g., as in the case of electrons in an unmagnetized, thermalized plasma (Thorne and Blandford, 2017).

In this chapter, we wish to access the two-point correlation function in a data-driven way. Thus we turn our consideration to the correlation function in galactic number counts familiar from the analysis of cosmic large-scale structure (Peebles and Peebles, 1993); we employ Peebles and Peebles (1993) in what follows and refer to that reference for all details. The joint probability of finding two galaxies, which is assumed to be stationary, at separation r centered within volume elements dV_1 and dV_2, respectively, is $dP_2 = n^2(1 + \xi(r/r_0))dV_1dV_2$, where the probability to find one galaxy is $dP_1 = ndV$. In this context $\xi(r/r_0)$, the two-point correlation function, is dimensionless, and it depends on r_0, a characteristic clustering length, which is determined from observations. If the universe is homogeneous, we can convert this quantity to an angular correlation function that can be directly determined from the data by including a selection function S_i which determines the likelihood that a galaxy i at some distance is bright enough to be detected. With this, the joint probability becomes

$$dP_2 = n^2 d\Omega_1 d\Omega_2 \int r_1^2 dr_1 r_2^2 dr_2 \, (1 + \xi(r_{12}/r_0)) \, S_1 S_2 \,, \tag{8.4}$$

and thus we have

$$dP_2 = N^2 d\Omega_1 d\Omega_2 (1 + w(\theta)) \,, \tag{8.5}$$

with

$$w(\theta) = \frac{\int r_1^2 dr_1 r_2^2 dr_2 \xi(r_{12}/r_0) S_1 S_2}{(\int r^2 dr S)^2} \,, \tag{8.6}$$

where $r_{12} = (r_1^2 + r_2^2 - 2r_1 r_2 \cos\theta)^{1/2}$ and N is the mean number of galaxies per steradian. In order to assess $w(\theta)$ from the observational data, the Landy-Szalay (LS) estimator (Landy and Szalay, 1993) is employed, though other choices are possible (Wall and Jenkins, 2012). In this method the data D with d points is compared to a reference model R with r points, which is comprised of randomly distributed galaxies, and three separate histograms are constructed: RR, DD, and DR. Each histogram counts the number of pairs of stars at separations of θ to $\theta + d\theta$, and DD counts these pairs using the data, RR counts them within the reference model, and DR counts the number of cross-correlation pairs, to yield

$$w_{\rm LS}(\theta) = \frac{RR(\theta) - 2DR(\theta) + DD(\theta)}{RR(\theta)} \,, \tag{8.7}$$

where the histograms must be suitably normalized.

We now segue to the two-point correlation function suitable to our studies in the Milky Way. We note that our selected Gaia DR2 set for the range of G-band magnitudes, line-of-sight source densities, distances, and colors we consider is exceptionally complete, so that we have no need for a selection function. However, complete velocity information is only available for a sample of stars which tend to be brighter than the ones in our sample. We thus turn to a density-density correlation function. Specifically we note that the density associated with the distribution function

is $\rho(\mathbf{x}, t) = M \int d^3\mathbf{v}\, f(\mathbf{v}, \mathbf{x}, t)$, where M is the total mass of the system. Thus we define the spatial correlation function $\rho_{12}(\mathbf{x}_{12}, t)$, where

$$\rho_{12}(\mathbf{x_{12}}, t) \equiv \left\langle \sum_{i=1}^{N} \rho(\mathbf{x}_i)\rho(\mathbf{x}_i + \mathbf{x}_{12}) \right\rangle , \tag{8.8}$$

In this case, we examine purely spatial correlations, and we do so for the full, 3-dimensional positions of the stars in our sample. The LS Estimator is:

$$\xi_{\rm LS}(q_i) = \frac{RR(q_i) - 2DR(q_i) + DD(q_i)}{RR(q_i)}, \tag{8.9}$$

where the histograms count the number of pairs of stars which are separated by some distance q_i to $q_i + dq_i$, where q_i represents either x, y, or z, DD counts these pairs for correlations within our Gaia data set, RR counts the correlations within a mock sample generated via a Metropolis algorithm, and DR counts the cross-correlation pairs between the two data sets. Please note that the Landy-Szalay estimator requires RR, DD, and DR be normalized such that they have unit areas (Wall and Jenkins, 2012). This normalization accounts for the potentially different numbers of stars in real and mock samples, as well as the fact that there are more cross-correlation pairs than pairs within one data set.

Further, we can slightly alter the general practice of computing the 2PCF by comparing two distinct data sets against one another, instead of comparing against samples drawn from a model-dependent mock catalogue. To this end, we replace the traditional definition of the RR histogram with another histogram based on real data, but in a distinctly different region than that used to build the DD histogram. For example, one can examine the difference in structure between the Northern hemisphere of the Galaxy and (a reflection of) the Southern hemisphere, so long as the geometries of the two regions are identical. This is enabled through the approximate reflection symmetry of the Galaxy, and thus acts as a new test of the symmetries of the Milky Way.

8.3 Methodology

Data Selection

For this study, we utilize the ultra-pure data set curated by Gardner, Hinkel, and Yanny (2020) and Hinkel, Gardner, and Yanny (2020b) as the sample boasts a very low relative parallax error without any known significant directional biases. The geometry of the cuts used is $R \in [7.0, 9.0]$ kpc, $\phi \in [174, 186]$ degrees, $|z| \in [0.2, 3.0]$ kpc, and latitude cuts of $|b| > 30$ degrees. Further, the Large and Small Magellanic Clouds (LMC and SMC, respectively) have been excised, as well as reflections thereof to aid in examination of both axial and reflection symmetries.

By avoiding known structures like the spiral arms and the LMC and SMC, our 2PCF analysis can therefore be sensitive to smaller or more diffuse structures within our Galaxy. Further, as the employed data set is very complete in the region of

study, and does not explicitly cut on any parameters which depend on the number of observations, we can be sure that any significant result that appears in the 2PCF is from real structure and not simply from missing stars, the Gaia scan-law, or from directional biases in parallax assessments. Finally, with a significant vertical reach, we are able to probe how correlations within the Galaxy change as we go out into the stellar halo.

Generation of Mock Samples

In order to illustrate various possible effects and how they bear out in the 2PCF, we create models of the Milky Way drawn from a distribution (Eq. 8.10) via the Metropolis algorithm (Metropolis et al., 1953a; Metropolis et al., 1953b). In practice, a "star" is generated in the middle of the desired geometry to be matched, and is then stepped randomly in the R and z directions 75,000 times, with a step size drawn randomly between 0 pc and up to 10 pc for R steps and up to 10 pc for z steps. Because the Galaxy is fairly axisymmetric away from the spiral arms (Gardner, Hinkel, and Yanny, 2020; Hinkel, Gardner, and Yanny, 2020b), we simply tack on an azimuthal coordinate drawn from a uniform distribution as we are modeling an out-of-plane geometry. All pseudo-random numbers were generated from the Mersenne Twister pseudo-random number generator (Matsumoto and Nishimura, 1998).

Our baseline model is an exponential disk in the radial coordinate with radial scale length $R_\mathrm{s} = 2.7$ kpc (Bovy, 2015; Widrow and Dubinski, 2005) and a uniform distribution in Galactic azimuth. The vertical distribution is a hyperbolic secant-squared model with scale height $z_\mathrm{s} = 280$ pc. Altogether, the fiducial model used in the model-model illustrations is:

$$n(R,z) = e^{-R/R_\mathrm{s}} \mathrm{sech}^2\left(\frac{z}{2z_\mathrm{s}}\right). \tag{8.10}$$

In an effort to reproduce the exact geometry of the data, cuts were applied after the generation of the model galaxy.

Construction of the 2PCF

In practice, the Two-Point Correlation Function is constructed via a number of steps. First, with both the Gaia data and mock data in hand, RR, DD, and DR were computed for a given coordinate direction. For the separation of two stars in the vertical direction, a simple absolute distance is computed. For the radial direction, x is used as a proxy. The same approach is used for the azimuthal separation of two stars. That is, we exploit the fact that our data is very close to the $\phi = 180°$ line so that a small angle approximation allows for the use of $y \approx R\phi$ as a proxy for azimuthal separation.

Next, the normalization factor of all three histograms are determined by simply summing the contents therein. The normalization factors are then applied, forcing each contribution to the Landy-Szalay estimator to have unit area. One particular caveat here is that our RR, DD, and DR histograms were cut off after a certain

length scale of interest for practical and computational reasons, meaning that the method of Wall and Jenkins (2012) must be tweaked slightly. That is, while there are indeed $n(n-1)/2$ pairs of stars in a data set of n stars, only considering the pairs out to a certain scale changes the area of the histograms. To account for this, we simply normalize each histogram by summing its contents and dividing the histogram through by that factor, instead of the $n(n-1)/2$ factor implied in Wall and Jenkins (2012).

8.4 Deconstructing the 2PCF

In order to better understand how the LS Estimator reveals structure, we have simulated a number of different effects and outline them in this section. In Fig. 8.1(a), the LS estimator is shown for z-separation distances and compares two data sets drawn from an identical distribution function. This control test illustrates the case where no structure exists, and indeed the LS estimator is consistent with zero. A result with structure is shown in Fig. 8.1(b), wherein two data sets are compared with markedly different scale heights. The first data set (D) has a scale height of $z_{\rm s} = 280$ pc, while the other (R) has a scale height of $z_{\rm s} = 420$ pc, and thus an excess of structure is found at small scales, and a dearth of structure is found at larger scales, resulting in the slanted estimator shown.

If instead of a smooth, hyperbolic-secant-squared distribution function, we use a DF with structure embedded in it, the LS estimator will then pick out the characteristic scales of that particular structure. For example, by introducing a toy-model of a vertical wave into one data set (D) as in Eq. 8.11,

$$n(R,z) = e^{-R/R_{\rm s}} \mathrm{sech}^2\left(\frac{z}{2z_{\rm s}}\right)(1+0.2\sin(8z)) \tag{8.11}$$

and comparing this against smoother data drawn from a hyperbolic-secant-squared distribution function (R), the LS estimator will indicate an excess of structure corresponding to the maxima of the density waves, and a dearth of structure near the trough of the density waves, as in Fig. 8.1(c). An interesting feature of anti-symmetric structure like that of the vertical waves found in (Widrow et al., 2012; Yanny and Gardner, 2013; Bennett and Bovy, 2018) is that any North-South comparison will result in increased significance in a structure search. In other words, when Northern data (DD) is compared against a reflection of the Southern data (RR), the anti-symmetric nature of the vertical waves results in the peaks in the North lining up with the troughs of the South, and thus the LS estimator strongly highlights this structural difference, as depicted in Fig. 8.1(d).

While of course helpful for illustrative purposes, the toy models in Fig. 8.1 are missing one key consideration. In selecting a reliable data set as free from observational artefacts as possible, we have implemented various cuts on *solarcentric* longitude and latitude. However, because the sun is not truly situated on the Galactic mid-plane, any analysis in galactocentric coordinates will necessarily run into problems caused by a geometry mismatch.

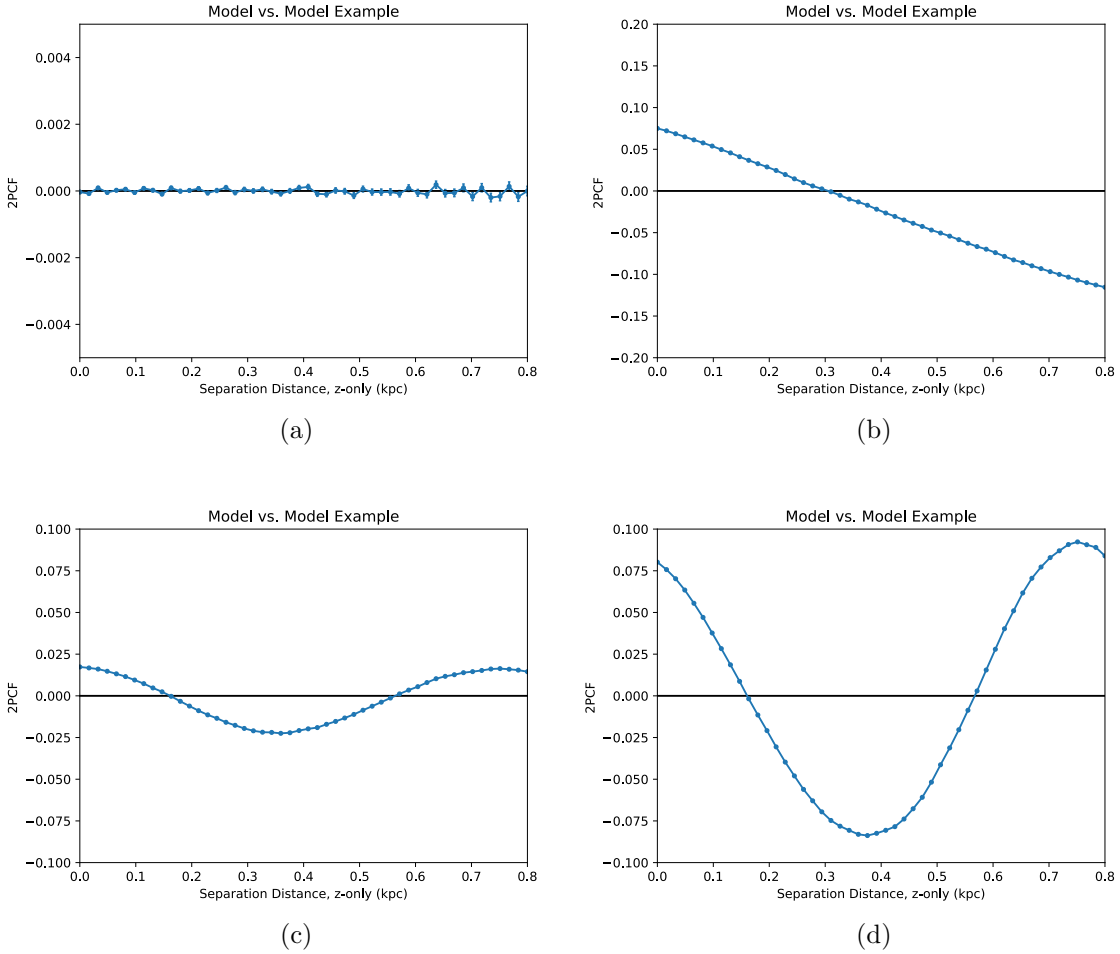

Figure 8.1: (a) The N vs. S z-2PCF comparing two models drawn from identical distribution functions. (b) The N vs. S z-2PCF comparing two models drawn from distribution functions with different scale heights. In this case, one model has a scale height of $z_s = 280$ pc, while the other has a scale height of $z_s = 420$ pc. (c) The z-2PCF comparing a model with vertical density waves against a smooth model. (d) The N vs. S z-2PCF comparing a model with vertical density waves in the North against the same model with vertical density waves in the South. The wave is modelled as $n(R,z) = e^{-R/R_s}\text{sech}^2(z/2z_s)(1+0.2\sin(8z))$, and thus the anti-symmetric nature of the wave results in more significant correlations in the North vs. South analysis than that comparing the density wave model against a smooth model.

To better illustrate this concept, let us consider Fig. 8.2. In panel (a), we repeat the control test of Fig. 8.1(a), but now include cuts on latitude ($|b| > 30°$) as well as the LMC and SMC cuts of Gardner, Hinkel, and Yanny (2020) and Hinkel, Gardner, and Yanny (2020b). In this case, a $z_\odot$ shift has not been applied, and thus these toy models implicitly assume $z_\odot = 0$ pc. It is clear from panel (a) that l and b

cuts alone do not bias the LS estimator if $z_\odot = 0$ pc. Indeed, even if the samples have an egregiously large mismatch in the number of stars, as in Fig. 8.2(b), the LS estimator still takes into account both the post-cut geometry as well as normalization considerations, correctly resulting in no indication of structure.

However, if $z_\odot \neq 0$, a galactocentric analysis will incur substantial geometric effects in the LS estimator, as seen in Fig. 8.2(c). In this case, an offset of $z_\odot = 20$ pc (Bennett and Bovy, 2018) has been included in the models, such that solarcentric cuts on l and b effectively emanate from a region which is not coincident with the Galactic mid-plane. This difference in geometries, North and South, is falsely registered in the LS estimator as structure, even though the models are identical in all other regards. Thus, we must be extremely careful to avoid geometric differences caused by a combination of non-zero $z_\odot$ and cuts on l and b.

There are two potential fixes for this issue. First, it is possible to select data such that the l and b cuts are avoided entirely. In these cases, an analysis in galactocentric coordinates works just fine, as the solarcentric cuts simply do not enter the geometry in question. To illustrate this point, Fig. 8.2(d) shows how samples drawn from identical distributions which avoid the l and b cuts result in an LS estimator which is consistent with zero. In this particular example, we have raised the minimum value of z to which we probe, and have restricted the region of R and ϕ as well. While certainly a viable workaround for the geometry mismatch issue stemming from solarcentric cuts in a Galactocentric coordinate system, this procedure limits the regions that we can explore.

To illustrate this, the regions of the data set impacted by the l and b cuts are shown via their projections in the $R - z$ and $z - \phi$ planes in Figs. 8.3(a) and 8.3(b) respectively. As the latter shows, increasing the minimum z to which we probe is an effective way of avoiding the l and b cuts, at the cost of cutting out the region with the highest number of stars. Regions at low-z are still available to explore with this method in limited regions of R, as shown in the former.

An alternative fix for the solarcentric cut mismatch issue is to simply conduct the analysis in solarcentric coordinates. That is, we can assume $z_\odot = 0$ pc. While not strictly true, we show that any false correlations due to this incorrect choice of $z_\odot$ are small in Fig. 8.3(c), if the data are drawn from otherwise identical distributions. In particular, the correlations we find in this case are $\xi_{\rm LS} < 0.001$, and are caused by the fact that we are sampling slightly different regions of the Galaxy's distribution function in the North and in the South. To wit, the 20 pc $z_\odot$ "shift" is small compared to the scale height of ~ 280 pc, and so the resulting effect is small, but is nonetheless important vis-a-vis the smallest significant correlation we can probe. Clearly, any structure will need to exceed this background correlation of about 0.0005 in Fig. 8.3(c). Moreover, for high $|z|$, the disk's density profile falls off approximately as an exponential decay function. Because a shift in an exponential function is equivalent to an overall normalization factor, and because the LS estimator takes into account differences in normalization, a $z_\odot$ shift will not matter for high $|z|$. In general, though, other distributions would still retain some effects from a $z_\odot$ shift. As shown in Fig. 8.3(d), neglecting $z_\odot$ results in negligible correlations for an otherwise identical model-model comparison, indicating the stars in our model do fall

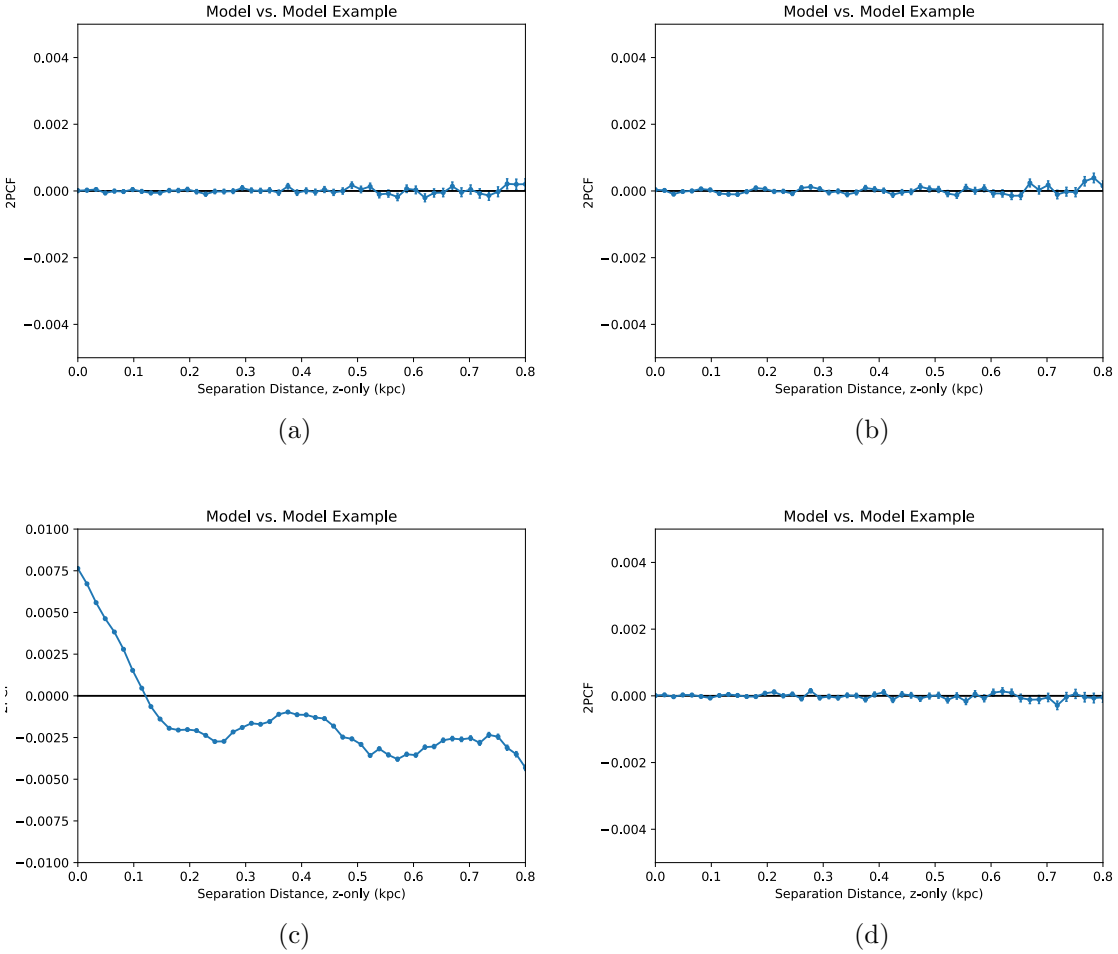

Figure 8.2: (a) The N vs. S z separation 2PCF comparing two models drawn from identical distribution functions, including $|b| > 30°$ and the set of LMC/SMC cuts mentioned in text. (b) The same scenario as panel a, but with a 20% mismatch in the number of stars between the two models. (c) The N vs. S z-2PCF comparing two models drawn from a distribution function which accounts for $z_{\odot}$, resulting in a geometry mismatch, North and South, due to the solarcentric cuts emanating from a location other than the mid-plane. (d) The N vs. S z-2PCF comparing two models drawn from a distribution function which accounts for $z_{\odot}$, but with Galactocentric geometry chosen in such a way that the l and b cuts are avoided. In this particular example, $7.9 < R < 8.3$ kpc, $179 < \phi < 181°$, and $0.3 < |z| < 2.0$ kpc, and thus the $|b| > 30°$ cuts and the LMC/SMC cuts do not impact the geometry of the sample, and thus there is no geometry mismatch from solarcentric cuts.

off approximately exponentially at high-$|z|$.

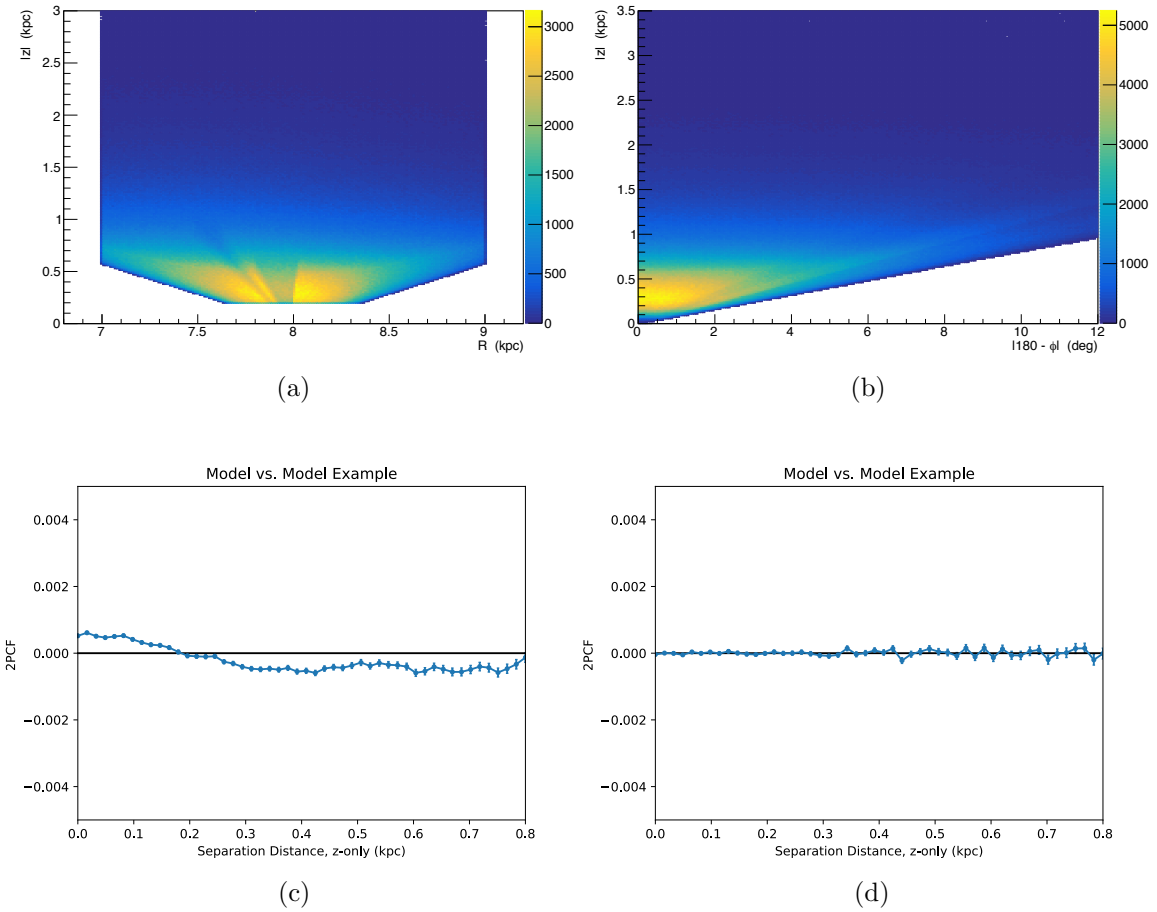

Figure 8.3: (a) The $R-z$ projection of the data set, illustrating the regions free of l, b cut effects. (b) The $\phi - z$ projection of the data set, illustrating the regions free of l, b cut effects. (c) A solarcentric analysis which does not suffer from the geometry mismatch like the analysis in panel c of Fig. 8.2. Here, $7.6 < R < 8.2$ kpc, $176 < \phi < 184°$, $0.2 < |z| < 2.0$ kpc. In this case the small, non-zero correlation arises due to the sampling of slightly different regions of the Galactic distribution function as a result of the $z_\odot$ offset. (d) A solarcentric analysis similar to panel c, but for higher z: $1.2 < |z| < 3.0$ kpc. The systematic, lower correlation limit to which one can probe is significantly smaller for regions well above the mid-plane, as explained in the text.

8.5 Vertical Structure

With a firmer picture of the types of correlations we can probe, we now look at the Gaia vs. Gaia 2PCF in order to better understand the structures behind the various broken symmetries we observe. In this section, we outline the results for the vertical separations of stars, and do so by comparing the North against the South, as well as the Left ($\phi > 180°$) with the Right ($\phi < 180°$). The two comparisons test reflection

and axial symmetry respectively.

For the vertical Two-Point Correlation Function analysis (z2PCF hereafter) we examine "wedges" of data that extend 200 pc in R, 1° in ϕ, and from $0.2 < |z| < 2.0$ kpc, sampling within the same region as the simulation results above for easy comparison. The separation distances are computed up to 1.5 kpc in separation, as the geometry fundamentally limits the number of pairs near the maximal 1.8 kpc of separation possible in the wedges, corresponding to stars at the maximal $z = 2.0$ kpc and minimal $z = 0.2$ kpc. Each bin for the North vs. South analysis has a width of 15 pc.

As we demonstrate in Fig. 8.4, the Galaxy is highly correlated in the vertical direction, with an array of wave-like structures across the pictured regions. Moreover, the particular wave-like pattern observed differs from wedge to wedge. Interestingly, the most significant differences amongst the waves observed appear at the highest separation distances, or equivalently at high z.

These waves mostly correspond to the known vertical waves discovered by Widrow et al. (2012), but benefit from the $\mathcal{O}(N^2)$ statistics afforded by pair counting statistics, as opposed to star counts which go as the number of stars, $\mathcal{O}(N)$. Indeed, there appears to be peaks which may be unaccounted for in comparison to the corresponding asymmetry results, as motivated by Fig. 8.5. These differences – especially at higher $|z|$ – may speak to differences in the vertical waves across the plane, or perhaps additional, as yet unappreciated effects.

In addition to North-South differences, axial differences among the vertical waves can be assessed via a Left-Right comparison. That is, a wedge of data above on the left (say $180° < \phi < 181°$) can be reflected across the $\phi = 180°$ ray and compared against a wedge on the right (say $179° < \phi < 180°$). Non-zero correlations from such a study speak to axial differences in the vertical waves – suggesting the waves are not perfectly planar as modelled by Widrow et al. (2012).

Indeed, Fig. 8.6 and 8.7 illustrate the axial differences of vertical structure in the North and in the South respectively. A number of observations are apparent. First, structural variations appear for the waves in the Northern hemisphere, but hardly at all in the Southern hemisphere. Additionally, the azimuthally adjacent wedges (panels a and b of Fig. 8.6) exhibit much less structure than wedges which are not azimuthally adjacent. As perturbations like the vertical waves would feel their own self-gravity, it would make sense for nearby wedges to be in phase, or at least nearly so. However, some effect must still be causing substantial differences in the wave structures across the plane, but appears to only be operative in the North. Again, the largest differences between the various waves occur at higher z.

8.6 Radial and Azimuthal Structure

We have seen how the vertical structure of the Galaxy can change substantially with radius and azimuth, so it is natural to ask if in-plane correlations exist as well. Indeed, the Gaia snail (Antoja et al., 2018), axial symmetry breaking (Hinkel, Gardner, and Yanny, 2020b; Gardner, Hinkel, and Yanny, 2020), the axial differences in vertical structure noted in this paper and Ferguson, Gardner, and Yanny (2017), as well as

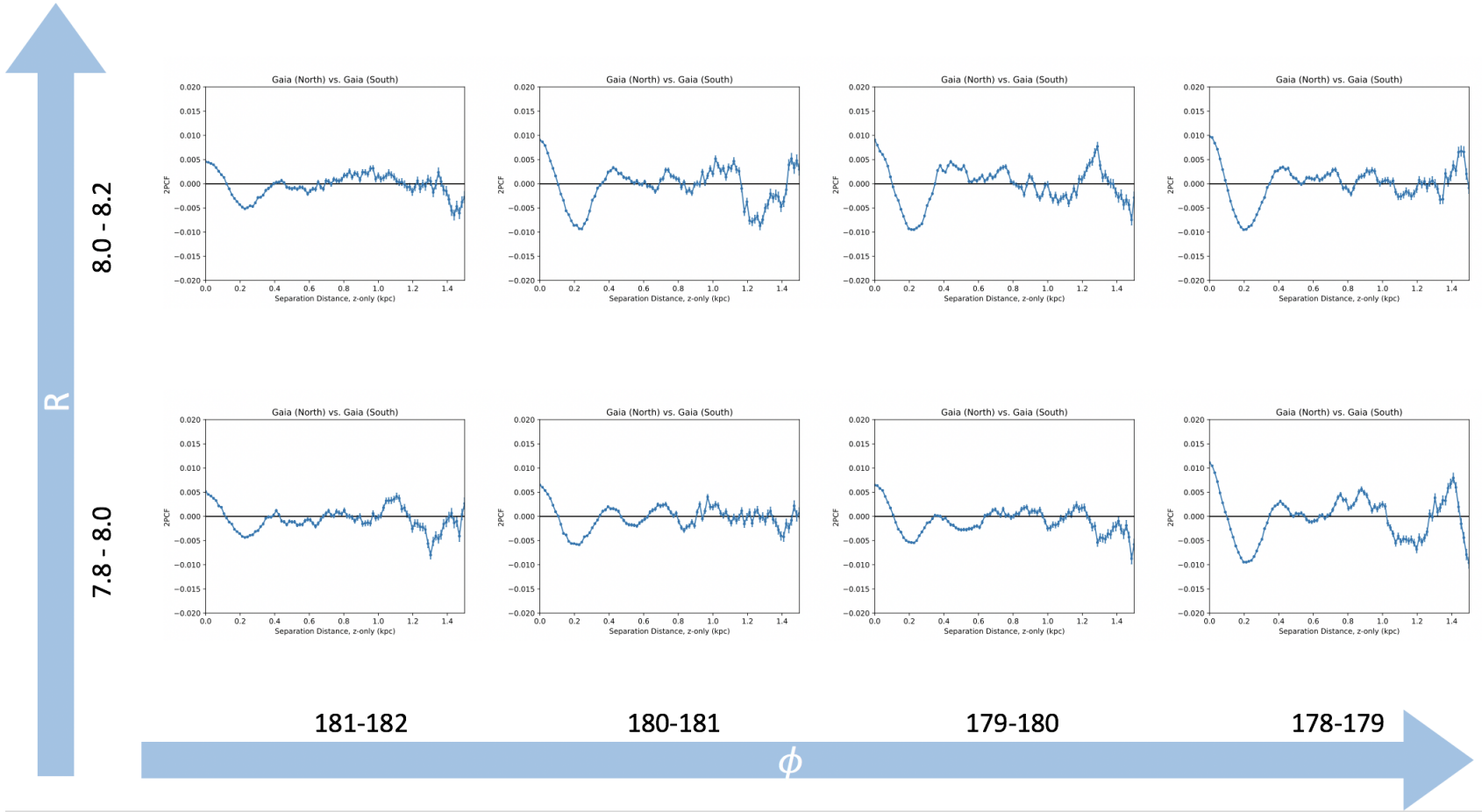

Figure 8.4: Several Gaia-Gaia, vertical separation 2PCF computations for various R, ϕ wedges, comparing the vertical structure in the North vs. the South. The region pictured exhibits highly correlated stars, revealing vertical waves in a new light.

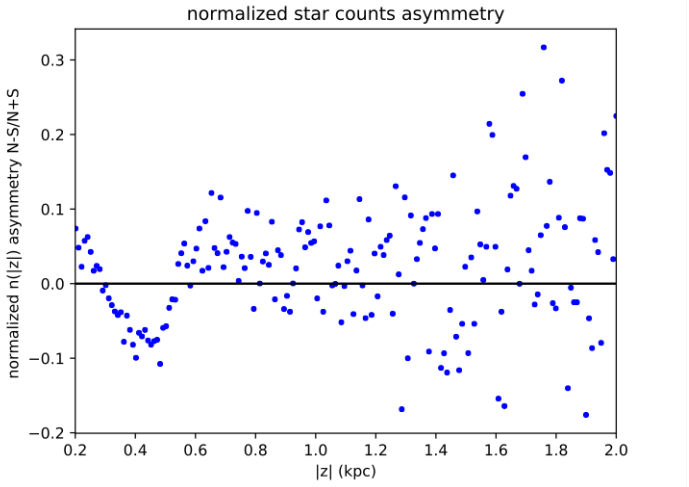

(a)

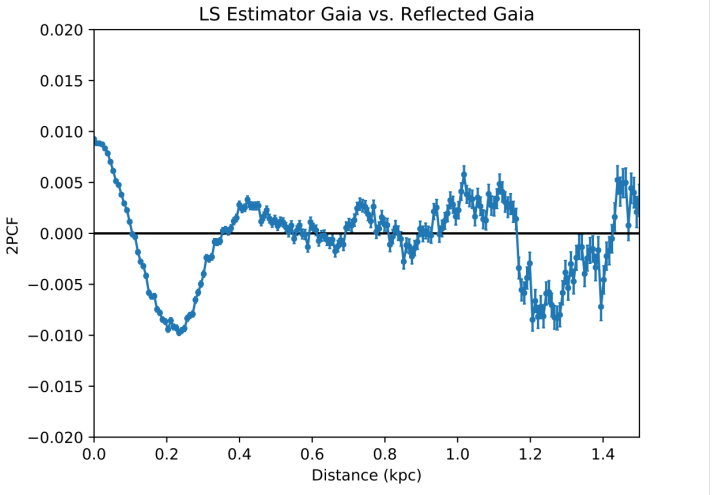

(b)

Figure 8.5: A comparison of the North-South asymmetry (a) and the Gaia-Gaia, North vs. South vertical 2PCF (b) in an exemplar region of the Galaxy. The peaks and troughs in the asymmetry can be linked to some – but seemingly not all – of the peaks in the z2PCF. Namely, the crests of the wave as seen in the asymmetry at $|z| \approx 0.2$ and $|z| \approx 0.6$ kpc result in the peak near a vertical separation distance of about 0.4 kpc in the 2PCF. The peak-to-trough distances between the first two peaks and the first trough are around 0.2 kpc, and this registers as a cross-correlation in the LS estimator and thus a trough in the 2PCF near 0.2 kpc. Error bars are omitted in the asymmetry plot for clarity. The vertical structure comes into focus much more clearly in the 2PCF due to the N^2 statistics when compared to the asymmetry analysis for the same region.

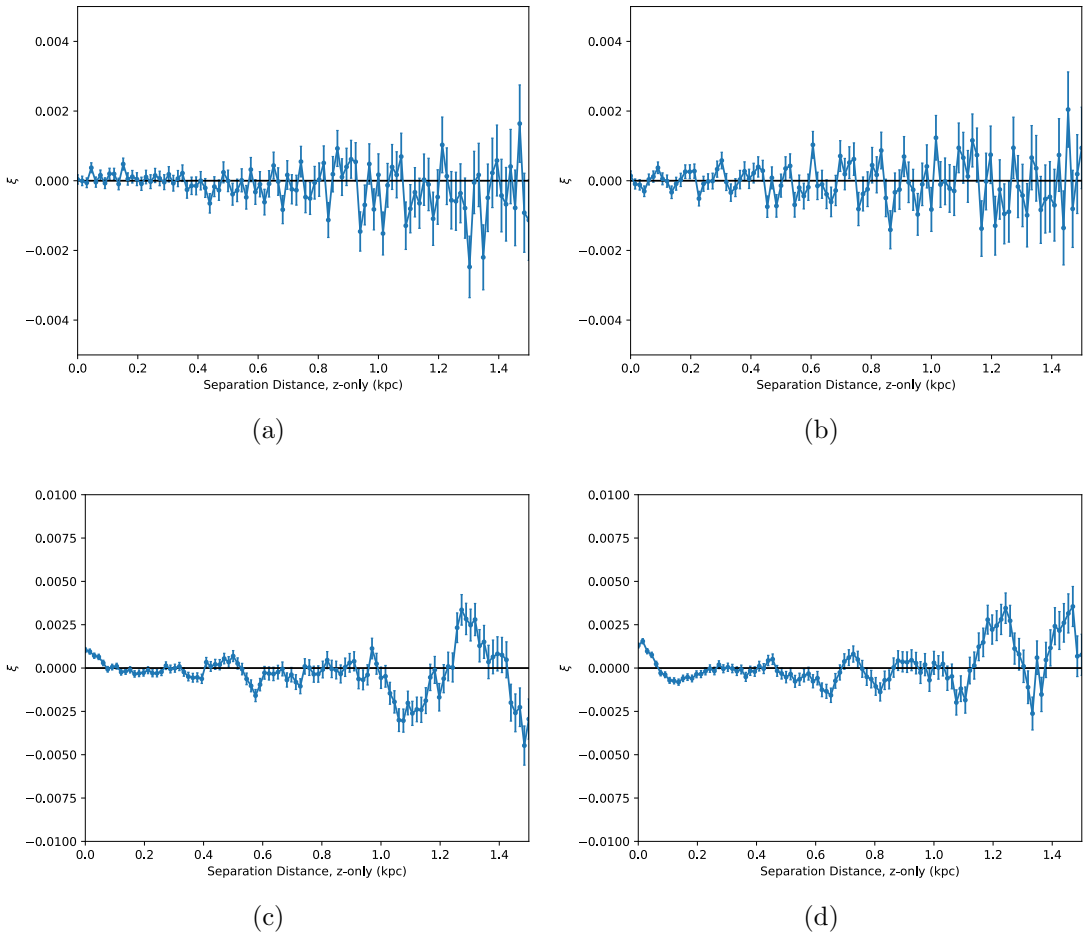

Figure 8.6: (a) The Left-Right z2PCF for $z > 0$ kpc, $7.8 < R < 8.0$ kpc, and $179° < \phi < 180°$ vs. $180° < \phi < 181°$. (b) The Left-Right z2PCF for $z > 0$ kpc, $8.0 < R < 8.2$ kpc, and $179° < \phi < 180°$ vs. $180° < \phi < 181°$. (c) The Left-Right z2PCF for $z > 0$ kpc, $7.8 < R < 8.0$ kpc, and $178° < \phi < 179°$ vs. $181° < \phi < 182°$. (d) The Left-Right z2PCF for $z > 0$ kpc, $8.0 < R < 8.2$ kpc, and $178° < \phi < 179°$ vs. $181° < \phi < 182°$.

the complex corrugation patterns suggested by Bland-Hawthorn and Tepper-Garcıa (2021) point to the real possibility of non-zero radial and azimuthal correlations. Thus, we examine radial and azimuthal structure via the x2PCF and y2PCF. In our case, x and y act as proxies for R and ϕ near the solar neighborhood.

For the x and y Two-Point Correlation Function analysis we again examine "wedges" of data, this time with $7.6 < R < 8.4$ kpc, 2° in ϕ, and for various "slices" of z. The separation distances are computed up to 0.4 kpc in separation for x and 0.25 kpc in y, as the geometry again limits the number of pairs beyond these scales. Each bin for the x and y analyses has a width of 8 pc.

Left-Right structural differences in the x-direction are shown in Fig. 8.8 for various

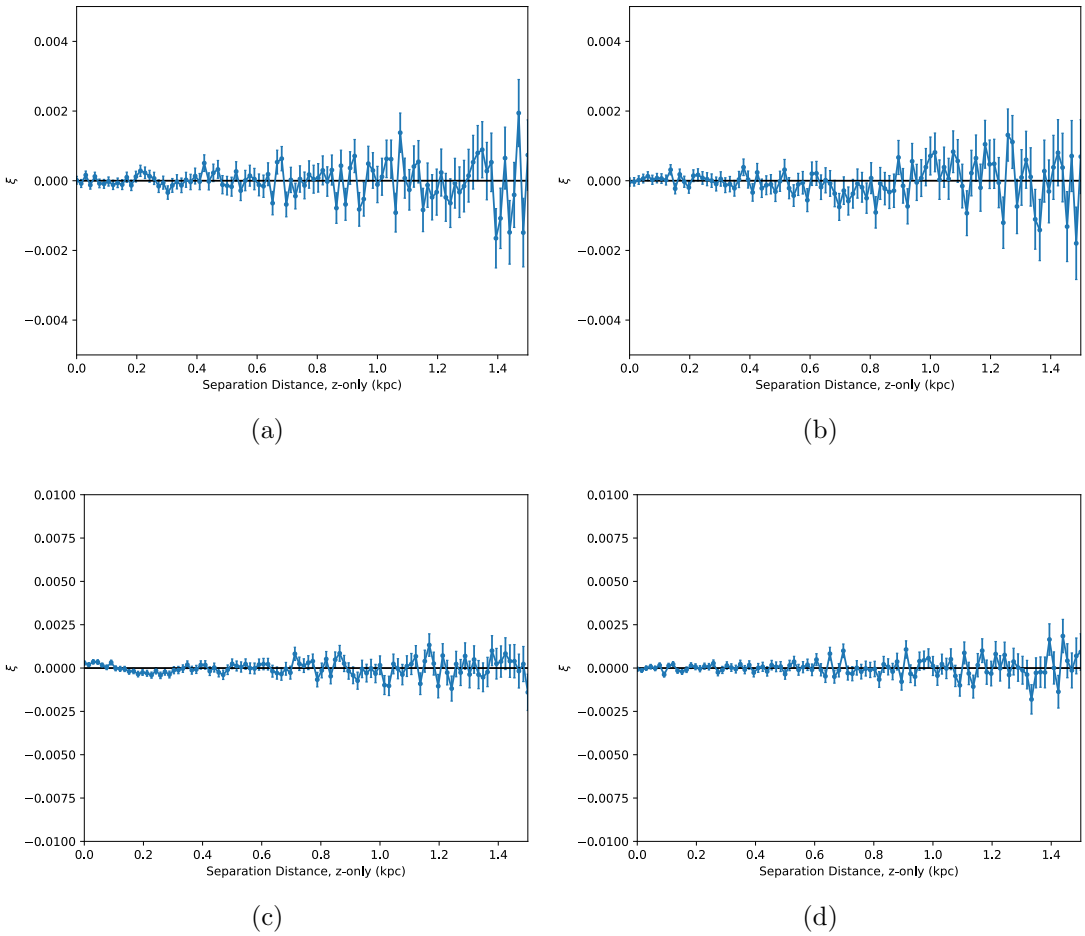

Figure 8.7: (a) The Left-Right z2PCF for $z < 0$ kpc, $7.8 < R < 8.0$ kpc, and $179° < \phi < 180°$ vs. $180° < \phi < 181°$. (b) The Left-Right z2PCF for $z < 0$ kpc, $8.0 < R < 8.2$ kpc, and $179° < \phi < 180°$ vs. $180° < \phi < 181°$. (c) The Left-Right z2PCF for $z < 0$ kpc, $7.8 < R < 8.0$ kpc, and $178° < \phi < 179°$ vs. $181° < \phi < 182°$. (d) The Left-Right z2PCF for $z < 0$ kpc, $8.0 < R < 8.2$ kpc, and $178° < \phi < 179°$ vs. $181° < \phi < 182°$.

z slices in the Northern hemisphere, and increase in z from panel (a) through panel (e). Interestingly, the stars in the North are indeed correlated in the x-direction, especially at lower $|z|$. The same is not true for the South, however, as depicted in Fig. 8.9. While both the North and the South share some structural similarities at the lowest $|z|$ values, the South lacks the structure seen in the North in the region with $0.3 < |z| < 1.2$ kpc (panels b-d).

This preponderance of x-direction structure in the North and lack of x-direction structure in the South is consistent with the vertical studies above. Indeed, the vertical waves we observe exhibit marked Left-Right structural differences in the North (Fig. 8.6), but not the South (Fig. 8.7). In other words, the seemingly out-

of-phase (axial symmetry breaking) vertical waves appear to create a corrugation pattern of some kind, even beyond the region of the known Gaia snail (Antoja et al., 2018).

Additionally, slight hints of y-direction structure exist in the North (Fig. 8.10), but not the South (Fig. 8.10). While not as significant as the x-direction structure seen previously, the stars nonetheless appear to be correlated. Moreover, a tantalizing, wave-like structure appears at the highest $|z|$ values in the North, perhaps hinting at a newly discovered structure: an azimuthal wave of some sort. The wavelength of the wave-like correlation pattern is about 40-50 pc.

8.7 A Brief Look at Data-Model Comparisons

As discussed previously, we have focused on exploiting Galactic symmetries at least in small part to avoid the problem of modelling the Galaxy. Indeed, the wide array of structural variations and effects seen in the preceding sections makes it clear that a simple, smooth, steady-state model of the Galaxy is *without a doubt* insufficient. In this section, we nonetheless pivot back to a more traditional 2PCF analysis, and briefly compare structure in the Gaia data against a smooth model for the Milky Way, though we leave a more detailed analysis to a future work.

With the caveat that the 2PCF may reveal a poor fit form over any diffuse structure not already apparent in the one-body distribution function, we examine a high-z region of our sample and compare this to a simple model. Namely, we compare the region with $7.6 < R < 8.4$ kpc, $176^\circ < \phi < 184^\circ$, and $1.2 < z < 3.0$ kpc, to an exponential disk of the form:

$$n(R, z) \propto e^{-|z|/z_s} e^{-R/R_s} \tag{8.12}$$

where $z_s = 0.465$ kpc and $R_s = 2.7$ kpc (recall, the normalization should not matter to the LS Estimator, which accounts for differing numbers of stars between samples). The fit of the data as well as the differences in vertical structure as revealed by the 2PCF are shown in Fig. 8.12.

Right away, it is clear that the fit may automatically absorb some structure, and that slight deviations of the data from the fit will be behind some of the correlations we find. While the 2PCF does uncover some slight hint of clustering at smaller spatial scales, it is unclear if this is due to small failures of fit, true structure, or both. We leave the development of a method to discern this difference to a future work.

8.8 Conclusions

We have introduced here a new realization of the Two-Point Correlation Function (2PCF). By exploiting reflection symmetry and axial symmetry, we have compared the structural differences of various regions of the Galaxy against one another. Moreover, we have examined the 2PCF for 1-D separations in x, y, and z only, uncovering more information regarding the orientation of the structures we find.

Ultimately, it is clear from this analysis that the stars in our Galaxy are not perfectly uncorrelated. In fact, stars are highly-correlated in the vertical direction

– confirming and even enhancing previous discoveries of vertical waves in the Milky Way disk (Widrow et al., 2012; Yanny and Gardner, 2013; Bennett and Bovy, 2018). These wave-like, vertical structures exhibit small differences in phase and amplitude, especially at higher $|z|$, and non-adjacent wedges of data show marked azimuthal differences in the waves, also at higher $|z|$.

In addition to the aforementioned vertical structure, there appears to be substantial radial structure at lower $|z|$, though this radial structure is much more apparent in the Northern hemisphere. Radial structure in the North extends all the way up to 1.2 kpc above the plane, while radial structure in the South is mostly confined to $0.2 < |z| < 0.3$ kpc. This North heavy structure trend is consistent with the azimuthal differences in vertical structure seen in the North, and with the relative lack of structure seen in the South.

Further, some hints of azimuthal structure exist – again predominantly in the North. Some slight azimuthal correlations exist at low $|z|$ in the North, but otherwise the thin disk appears to be devoid of azimuthal structure away from the spiral arms. Very interestingly, an azimuthal wave structure with a wavelength around 40 or 50 pc is apparent at high $|z|$ in the North, speaking to previously undiscovered dynamical effects. It is not obvious if these effects are related to the Gaia phase space spiral, though they may well be.

As this analysis is effected in solarcentric coordinates, the true Galactic mid-plane is really below our $z = 0$ plane. As such, the lack of structure in the South, compared to the North suggests that the mid-plane itself likely has very little structure away from the spiral arms. This fact seems to disfavor the warping of the disk as a cause of this structure, as warping would presumably be visible both in the North and South, and would be *more* noticeable in the South, near the true mid-plane – the opposite of what we observe.

Additionally, we find evidence of substantial structural variations across R and ϕ in the vertical direction. Not only have we resolved the vertical waves discovered by Widrow et al. (2012) in our z2PCF analysis, a Left-Right comparison shows significant differences at high $|z|$, perhaps suggesting that the waves are disrupting, out of phase (i.e. not perfectly planar waves, agreeing with the findings of Ferguson, Gardner, and Yanny (2017)), or superimposed on an entirely different effect, like the corrugations suggested by Bland-Hawthorn and Tepper-Garcıa (2021). More study is required to determine the precise origin of this correlation we find.

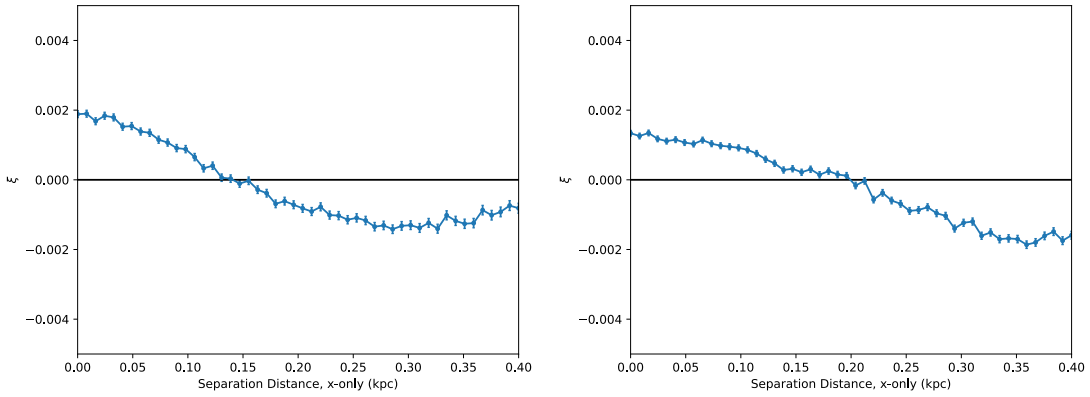

(a) (b)

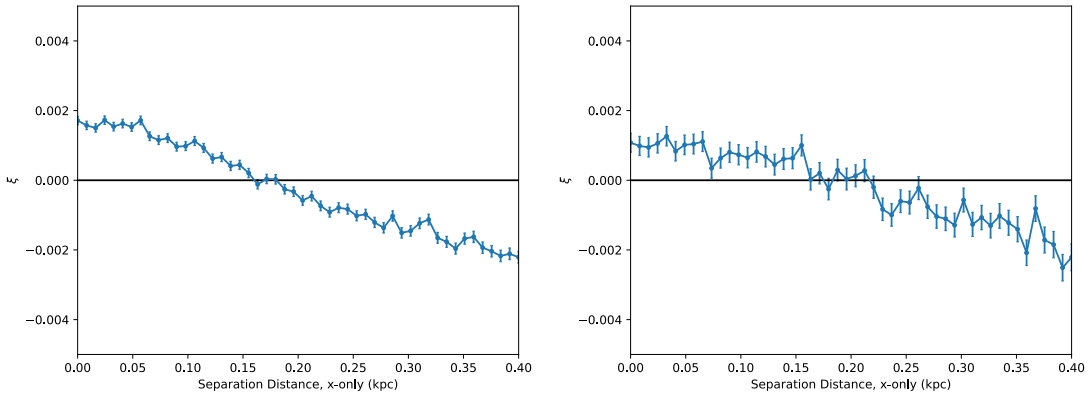

(c) (d)

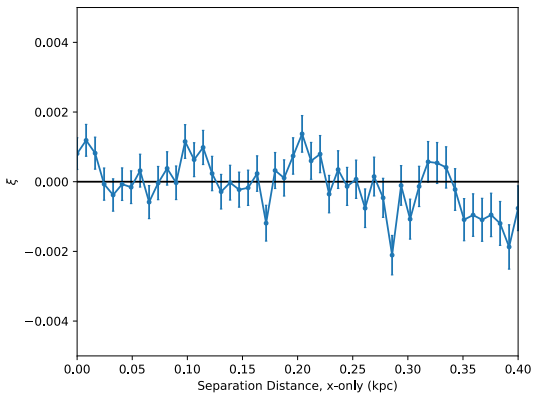

(e)

Figure 8.8: Left ($180° < \phi < 182°$) vs. Right ($178° < \phi < 180°$) comparisons of structure in the x-direction for the Northern hemisphere, with $7.6 < R < 8.4$ kpc, and for various slices of $|z|$. (a) $0.2 < |z| < 0.3$ kpc, (b) $0.3 < |z| < 0.5$ kpc, (c) $0.5 < |z| < 0.8$ kpc, (d) $0.8 < |z| < 1.2$ kpc, (e) $1.2 < |z| < 3.0$ kpc.

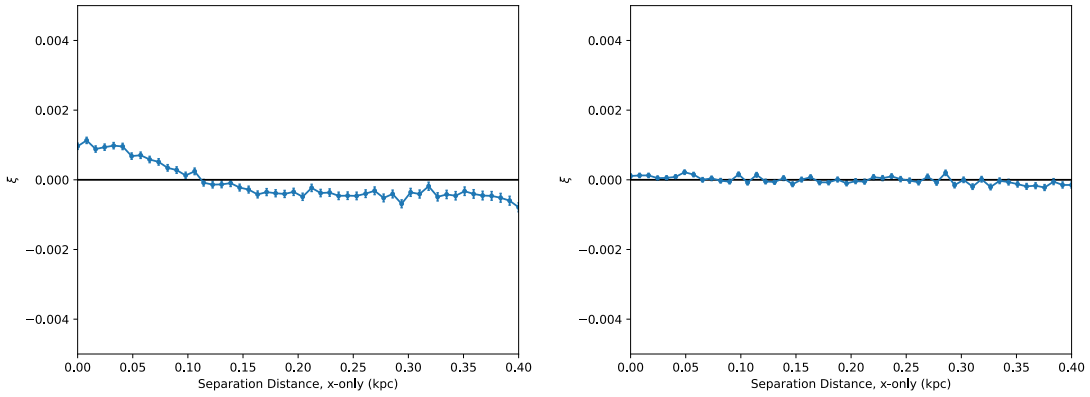

(a) (b)

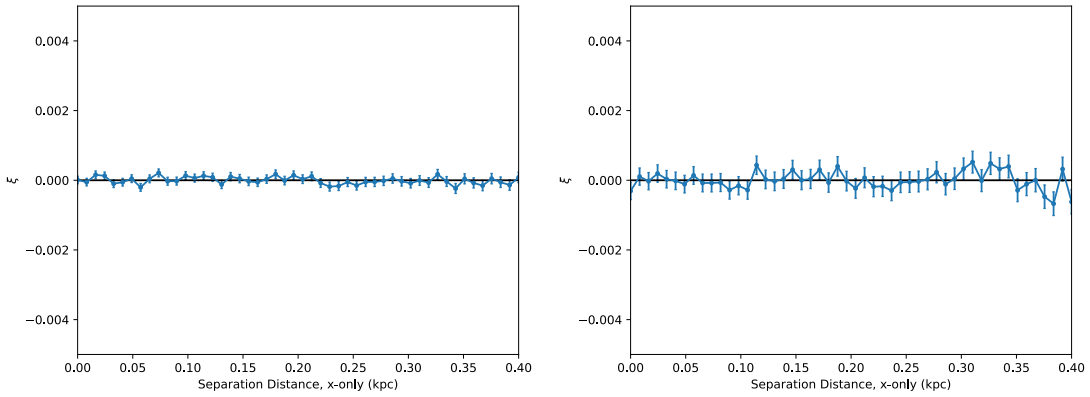

(c) (d)

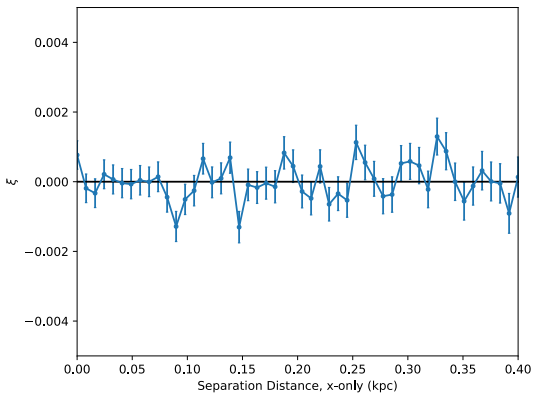

(e)

Figure 8.9: Left ($180° < \phi < 182°$) vs. Right ($178° < \phi < 180°$) comparisons of structure in the x-direction for the Southern hemisphere, with $7.6 < R < 8.4$ kpc, and for various slices of $|z|$. (a) $0.2 < |z| < 0.3$ kpc, (b) $0.3 < |z| < 0.5$ kpc, (c) $0.5 < |z| < 0.8$ kpc, (d) $0.8 < |z| < 1.2$ kpc, (e) $1.2 < |z| < 3.0$ kpc.

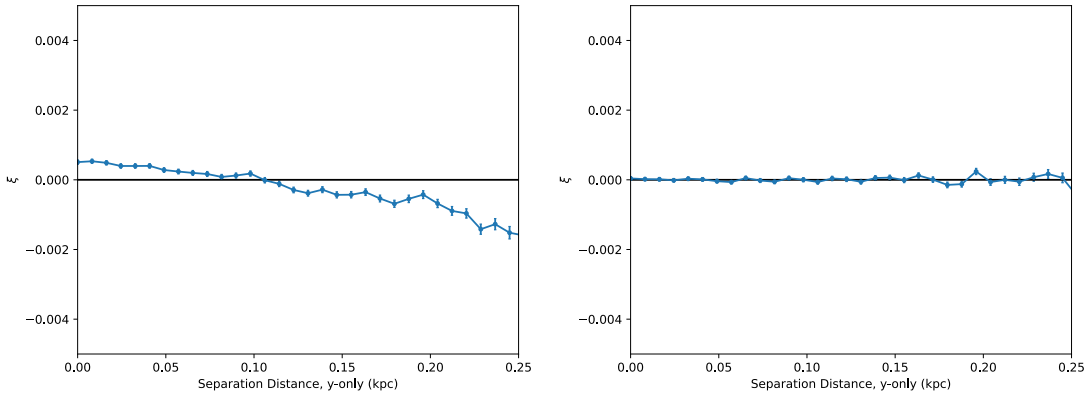

(a)

(b)

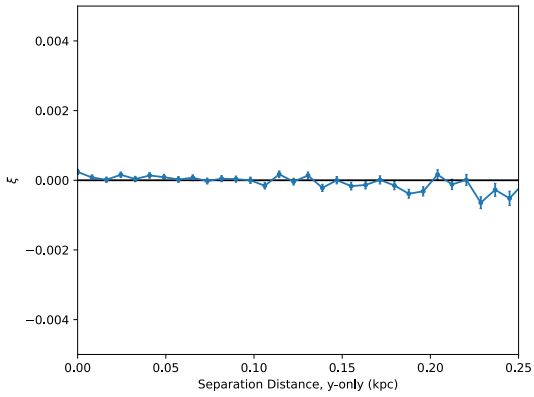

(c)

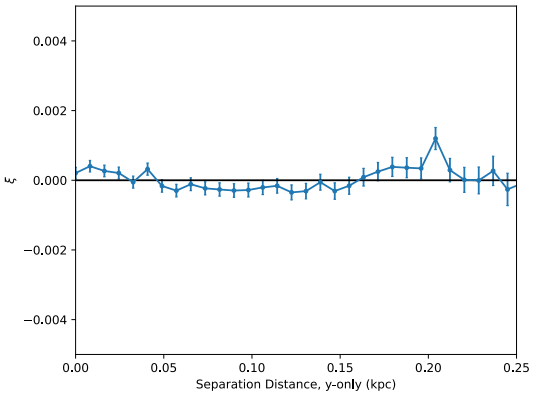

(d)

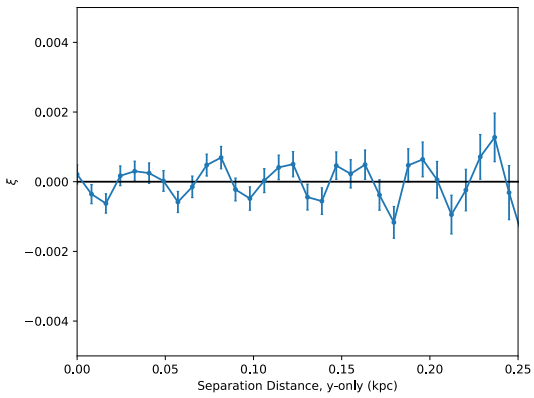

(e)

Figure 8.10: Left ($180° < \phi < 182°$) vs. Right ($178° < \phi < 180°$) comparisons of structure in the y-direction for the Northern hemisphere, with $7.6 < R < 8.4$ kpc, and for various slices of $|z|$. (a) $0.2 < |z| < 0.3$ kpc, (b) $0.3 < |z| < 0.5$ kpc, (c) $0.5 < |z| < 0.8$ kpc, (d) $0.8 < |z| < 1.2$ kpc, (e) $1.2 < |z| < 3.0$ kpc.

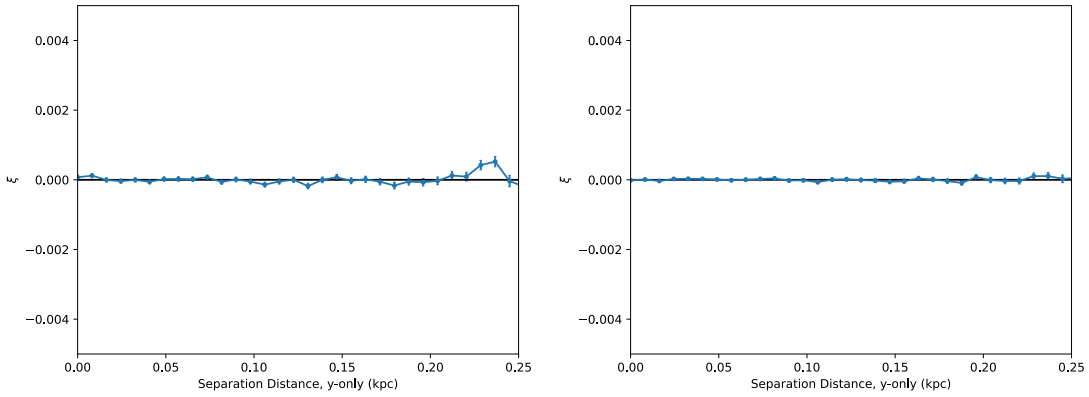

(a)

(b)

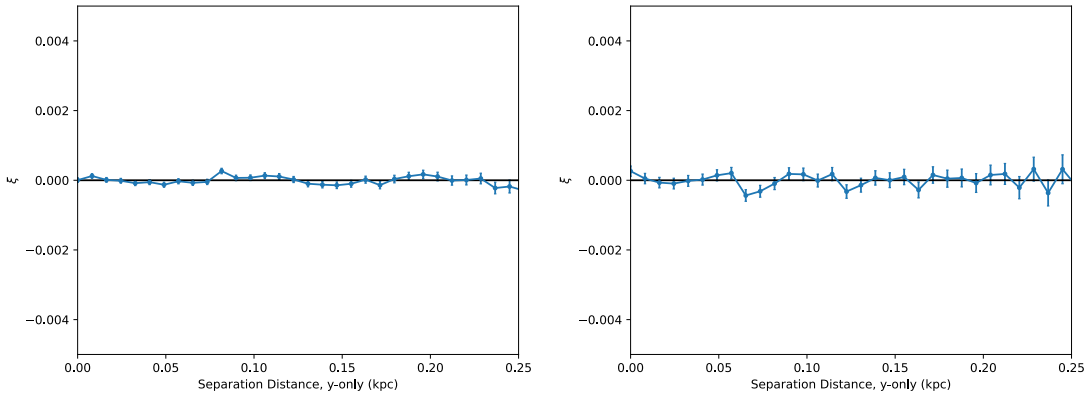

(c)

(d)

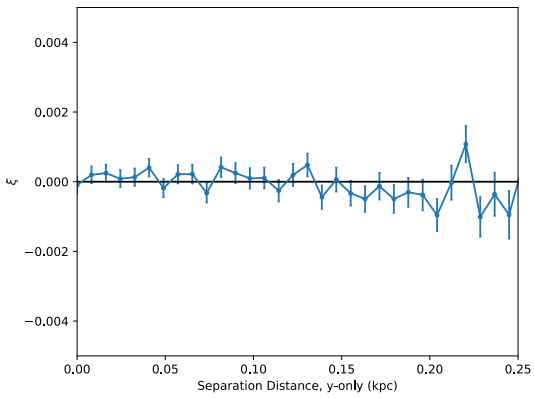

(e)

Figure 8.11: Left ($180° < \phi < 182°$) vs. Right ($178° < \phi < 180°$) comparisons of structure in the y-direction for the Southern hemisphere, with $7.6 < R < 8.4$ kpc, and for various slices of $|z|$. (a) $0.2 < |z| < 0.3$ kpc, (b) $0.3 < |z| < 0.5$ kpc, (c) $0.5 < |z| < 0.8$ kpc, (d) $0.8 < |z| < 1.2$ kpc, (e) $1.2 < |z| < 3.0$ kpc.

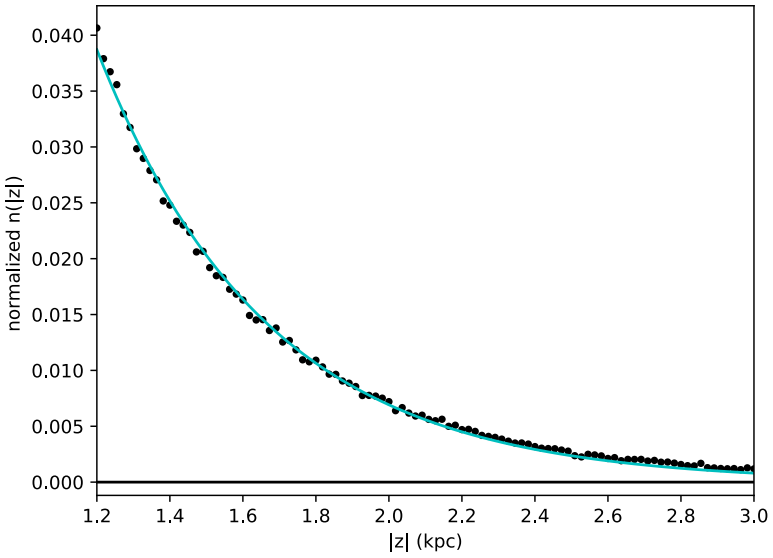

(a)

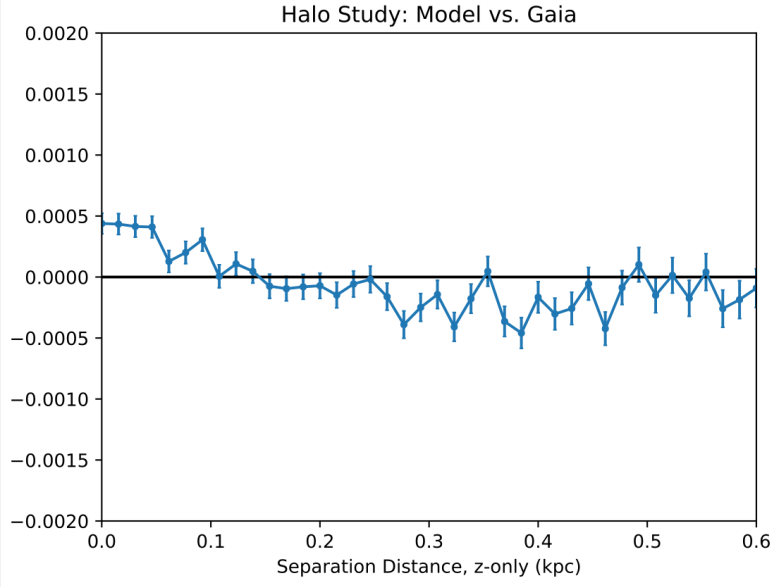

(b)

Figure 8.12: (a) The fit of a normalized, vertical profile of the Gaia data, where as motivated in the text, the particular normalization of the data does not impact the LS Estimator of the 2PCF. A vertical scale height of about 465 pc is found, which is somewhere between the literature values for the thin and thick disk scale heights. (b) The above fit to the vertical distribution of stars is used to generate a mock Galaxy, against which the Gaia data is compared. The result yields small, but potentially significant evidence of clustering at small scales, though slight failures of the fit form may explain this.

Chapter 9 Summary and Further Work

9.1 Contributions to the Field

In this dissertation, we have provided a number of techniques for detecting and assessing the structure and dynamics of the Milky Way, and we have detailed a method of selecting stars as free from scan law effects as is reasonably possible. To wit, we have shown that various asymmetries and different forms of the two-point correlation function can be used to highlight structures and trends in the Galaxy. These tools have been described in detail in this thesis as they may prove useful in analyzing future data sets as well.

Upon application of the techniques above, multiple effects stand out. First, by way of Noether's Theorem, it is clear that axial symmetry is broken in the Milky Way, and that angular momentum must not be perfectly conserved, indicating that outside forces are acting on the nearby region of the Milky Way. Indeed, the Magellanic Clouds are shown to exert significant torques about the Galaxy's z-axis, and the picture of an LMC-induced deformation of the Milky Way halo (Erkal et al., 2019) matches the observed axial asymmetry well, suggesting a Magellanic origin for the Galactic warp (Weinberg and Blitz, 2006).

Moreover, we have applied the Galactic dynamics theorems of An, Evans, and Sanders (2017) to the Galaxy and have found that axial symmetry breaking in the North only minus the South only data sets is much larger in magnitude than that of the aggregate data, speaking to non-steady-state effects. In this instance, the theorem of An, Evans, and Sanders (2017) has admittedly been applied in an approximate manner, as the theorem truly states that an axisymmetric system in steady state is North-South reflection symmetric, and it has been detailed previously that the Galaxy does not quite possess perfect axisymmetry. Further, the theorem of An, Evans, and Sanders requires an isolated system, which in light of the analysis above is not quite true either. However, given the grossly larger N/S differences compared to the relatively smaller axial asymmetry, we think this still points toward non-steady-state behavior.

Next, we have shown how the axial asymmetry techniques outlined above can be used to uncover a sign flip in the axial asymmetry of stars closer to the Galactic center. Upon further investigation, the sense of the sign change in the axial asymmetry matches that of an OLR, offering a new way of determining the OLR resonant radius. By zeroing in on the sign flip's location, we have found that $R_{\rm OLR} = (0.96 \pm 0.03) R_0$, where R_0 is the Galactocentric in-plane radial coordinate of the Sun. Using the Sun-GC distance of Abuter et al. (2018), this corresponds to $R_{\rm OLR} = 7.85 \pm 0.25$ kpc. However, our analysis is limited to about 2 kpc in R, and thus other sign flips may also be found, where the precise sense of the sign flip could hold insights into the nature of any resonances.

Also of interest is an abrupt change in the vertical structure near the OLR. Indeed, Trick et al. (2021) find something very similar near one of their OLR candidates.

While as yet unclear, this phenomenon may be due to some kind of historical asymmetry in the bar region itself. Bar buckling, for example, is thought to cause stellar bars to bend out of plane in an oscillatory manner (see, e.g. Collier, 2020) and the buckling event may even recur (Martinez-Valpuesta, Shlosman, and Heller, 2006). Other instabilities or resonant interactions may also cause similar vertical bending of the bar (Pfenniger and Friedli, 1991; Combes et al., 1990). Vertical resonances of the bar are known to exist (e.g. Quillen et al., 2014) as well, and Combes et al. (1990) find that the Inner Lindblad Resonance has epicyclic frequencies for horizontal and vertical motions that are, very interestingly, the same. It is currently unknown if this is also true for the OLR.

Recent findings make the study of a potential buckling event even more timely. While vertical waves in the outer disk (Widrow et al., 2012) have sometimes been attributed to the Sagittarius dwarf interacting with our Galaxy (e.g. Gómez et al., 2012b), Bennett, Bovy, and Hunt (2021) have suggested that Sagittarius alone is not sufficient to explain the vertical waves. Khoperskov et al. (2019b), on the other hand, find that bar buckling might be able to explain some vertical structure near the solar circle. As such, it is unclear if the vertical structure near our OLR candidate is coincidentally due to the Sagittarius impact, evidence of a vertical resonance, or perhaps speaks to some as yet undiscovered connection between bar buckling and the OLR. This topic is ripe for exploration, and a couple potential investigations are mentioned later.

With the resonant radius of the OLR in hand, we also compute the pattern speed of the Galactic bar via the rotation curve of Eilers et al. (2019) and the Sun-Galactic Center distance of Abuter et al. (2018). By calculating the pattern speed in this way, we have effectively avoided any need to observe the dusty and dense Galactic center region directly, and have only assumed that the resonance is an $m = 2$ OLR due to the classical orbital alignment flip (Contopoulos and Papayannopoulos, 1980), as opposed to any higher order resonance. It is unclear exactly how higher order resonances would manifest themselves in the axial asymmetry data available for study, but any change of the assumed m-value for the resonant feature we observe would result in lower estimates for the pattern speed. As it stands, the pattern speed we have inferred from the sign flip in the asymmetry and by making an $m = 2$ assumption is $\Omega_{\rm p} = 49.3 \pm 2.2$ km s^{-1} kpc^{-1}.

It is worth reiterating here that the pattern speed determinations in the literature form a very wide assortment of values (Bland-Hawthorn and Gerhard, 2016), and ours falls on the faster end. However, Hilmi et al. (2020) suggests an upward revisions of the bar's pattern speed found by Sanders, Smith, and Evans (2019) and Bovy et al. (2019), and that direct observations of the bar's pattern speed may be subject to time-dependent effects which cause fluctuations in bar observables. Such a finding brings the low-end of pattern speed assessments into better agreement with our result.

From our determination of the Galactic bar's pattern speed and the rotation curve of Eilers et al. (2019), we were able to back out the resonant radius for the Co-rotation Resonance, though the radius we find is just on the edge of the rotation

curve approximation given by Eilers et al.[1]. Namely, we find that $R_{\rm CR} = (0.58 \pm 0.04)R_0 = 4.76 \pm 0.27$ kpc, placing it within 1-σ of the bar half-length measurements of $\ell_{\rm bar} = 5.0 \pm 0.2$ kpc by Wegg, Gerhard, and Portail (2015). While a weak bar should possess a CR radius beyond the physical extent of the bar, we note that there exists a possible explanation for this slight tension. Indeed, Eilers et al. (2019) and a preceding paper by Hogg, Eilers, and Rix (2019) employ a Jeans equation analysis in order to arrive at their rotation curve, and assume both axisymmetry and that the Galaxy is in steady state. If the failures of axisymmetry and non-steady-state effects are taken into consideration, the rotation curve is shifted slightly faster, resulting in our estimate of the Co-rotation Resonant radius moving outward (Hinkel, Gardner, and Yanny, 2020a). Fluctuations of Galactic bar parameters, perhaps due to disconnecting and re-connecting to nearby spiral arms or a slowing of the bar (Weinberg, 1985), could be the cause of the non steady state effects, as suggested by Hilmi et al. (2020).

Finally, this dissertation has demonstrated the power of the Two-Point Correlation Function (2PCF) with its full, vector arguments to highlight structures and structural differences throughout the Milky Way. Included in this is a critical development of the data-data 2PCF method to compare various Gaia regions against one another. This appears to be a novel way to explore the vertical waves in the Galaxy, e.g., and this method exploits the various symmetries of our Galaxy.

With the Two-Point Correlation Function analysis above, we have found that the vertical waves in our Galaxy vary significantly across R and ϕ. Interestingly, we have found that the vertical waves vary most markedly in form at high $|z|$ via a Gaia-Gaia 2PCF analysis. Furthermore, non-zero correlations are found not only in the z direction, but also in x, and y. Upon comparison with various toy models, the particular correlation profiles found in the x and y directions roughly match that of differences in scale height, which like the vertical waves, seems to vary across the plane.

Altogether, this dissertation has demonstrated the power of examining symmetries to uncover trends and structures beyond the current models used to describe the Galaxy. Throughout this document, we have either explicitly calculated the degree to which expected symmetries are broken via the asymmetry observable, computed the asymmetry profile to examine how a symmetry is broken along some coordinate direction, or have exploited expected symmetries via a Gaia-Gaia 2PCF analysis to uncover structural differences throughout the Galaxy. As shown in the previous chapters and reiterated here, these methods have resulted in insights regarding the very interior region of our Galaxy to the furthest reaches of the Dark Matter halo.

9.2 Future Work

In light of the ability of the asymmetry observable outlined above to discriminate between various models for the geometry of the Galactic halo, it would be interesting

[1] With the slight update to the Sun-GC distance (Abuter et al., 2019), this tension is lessened somewhat.

to see if the results of Erkal et al. (2019) could be modified slightly to find the model which best matches the observed axial asymmetry and the Orphan Stream data. It would also be informative to test if triaxial models in the literature could better explain the observed asymmetries, as the prolate and oblate models of Erkal et al. (2019) arbitrarily assume that two axes of the Galactic halo share a scale length, perhaps out of convenience. A two-component halo model like that suggested by Norris (1994) and advanced by Beers et al. (2012) could also be used, and might better unite the ideas of Searle and Zinn (1978) and Eggen, Lynden-Bell, and Sandage (1962) for both an in-situ and accreted halo. Such a radially varying halo geometry would also nicely explain the Galactic warp (Dekel and Shlosman, 1983), especially if the large radius behavior tends towards a prolate geometry (Ideta et al., 2000), though Conroy et al. (2021) suggest a much more complicated shape. Nonetheless, Helmi (2020), Di Matteo et al. (2019), and Haywood et al. (2018) suggest that the two-component halo model is unlikely and may just be the "tail" of the thick disk distribution.

While Gaia DR2 did not have sufficient data for a full 6D phase space analysis with the 2PCF, it is possible that DR3 or later releases could offer an opportunity to examine structure via the 2PCF not just in spatial separations or just in velocity space like that of Helmi and Tim de Zeeuw (2000), but in full, 6-D phase-space as a combined "phase-space-separation" metric. In this case, some factor with units of time would be applied to make the units make physical sense, and we envision changing this particular factor would be akin to examining the change over time in Galactic structure. Of course, this would only be valid for smaller steps in time (i.e. linearized) without prior knowledge of the Galaxy's potential. Moreover, our volume of study is finite, and moving forward or backward in time by too large a step could result in completeness issues. Nonetheless, very small steps could potentially give a sense of whether or not known structures are growing or dissipating.

In a similar vein, a larger quantity of 6D phase space data could help to determine why the vertical structure near our Outer Lindblad Resonance radius changes so abruptly with radius, and why the change seems more marked in the North. Indeed, quite a few questions remain regarding this strange feature in the Galactic disk. Can the observed vertical structure "flip" near our OLR candidate (Fig. 7.2) be explained by some asymmetry in the bar itself, perhaps averaged over some time? Buckling of the Galactic bar could offer a potential answer here (see, e.g., Figure 5 of Łokas, 2019), and it would be interesting to identify the stars participating in a resonance of the Galactic bar and see if any radial and vertical couplings could match models of bar buckling in the Milky Way.

Intriguingly, bar buckling appears to hold some sway over the halo through the exchange of angular momentum near resonances (Athanassoula, 2003; Martinez-Valpuesta, Shlosman, and Heller, 2006), so perhaps there is more to uncover near the OLR. Moreover, marginal evidence exists for an asymmetry in the Galactic Center Excess (GCE) (Leane and Slatyer, 2020), which may stem from dark matter (Leane and Slatyer, 2019). It would be interesting to study if some sort of bar buckling remnant effect could exist in the inner dark halo, giving rise to the GCE, or if the tilted triaxial nature of the halo could, along with a bar buckling event, produce

such an asymmetry in the inner dark halo.

On the other hand, the North-South effect in the resonant region we detect could conceivably be due to a vertical resonance, in which case a full 6D phase space analysis of the region along with an assumed potential could help us understand if a vertical resonance is roughly co-located at the OLR radius. With a model of the Galactic potential and the velocities and positions of a large number of stars, orbits could be computed in order to determine if model resonant orbits are indeed consistent with the observed phase-space data. While Bate et al. (2002) find that the OLR and vertical resonance are co-located for a Keplerian disk, which is obviously not the case for a radially distributed mass profile like that of the Milky Way, it is nonetheless interesting (and interesting in any event) to see if the resonances might be close to one another by repeating the sign flip analysis of Hinkel, Gardner, and Yanny (2020a) for the North and South hemispheres separately. A slightly different sign-flip location for the vertical structure is certainly possible.

One particular outcome of the 2PCF studies in chapter 8 is a new illustration of the richness of vertical wave structure – the waves vary substantially in R and ϕ. Along with the notion of a warped Milky Way disk[2] (Kerr, 1957; Burke, 1957; Djorgovski and Sosin, 1989; Skowron et al., 2019; Chen et al., 2019b), it is natural to wonder if separation of the various effects might reveal more about our Galaxy's dynamics. Indeed, if one were to correct for the vertical asymmetry[3], perhaps as determined via Chebyshev fits, one might be able to glimpse a clearer picture of the local warping of the disk, though distinguishing between the z-offset and the odd terms in the expansion may prove impossible. To wit, by accounting for the vertical waves, one might be able to measure warping of the disk in the very same region where we have many millions of well-measured stars to exploit. However, complicated corrugation patterns (Bland-Hawthorn and Tepper-Garcıa, 2021) or vertical waves that change substantially across the footprint of the analysis could present problems here.

Focusing only on the solar neighborhood could present problems for low-m modes of warping, given that any local analysis would only sample a small region of the full 360° of ϕ, where low-m modes with $m > 1$ might not be easily discernible. However, it is possible that the statistical strength of the Gaia database could nonetheless help to discover or set limits on various $m > 1$ modes found in HI gas (e.g. Levine, Blitz, and Heiles, 2006) and not (yet) in stars as we propose here. Such a study would complement the low-statistics but large volume warping studies of Chen et al. (2019b) and Skowron et al. (2019).

In practice, a quantitative analysis of the local warping of the disk could be effected in the following manner. First, the Gaia data is divided into bins in Galactocentric azimuth, ϕ. Second, each vertical profile, $n(z)$, is fit via Chebyshev polynomials. By keeping only the even terms of the fit form, the asymmetry is effectively discarded,

[2]Warping of the disk has been observed in both gas (Kerr, 1957; Burke, 1957) and stars (Djorgovski and Sosin, 1989; Skowron et al., 2019; Chen et al., 2019b), and the precise orientations found by these papers disagree slightly.

[3]Bennett and Bovy (2018) suggested accounting for the local vertical asymmetry to better measure $z_\odot$, and this warping analysis would be somewhat similar to that effort. However, disentangling this effect and the $z_\odot$ shift remains subject to systematic uncertainties.

allowing for a corrected assessment of the mid-plane in each azimuthal bin. By examining the height of the mid-plane, $\bar{z}$ in solarcentric coordinates, relative to that near the Sun for each bin, the following fit form (Binney and Tremaine, 2008; Levine et al., 2008) may be realized for a given annulus in R:

$$\bar{z}(R,\phi) = A_0(R) + \sum_{m=1}^{\infty} A_m(R)\cos(m(\phi - \phi_m)). \tag{9.1}$$

Here, m is the order of the particular mode of warping, ϕ_m is the relative orientation of that mode, and A_m is the amplitude of the mode. For long-lived warps, presumably only the amplitude will depend on R.

Ultimately, the sheer volume of data available to the astronomy and astrophysics community promises untold opportunities for discovery. In this dissertation, we have made the case for examinations of Galactic symmetries, near-symmetries, and symmetry breaking as a means to uncover substructure and trends throughout our Galaxy, and we have offered concrete ideas for the continuation of these studies. Rooted in fundamental physics, demonstrated throughout nuclear and particle physics (and now astrophysics), and fueled by the ever growing repository of astrophysical data, we suspect that these tools will prove useful in analyzing the Milky Way for years to come.

Appendix A: Queries of the Gaia Database and Formatting of Data

Data from the European Space Agency's Gaia Space Telescope is used in this dissertation. Specifically, the second data release (Gaia DR2) is employed, and is obtained via Astronomical Data Query Language (ADQL) queries from `https://gea.esac.esa.int/archive/`. Due to limitations on query size and processing time, the data set we use is constructed from a series of smaller queries.

In practice, authenticated users of the Gaia database may query an unlimited number of stars at once, but time-out limits of 2 hours may limit complicated queries, especially those with a large number of stars. Additionally, the database handles queries with indexed columns much more quickly than queries with complex calculations involved, and this influenced the particular query strategy we chose. Finally, "where" statements in the queries are ordered to try to optimize the speed of the queries.

Because observational data in the database is tabulated in terms of (solarcentric) Galactic longitude, l, and Galactic latitude, b, while our analysis is in Galactocentric cylindrical coordinates, e.g., cuts on R, ϕ, and z are made after queries of the database in order to avoid query time-out. Moreover, any cuts on non-indexed columns are avoided where possible in favor of later processing, and unavoidable query conditions using non-indexed columns are placed toward the end of the query in order to optimize its run time. By querying a larger volume of space than needed, we are ultimately able to explore the completeness of the data in multiple parameter spaces in post-query investigations, and settle on a set of cuts after the completeness is analyzed.

To break up the duration of the multiple queries, we run our queries in four "quadrants:" $|b| > 40°$ or $30° < |b| < 40°$, and $|l - 180°| < 110°$ or $|l - 180°| > 110°$. Query results are downloaded as comma-separated files and appended into one file after removal of column headers. Further pre-processing is done to change the delimiter to a space so that existing C++ code could form a Root file (Antcheva et al., 2009) for quicker analysis. All parameter-space explorations outlined in chapter 5 and chapter 6 are done via Root.

It is also useful to mention a couple peculiarities of the Gaia database here. First, since Gaia only allows a 2D sky-projection solution or a full 5D astrometric solution, a star must have all 5 astrometric parameters available in the database to be useful to our analyses. A column in the database encodes this information in base-ten, but is more transparent as a binary number – "astrometric_params_solved" must be 31 (11111 in binary) if all 5 astrometric quantities are available.

Further, ADQL requires the user to optimize any query in order to reduce run times. Most importantly, using indexed (i.e. readily available) columns in the database is always faster than calculating new columns. Moreover, ordering various conditions to cull the data before doing any complex, non-indexed calculations saves large amounts of time, as will ordering conditions which greatly reduce the number of rows first, while keeping less restrictive queries for later in the code.

A sample query is included below for archival purposes, with ADQL keywords

in capital letters, and database-specific variables in lower-case. Please note, more columns were queried in our original analysis, but as they went unused they have been omitted here for clarity. All units of measurement used by the database can be found in the documentation at gea.esac.esa.int/archive/documentation/GDR2/index.html or in the data model at gea.esac.esa.int/archive/documentation/GDR2/Gaia_archive/chap_datamodel/sec_dm_main_tables/ssec_dm_gaia_source.html:

```
SELECT gaiadr2.gaia_source.parallax,
gaiadr2.gaia_source.parallax_error,  gaiadr2.gaia_source.l,
gaiadr2.gaia_source.b,  gaiadr2.gaia_source.phot_g_mean_mag,
gaiadr2.gaia_source.bp_rp,  gaiadr2.gaia_source.pmra,
gaiadr2.gaia_source.pmra_error,  gaiadr2.gaia_source.pmdec,
gaiadr2.gaia_source.pmdec_error
FROM gaiadr2.gaia_source
WHERE (ABS (gaiadr2.gaia_source.b) > 30 AND
gaiadr2.gaia_source.astrometric_params_solved = 31
AND gaiadr2.gaia_source.parallax > -0.07 AND
1/gaia_source.parallax < 3.10)
```

In this example, the data is queried so that the parallax is positive after a parallax offset shift is applied (e.g. Stassun and Torres, 2018), and is queried for a volume that excludes stars beyond the cuts motivated in earlier chapters. Further cuts are more efficiently applied via Root (e.g.) after the query.

Appendix B: Miscellaneous Observational Considerations

Despite boasting a whopping 1.7 billion total stars in its DR2 catalogue, the Gaia space telescope's data is, like all data, subject to various incompletenesses and biases. While much of the details have been outlined in chapter 5 and chapter 6, it is worth noting a few further details for the sake of completeness. These details underlie and motivate some of the choices earlier in the document.

First, it is important to note that data with full 6D phase space information makes up less than 1% of the database, and thus statistical strength is compromised if one insists on only analyzing stars with 6D data. Moreover, the Radial Velocity (RV) data set (Cropper et al., 2018) is subject to directional biases and completeness issues due to the comparative difficulty of collecting spectra, as depicted in figures 9 and 10 of Rybizki et al. (2021). Moreover, sources with G-band[4] magnitudes fainter than about 14th magnitude do not have RV data (Sartoretti et al., 2018; Rybizki et al., 2021). As such, we opt for analyses based on 5D phase space data only, as position data is all that is needed.

Second, another implicit consideration for our analyses is that we have chosen dimmer, redder stars in an effort to avoid very young, hot stars. As a general principle, young, high mass stars do not wander far from their birth clouds, and thus clustering or asymmetries in these stars may speak more to star formation trends instead of some galactoseismological effect. By avoiding the bluest, brightest stars as well as the regions with sizable mass in gas and dust, we are implicitly focusing on stars which are very likely to have made many trips around the Galactic center and thus have sampled a long history of interactions with and internal dynamics of our Galaxy.

Another consideration is the parallax zero-point offset. While our particular choice of parallax zero-point offset is specified in earlier chapters, it is worth explicitly mentioning why the particular choice of zero-point does not affect our results. First, the various parallax offsets in the literature (Zinn et al., 2019; Stassun and Torres, 2018; Lindegren et al., 2018) are no more than about 0.08 mas in magnitude, and any star which is shifted into positive territory via the application of this offset is at minimum distance $d \approx {}^{1}/_{0.08\text{ mas}} \approx 12$ kpc away, and well outside our sample volume. Moreover, there is no evidence for substantial variations of the zero-point offset with direction of observation[5] (Vasiliev, 2019), so any global shift of about 0.07 mas should not affect asymmetry measurements or clustering.

Finally, our method of excising the Large and Small Magellanic Clouds (LMC and SMC respectively) is motivated by a desire to maintain an ability to test axial and reflection symmetries, but we do not address the other methods in the literature for identifying (and thus for our purposes, excising) LMC and SMC stars in our earlier chapters. As a particular example, Helmi et al. (2018a) suggest identifying LMC

[4]Note that Gaia uses both a G-band photometry as well as a G_{RVS} photometer, and these are not identical (see, e.g. C. Jordi, 2012)

[5]Vasiliev (2019) find some covariance relation between parallax offsets for nearby stars, but the effect seems to be extremely small.

stars in part through their clustering in proper motion space. However, as is the case for all dense fields, astrometric solutions in the direction of the LMC and SMC can be unreliable due to point source identification issues, possibly resulting in incorrect distance assessments and proper motion measurements. In fact, foreground stars and LMC stars, e.g., which may be some fifty kiloparsecs distant from one another could be nearly coincident on the sky, causing the effect to "bleed" into the region closer to the Sun. While this problem is significant enough for us to not employ proper motion LMC/SMC cuts for our sensitive studies of symmetry, it should be noted as well that proper motions are a solarcentric observable, and cuts on these particular quantities may bias the spatial distribution of stars in unexpected ways.

Appendix C: Further Study of Systematics

In an effort to expand upon the systematics associated with the axial asymmetry analysis in Chapters 5 and 6, a more detailed analysis is presented here. Namely, we outline the asymmetry systematics for null value entries and negative parallaxes in the Gaia database, dense field incompleteness in our Gaia sample, scan-law incompletenesses, and a couple of other possible sources. While immense care has been taken to avoid many of the effects listed here, we nonetheless quantify their potential impact. The total systematic asymmetry from the quantifiable sources below is $|\mathcal{A}_{\rm sys}| \approx 0.0009$.

Null Entries and Negative Parallaxes

By their very nature, stars with null or negative parallaxes cannot be described by a 3-D position vector. Because the parallax does not exist or is otherwise unphysical (i.e. negative), the distance to that star cannot be computed via astrometry, and thus we are left with only the 2-D position on the sky. As a result, we cannot say for certain if a star with negative or null parallax would be in our sample geometry or not. Nonetheless, stars with null parallaxes are generally very far away (Michalik et al., 2015), and if stars have negative parallaxes due to a small, incorrect offset, their true parallax value would be extremely small, and thus they would also be extremely far away. It is exceedingly likely that the systematics for null and negative parallaxes explored here are gross overestimates.

Still, out of general principle, we share more details here regarding how we arrived at the systematics in Chapter 6, which is originally published as Hinkel, Gardner, and Yanny (2020b). In this chapter, a statistical query of the first several million, randomly drawn stars in the Gaia database is performed considering all stars with $|b| > 30^\circ$ and $14 < G < 18$ mag, as all stars in the database possess at least a 2D astrometric solution (l and b) as well as G-band photometry. The resulting estimate of the systematic is given as $|\mathcal{A}_{\rm null\ \varpi\ \&\ color}| \approx 0.0017$. Here, we explore this systematic in more detail by repeating the query for the entire 1.7 billion star database.

In this deeper exploration, the Gaia database is queried for a count of all stars with one of the following conditions met: the star has a null parallax, negative parallax (after shift of 0.07 mas), or null $G_{\rm BP} - G_{\rm RP}$ color. The query is done for $0^\circ < l < 180^\circ$ and $180^\circ < l < 360^\circ$ in order to assess how many stars on the Right (R) and Left (L) respectively satisfied the conditions. A separate pair of queries is performed to determine the total number of stars in the $|b| > 30^\circ$ and $14 < G < 18$ mag window, without regard for the three conditions above.

The queries above resulted in $N_{\rm L,missed} = 259{,}317$ stars on the Left which satisfy one of the three criteria above, out of a possible $N_{\rm L,total} = 10{,}791{,}366$ stars. For the Right, the numbers are $N_{\rm R,missed} = 219{,}731$ and $N_{\rm R,total} = 10{,}640{,}362$, respectively. The systematic asymmetry from nulls or negative parallaxes is then computed via Eq. 9.2, which quantifies the contribution of the missed stars to a total asymmetry.

$$\mathcal{A}_{\text{null } \varpi \text{ \& color}} = \frac{N_{\text{L,missed}} - N_{\text{R,missed}}}{N_{\text{L,total}} + N_{\text{R,total}}} \tag{9.2}$$

This deeper dive into the null entry and negative parallax systematic error results in $|\mathcal{A}_{\text{null } \varpi \text{ \& color}}| \approx 0.0018$, differing from the previous estimate derived from a small sample by what amounts to a rounding error in the last digit. This does not change any conclusions from the above chapters. Regardless, as motivated in Chapter 6, the Gaia data is nearly 100% complete for the region we study, as we avoid dense fields (Arenou et al., 2018). As such, an exaggerated, worst case scenario of 99% completeness would then imply that the systematic uncertainty for null entries and negative parallaxes is then around $|\mathcal{A}_{\text{null } \varpi \text{ \& color}}| \approx 2 \times 10^{-4}$. This is much smaller than the asymmetries we measure.

Although certainly small, the above systematic is perhaps frustratingly resigned to estimation only. To wit, there is no way to say for certain that a star with no parallax, e.g., falls within our sample or not, as it lacks full, 3-D information. A potential future exploration of these stars with photometrically-derived distances might help to more concretely prove how few of these stars infiltrate our sample, but this is not needed at this time.

Dense Field Incompleteness

As covered previously, the Gaia telescope has trouble observing dense fields, and spurious astrometric solutions, missing stars, and duplicated sources can occur in these regions. Indeed, Arenou et al. (2018) detail how complete the Gaia data is (as compared to the Hubble Space Telescope) given a source density on the sky and the G-band magnitude of stars, and find that ultra-dense fields can result in significant incompletenesses, especially in fainter stars. Although we have cut away the LMC and SMC sight-lines and the lower latitudes close to the mid-plane, there may still be some localized, dense fields which affect some parts of our sample.

While most of our sample falls within a line of sight with low source densities, small "pin-pricks" of denser fields will show up in the data, generally at lower latitudes. We explore a worst-case scenario by studying stars near $b = 30°$ near the Galactic Center – the densest region in our volume of study. An example of these denser fields is shown in Fig. 1.

As a way of estimating a possible false asymmetry from missing stars lost to the dense fields, we first estimate the true source density in stars per square degree for the small, dense regions we find. To do so, we extrapolate the measured source densities in our subset of the data to that of the full Gaia data set and find around 4×10^5 stars per square degree[6]. This ultra-conservative estimation ignores the fact that most stars lie below $|b| = 30°$ and thus the true source density for the bright yellow points in Fig. 1 is much smaller.

[6]That is, our data set is a subset of the full Gaia database, containing a fraction f of the total number of stars. We conservatively extrapolate our source densities to that of the full database by simply dividing the source densities by f. As our sample omits the $|b| < 30°$ region, this is a gross overestimate.

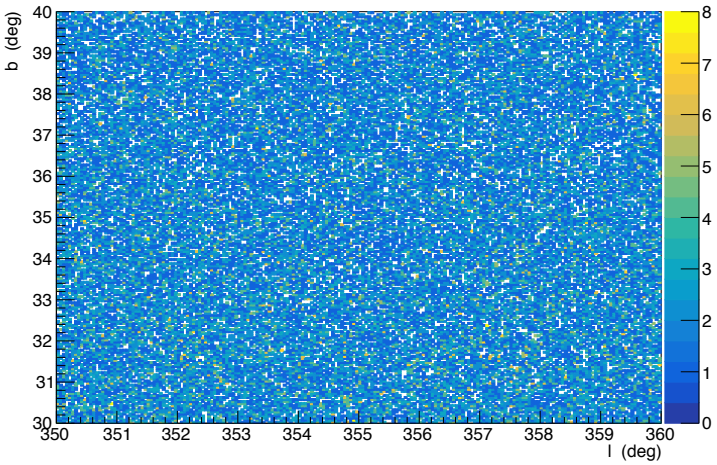

Figure 1: A zoomed-in view of the data for $30° < b < 40°$ and $350° < l < 360°$, after the cuts of Chapters 5 and 6 have been applied. Please note that the view is zoomed-in to such an extent that, after cuts, there are small regions with no stars. This is not an indication of incompleteness, but is due to the fact that the data is binned very finely in this view. In a small number of bins, the stars can be slightly denser than average, and we study these to ensure that any incompletenesses due to dense field issues do not contribute significantly to the asymmetries we measure.

Nonetheless, we use this overestimate of the source density and read off the relative incompleteness factor from Arenou et al. (2018) for our magnitude window. With this in hand, we again conservatively estimate a worst-case completeness of 90% in these regions, and estimate the number of stars which could be missing from the analysis. By counting up these potentially missing stars, multiplying by the number of over-dense regions, and doing this for the Left and the Right in the worst case, $30° < b < 40°$ scenario, we find $|\mathcal{A}_{\rm densefields}| \approx 0.000013$.

Gaia Scan-Law Artefacts

By virtue of its precise orbital and rotational parameters, the Gaia space telescope scans the sky in a manner that does not lend itself to uniformity. As discussed numerous times throughout this dissertation, great care has been taken to avoid explicitly cutting on any parameters which depend on the number of observations of a star, and such a method seemed to effectively avoid artefacts from the Gaia scan-law. Nonetheless, we mention the possibility for imperceptible artefacts which escape our methods, and we outline here how our estimation of this systematic error came to be.

First, noting Fig. 6.2(a), we know the regions of the sky where the scan law surfaces upon cutting on relative parallax error. The idea is then to zoom into one of these regions in the data set where there are no cuts on relative parallax errors, and

see if an asymmetry surfaces. Of course, the asymmetry found via this method could be from real Galactic structure, but given the coincidence with the streaky pattern, we conservatively assume the entire asymmetry is due to a scan-law systematic error. In doing so, we find a very localized asymmetry of something like 0.007, but this is for a very small region of the Galaxy. In fact, since the scan-law effects only appear to afflict around 10% of the sky in Fig. 6.2(a), we take the systematic to be a factor of ten lower – $|\mathcal{A}_{\text{scan}}| \approx 0.0007$. Like the previous estimates, this is a conservative overestimate.

Unresolved Binaries

Although unexplored in Chapters 5 and 6, another possible systematic asymmetry may occur due to the Gaia space telescope's ability to resolve binary star systems on the left and right of the $\phi = 180°$ ray. If Gaia has imaged certain parts of the sky more than others, it is possible that the telescope has better resolved binaries in some regions of the sky than others. We explore this possibility here.

As noted by Belokurov et al. (2020), unresolved binaries tend to occur at bright magnitudes in Gaia data, and only a few percent of dimmer stars are unresolved binaries. Moreover, Belokurov et al. find that close-up binary pairs are much more likely to be resolved, so our close-up, dim sample likely has very few unresolved binaries to worry about, not to mention our sample is out of plane. While it is probably comforting that the number of unresolved binaries in our sample is quite small, it is nonetheless difficult to identify the interlopers.

Note that eclipsing, unresolved binaries can potentially be identified by examining the photometric variability flag provided in the Gaia database (Holl et al., 2018), and then assume that the orientation of binary stars are purely random. However, all kinds of variable stars exist, and not all of them are eclipsing binaries. Determining which sources in the Gaia database are truly unresolved binaries and not Cepheids, RR Lyrae, Delta Scuti stars, etc. (Brown et al., 2018) is a difficult problem. Regardless, this photometry variation does not capture any binaries beyond those which happen to be eclipsing binaries.

Instead, Belokurov et al. (2020) suggest using the fact that the astrometric solution for unresolved binaries are subject to larger errors due to the movement of the photo-center of a binary system with time. Specifically, the Re-normalized, Unweighted Error (RUWE) tends to be higher for unresolved binaries, and (to a lesser extent) the Astrometric Excess Noise (AEN) is higher as well. While this could help identify unresolved binaries, there are other situations which could cause higher than average AEN, including observations in dense fields (Lindegren et al., 2018).

Alas, there appears to be no foolproof way of assessing this systematic short of developing an entirely new way of identifying unresolved binaries. At the very least, we have performed a basic query of the Gaia database and all of the variable stars on the left and right for our magnitude and latitude windows were counted (l cuts were also applied to excise the LMC and SMC). This results in about 18,000 stars on each side out of tens of millions (or $|\mathcal{A}_{\text{variable}}| \approx 0.00006$) – not nearly enough to explain the asymmetry we find. These numbers absorb true variable stars, and so the number

of unresolved binaries is smaller still. While the photometric variability criteria only captures eclipsing binaries, there is no compelling reason why other, non-eclipsing binaries would be distributed differently. Unfortunately, the second data release does not identify all variable stars (Brown et al., 2018), so this estimate must remain rather rudimentary and inexact. Further exploration of the spatial distribution of unresolved binaries and the development of a more robust method of identifying them is left to a future work.

Other Objects

In addition to stars, asteroids (Spoto et al., 2018, e.g.) and quasars (Heintz et al., 2018, e.g.) actually make their way into the Gaia database. As solar system objects are extremely close by, the former are excised by our requirement that $|z| > 0.2$ kpc. The latter are also excised by the R, ϕ, and z cuts, which effectively limit the data to $\sim$3 kpc distance at most, easily avoiding these extremely distant objects. We therefore assume these objects do not contribute at all to any systematic errors in our analysis.

Appendix D: Code and Data Repository

In compliance with U.S. Department of Energy rules and out of general, scientific principle, all relevant data and code is available for examination in an online repository. All data used herein may also be queried from the freely available Gaia database, and the particular subset of the data we have used is outline in Chapters 5 and 6. The purpose of this data sharing is to enable validation of our results and to better facilitate future work building upon this dissertation. The repository can be found at: doi.org/10.17632/hx9tmcjtxx.1. Data and code can also be shared by request.

Bibliography

Ablimit, Iminhaji et al. (2020). "The Rotation Curve, Mass Distribution, and Dark Matter Content of the Milky Way from Classical Cepheids". In: *The Astrophysical Journal Letters* 895.1, p. L12.

Abuter, R et al. (2018). "Detection of the gravitational redshift in the orbit of the star S2 near the Galactic centre massive black hole". In: *Astronomy & Astrophysics* 615, p. L15.

Abuter, R et al. (2019). "A geometric distance measurement to the Galactic center black hole with 0.3% uncertainty". In: *Astronomy & Astrophysics* 625, p. L10.

Aguerri, JAL, JE Beckman, and M Prieto (1998). "Bar strengths, bar lengths, and corotation radii, derived photometrically for 10 barred galaxies". In: *The Astronomical Journal* 116.5, p. 2136.

Ahn, Christopher P et al. (2012). "The ninth data release of the Sloan Digital Sky Survey: first spectroscopic data from the SDSS-III Baryon Oscillation Spectroscopic Survey". In: *The Astrophysical Journal Supplement Series* 203.2, p. 21.

Alard, C (2000). "Flaring and warping of the milky way disk: not only in the gas". In: *arXiv preprint astro-ph/0007013*.

An, Deokkeun (2019). "Asymmetric Mean Metallicity Distribution of the Milky Way's Disk". In: *The Astrophysical Journal Letters* 878.2, p. L31.

An, J, NW Evans, and JL Sanders (2017). "Reflection symmetries of isolated self-consistent stellar systems". In: *Monthly Notices of the Royal Astronomical Society* 467.2, pp. 1281–1286.

Anders, Friedrich et al. (2019). "Photo-astrometric distances, extinctions, and astrophysical parameters for Gaia DR2 stars brighter than G= 18". In: *Astronomy & Astrophysics* 628, A94.

Antcheva, Ilka et al. (2009). "ROOT—A C++ framework for petabyte data storage, statistical analysis and visualization". In: *Computer Physics Communications* 180.12, pp. 2499–2512.

Antoja, T et al. (2018). "A dynamically young and perturbed Milky Way disk". In: *Nature* 561.7723, p. 360.

Antoja, Teresa et al. (2014). "Constraints on the Galactic bar from the Hercules stream as traced with RAVE across the Galaxy". In: *Astronomy & Astrophysics* 563, A60.

Arenou, F et al. (2018). "Gaia Data Release 2-Catalogue validation". In: *Astronomy & Astrophysics* 616, A17.

Athanassoula, E (2003). "What determines the strength and the slowdown rate of bars?" In: *Monthly Notices of the Royal Astronomical Society* 341.4, pp. 1179–1198.

Bailer-Jones, CAL et al. (2018). "Estimating distance from parallaxes. IV. Distances to 1.33 billion stars in Gaia data release 2". In: *The Astronomical Journal* 156.2, p. 58.

Bailer-Jones, Coryn AL (2015). "Estimating distances from parallaxes". In: *Publications of the Astronomical Society of the Pacific* 127.956, p. 994.

Bailin, Jeremy (2003). "Evidence for coupling between the Sagittarius dwarf galaxy and the Milky Way warp". In: *The Astrophysical Journal Letters* 583.2, p. L79.

Banerjee, Arunima and Chanda J Jog (2011). "Progressively more prolate dark matter halo in the outer Galaxy as traced by flaring HI gas". In: *The Astrophysical Journal Letters* 732.1, p. L8.

Bate, MR et al. (2002). "The excitation, propagation and dissipation of waves in accretion discs: the non-linear axisymmetric case". In: *Monthly Notices of the Royal Astronomical Society* 332.3, pp. 575–600.

Beers, Timothy C et al. (2012). "The case for the dual halo of the Milky Way". In: *The Astrophysical Journal* 746.1, p. 34.

Behroozi, Peter S., Risa H. Wechsler, and Charlie Conroy (June 2013). "The Average Star Formation Histories of Galaxies in Dark Matter Halos from z = 0-8". In: *The Astrophysical Journal* 770.1, 57, p. 57. DOI: 10.1088/0004-637X/770/1/57. arXiv: 1207.6105 [astro-ph.CO].

Bell, Eric F et al. (2008). "The accretion origin of the Milky Way's stellar halo". In: *The Astrophysical Journal* 680.1, p. 295.

Belokurov, V et al. (2018). "Co-formation of the disc and the stellar halo". In: *Monthly Notices of the Royal Astronomical Society* 478.1, pp. 611–619.

Belokurov, Vasily et al. (2020). "Unresolved stellar companions with Gaia DR2 astrometry". In: *Monthly Notices of the Royal Astronomical Society* 496.2, pp. 1922–1940.

Bennett, Morgan and Jo Bovy (2018). "Vertical waves in the solar neighbourhood in Gaia DR2". In: *Monthly Notices of the Royal Astronomical Society* 482.1, pp. 1417–1425.

Bennett, Morgan, Jo Bovy, and Jason A. S. Hunt (2021). "Exploring the Sgr-Milky-Way-disc interaction using high resolution N-body simulations". In: arXiv: 2107.08055 [astro-ph.GA].

Bensby, Thomas, Sofia Feltzing, and MS Oey (2014). "Exploring the Milky Way stellar disk-A detailed elemental abundance study of 714 F and G dwarf stars in the solar neighbourhood". In: *Astronomy & Astrophysics* 562, A71.

Binney, J et al. (2014). "Galactic kinematics and dynamics from Radial Velocity Experiment stars". In: *Monthly Notices of the Royal Astronomical Society* 439.2, pp. 1231–1244.

Binney, James (2012). "Actions for axisymmetric potentials". In: *Monthly Notices of the Royal Astronomical Society* 426.2, pp. 1324–1327.

— (2017). "Self-consistent modelling of our Galaxy with Gaia data". In: *Proceedings of the International Astronomical Union* 12.S330, pp. 111–118.

— (2019). "Modelling our Galaxy". In: *arXiv preprint arXiv:1909.02455*.

Binney, James and Tilmann Piffl (2015). "The distribution function of the Galaxy's dark halo". In: *Monthly Notices of the Royal Astronomical Society* 454.4, pp. 3653–3663.

Binney, James and Ralph Schönrich (2018). "The origin of the Gaia phase-plane spiral". In: *Monthly Notices of the Royal Astronomical Society* 481.2, pp. 1501–1506.

Binney, James and Scott Tremaine (2008). *Galactic Dynamics*.

Bland-Hawthorn, Joss and Ortwin Gerhard (Sept. 2016). "The Galaxy in Context: Structural, Kinematic, and Integrated Properties". In: *Annual Review of Astronomy and Astrophysics* 54, pp. 529–596. DOI: 10.1146/annurev-astro-081915-023441. arXiv: 1602.07702 [astro-ph.GA].

Bland-Hawthorn, Joss and Thor Tepper-Garcıa (2021). "Galactic seismology: the evolving 'phase spiral'after the Sagittarius dwarf impact". In: *Monthly Notices of the Royal Astronomical Society* 504.3, pp. 3168–3186.

Blitz, Leo and David N Spergel (1991). "Direct evidence for a bar at the Galactic center". In: *The Astrophysical Journal* 379, pp. 631–638.

Borsato, Nicholas W, Sarah L Martell, and Jeffrey D Simpson (2019). "Identifying Stellar Streams in Gaia DR2 with Data Mining Techniques". In: *arXiv preprint arXiv:1907.02527*.

Bose, Sownak et al. (Oct. 2016). "Substructure and galaxy formation in the Copernicus Complexio warm dark matter simulations". In: *Monthly Notices of the Royal Astronomical Society* 464.4, pp. 4520–4533. ISSN: 0035-8711. DOI: 10.1093/mnras/stw2686. eprint: https://academic.oup.com/mnras/article-pdf/464/4/4520/8313906/stw2686.pdf. URL: https://doi.org/10.1093/mnras/stw2686.

Bovy, Jo (Feb. 2015). "galpy: A python Library for Galactic Dynamics". In: *The Astrophysical Journal Supplement Series* 216.2, 29, p. 29. DOI: 10.1088/0067-0049/216/2/29. arXiv: 1412.3451 [astro-ph.GA].

— (2017). "Galactic rotation in Gaia DR1". In: *Monthly Notices of the Royal Astronomical Society: Letters* 468.1, pp. L63–L67.

Bovy, Jo and Hans-Walter Rix (2013). "A direct dynamical measurement of the Milky Way's disk surface density profile, disk scale length, and dark matter profile at 4 kpc R 9 kpc". In: *The Astrophysical Journal* 779.2, p. 115.

Bovy, Jo et al. (2019). "Life in the fast lane: a direct view of the dynamics, formation, and evolution of the Milky Way's bar". In: *Monthly Notices of the Royal Astronomical Society* 490.4, pp. 4740–4747.

Brown, AGA et al. (2018). "Gaia Data Release 2-Summary of the contents and survey properties". In: *Astronomy & astrophysics* 616, A1.

Buckley, Matthew R and Annika HG Peter (2018). "Gravitational probes of dark matter physics". In: *Physics Reports* 761, pp. 1–60.

Burke, Bernard F (1957). "Systematic distortion of the outer regions of the galaxy." In: *The Astronomical Journal* 62, p. 90.

C. Jordi (May 2012). "Photometric relationships between Gaia photometry and existing photometric systems". Technical Note. GAIA-C5-TN-UB-CJ-041. URL: http://www.rssd.esa.int/doc_fetch.php?id=2760608.

Camargo, Denilso, Charles Bonatto, and Eduardo Bica (2015). "Tracing the Galactic spiral structure with embedded clusters". In: *Monthly Notices of the Royal Astronomical Society* 450.4, pp. 4150–4160.

Carrillo, I et al. (Aug. 2019). "Kinematics with Gaia DR2: The Force of a Dwarf". In: *Monthly Notices of the Royal Astronomical Society*. stz2343. ISSN: 0035-8711. DOI: 10.1093/mnras/stz2343. eprint: http://oup.prod.sis.lan/mnras/advance-article-pdf/doi/10.1093/mnras/stz2343/29211724/stz2343.pdf. URL: https://doi.org/10.1093/mnras/stz2343.

Chakrabarty, Dalia (2007). "Phase space structure in the solar neighbourhood". In: *Astronomy & Astrophysics* 467.1, pp. 145–162.

Chandrasekhar, Subrahmanyan (1943). "Dynamical friction. I. General considerations: the coefficient of dynamical friction". In: *Astrophysical Journal* 97, pp. 255–262.

Chen, BQ et al. (2019a). "The Galactic spiral structure as revealed by O-and early B-type stars". In: *Monthly Notices of the Royal Astronomical Society* 487.1, pp. 1400–1409.

Chen, Xiaodian et al. (2019b). "An intuitive 3D map of the Galactic warp's precession traced by classical Cepheids". In: *Nature Astronomy* 3.4, p. 320.

Chequers, Matthew H, Lawrence M Widrow, and Keir Darling (2018). "Bending waves in the Milky Way's disc from halo substructure". In: *Monthly Notices of the Royal Astronomical Society* 480.3, pp. 4244–4258.

Chiba, Rimpei, Jennifer KS Friske, and Ralph Schönrich (2021). "Resonance sweeping by a decelerating Galactic bar". In: *Monthly Notices of the Royal Astronomical Society* 500.4, pp. 4710–4729.

Clarke, Jonathan and Ortwin Gerhard (2021). "The Pattern Speed of the Milky Way Bar/Bulge from VIRAC & Gaia". In: *arXiv preprint arXiv:2107.10875*.

Collier, Angela (2020). "Violent buckling benefits galactic bars". In: *Monthly Notices of the Royal Astronomical Society* 492.2, pp. 2241–2249.

Combes, F et al. (1990). "Box and peanut shapes generated by stellar bars". In: *Astronomy and Astrophysics* 233, pp. 82–95.

Conroy, Charlie et al. (2021). "All-sky dynamical response of the Galactic halo to the Large Magellanic Cloud". In: *Nature* 592.7855, pp. 534–536.

Contopoulos, George and Th Papayannopoulos (1980). "Orbits in weak and strong bars". In: *Astronomy and Astrophysics* 92, pp. 33–46.

Corbelli, Edvige (2003). "Dark matter and visible baryons in M33". In: *Monthly Notices of the Royal Astronomical Society* 342.1, pp. 199–207.

Cropper, M et al. (2018). "Gaia Data Release 2-Gaia Radial Velocity Spectrometer". In: *Astronomy & Astrophysics* 616, A5.

Cunningham, Emily C et al. (2020). "Quantifying the Stellar Halo's Response to the LMC's Infall with Spherical Harmonics". In: *The Astrophysical Journal* 898.1, p. 4.

D'Onghia, E et al. (2016). "Excitation of coupled stellar motions in the Galactic disk by orbiting satellites". In: *The Astrophysical Journal* 823.1, p. 4.

Darling, Keir and Lawrence M Widrow (2019). "Emergence of the Gaia phase space spirals from bending waves". In: *Monthly Notices of the Royal Astronomical Society* 484.1, pp. 1050–1056.

Deason, Alis J et al. (2020). "The edge of the Galaxy". In: *Monthly Notices of the Royal Astronomical Society* 496.3, pp. 3929–3942.

Deason, Alis J et al. (2021). "The mass of the Milky Way out to 100 kpc using halo stars". In: *Monthly Notices of the Royal Astronomical Society* 501.4, pp. 5964–5972.

Debattista, Victor P, Ortwin Gerhard, and Maartje N Sevenster (2002). "The pattern speed of the OH/IR stars in the Milky Way". In: *Monthly Notices of the Royal Astronomical Society* 334.2, pp. 355–368.

Debattista, Victor P. et al. (Oct. 2013). "What's up in the Milky Way? The orientation of the disc relative to the triaxial halo". In: *Monthly Notices of the Royal Astronomical Society* 434.4, pp. 2971–2981. DOI: 10.1093/mnras/stt1217. arXiv: 1301.2670 [astro-ph.GA].

Dehnen, Walter (1999). "The pattern speed of the Galactic bar". In: *The Astrophysical Journal Letters* 524.1, p. L35.

— (2000). "The effect of the outer Lindblad resonance of the galactic bar on the local stellar velocity distribution". In: *The Astronomical Journal* 119.2, p. 800.

Dekel, Avishai and Izhak Shlosman (1983). "Galactic warps in tilted halos". In: *Symposium-International Astronomical Union*. Vol. 100. Cambridge University Press, pp. 187–188.

Di Matteo, P et al. (2019). "The Milky Way has no in-situ halo other than the heated thick disc-Composition of the stellar halo and age-dating the last significant merger with Gaia DR2 and APOGEE". In: *Astronomy & Astrophysics* 632, A4.

Djorgovski, S and Craig Sosin (1989). "The warp of the Galactic stellar disk detected in IRAS source counts". In: *The Astrophysical Journal* 341, pp. L13–L16.

Drimmel, Ronald and David N Spergel (2001). "Three-dimensional structure of the Milky Way disk: the distribution of stars and dust beyond 0.35 R0". In: *The Astrophysical Journal* 556.1, p. 181.

Dwek, E et al. (1995). "Morphology, near-infrared luminosity, and mass of the Galactic bulge from COBE DIRBE observations". In: *The Astrophysical Journal* 445, pp. 716–730.

Eggen, OJ, D Lynden-Bell, and AR Sandage (1962). "Evidence from the motions of old stars that the Galaxy collapsed." In: *The Astrophysical Journal* 136, p. 748.

Eilers, Anna-Christina et al. (2019). "The circular velocity curve of the Milky Way from 5 to 25 kpc". In: *The Astrophysical Journal* 871.1, p. 120.

Englmaier, Peter and Ortwin Gerhard (1999). "Gas dynamics and large-scale morphology of the Milky Way galaxy". In: *Monthly Notices of the Royal Astronomical Society* 304.3, pp. 512–534.

Erkal, D et al. (2019). "The total mass of the Large Magellanic Cloud from its perturbation on the Orphan stream". In: *Monthly Notices of the Royal Astronomical Society* 487.2, pp. 2685–2700.

Erkal, Denis, Vasily A Belokurov, and Daniel L Parkin (2020). "Equilibrium models of the Milky Way mass are biased high by the LMC". In: *Monthly Notices of the Royal Astronomical Society* 498.4, pp. 5574–5580.

Erkal, Denis et al. (2021). "Detection of the LMC-induced sloshing of the Galactic halo". In: *Monthly Notices of the Royal Astronomical Society* 506.2, pp. 2677–2684.

Evans, N Wyn, Ciaran AJ O'Hare, and Christopher McCabe (2019). "Refinement of the standard halo model for dark matter searches in light of the Gaia Sausage". In: *Physical Review D* 99.2, p. 023012.

Fardal, Mark A et al. (2019). "The course of the Orphan Stream in the Northern Galactic Hemisphere traced with Gaia DR2". In: *Monthly Notices of the Royal Astronomical Society* 486.1, pp. 936–949.

Fattahi, Azadeh et al. (Jan. 2019). "The origin of galactic metal-rich stellar halo components with highly eccentric orbits". In: *Monthly Notices of the Royal Astronomical Society* 484.4, pp. 4471–4483. ISSN: 0035-8711. DOI: 10.1093/mnras/stz159. eprint: https://academic.oup.com/mnras/article-pdf/484/4/4471/27765834/stz159.pdf. URL: https://doi.org/10.1093/mnras/stz159.

Ferguson, Deborah, Susan Gardner, and Brian Yanny (2017). "Milky Way tomography with K and M dwarf stars: The vertical structure of the galactic disk". In: *The Astrophysical Journal* 843.2, p. 141.

Fragkoudi, F et al. (2019). "On the ridges, undulations, and streams in Gaia DR2: linking the topography of phase space to the orbital structure of an N-body bar". In: *Monthly Notices of the Royal Astronomical Society* 488.3, pp. 3324–3339.

Fux, Roger (2001). "Order and chaos in the local disc stellar kinematics induced by the Galactic bar". In: *Astronomy & Astrophysics* 373.2, pp. 511–535.

Gandhi, Suroor S et al. (2021). "Snails Across Scales: Local and Global Phase-Mixing Structures as Probes of the Past and Future Milky Way". In: *arXiv preprint arXiv:2107.03562*.

Garavito-Camargo, Nicolas et al. (2019). "Hunting for the Dark Matter Wake Induced by the Large Magellanic Cloud". In: *arXiv preprint arXiv:1902.05089*.

Gardner, Susan, Austin Hinkel, and Brian Yanny (2020). "Applying Noether's theorem to matter in the Milky Way: evidence for external perturbations and non-steady-state effects from Gaia Data Release 2". In: *The Astrophysical Journal* 890.2, p. 110.

Gardner, Susan, Samuel D McDermott, and Brian Yanny (2021). "The Milky Way, coming into focus: Precision astrometry probes its evolution and its dark matter". In: *Progress in Particle and Nuclear Physics*, p. 103904.

Gerhard, Ortwin and Christopher Wegg (2015). "The galactic bar". In: *Lessons from the Local Group*. Springer, pp. 43–52.

Gieren, Wolfgang et al. (2013). "The Araucaria Project. A Distance Determination to the Local Group Spiral M33 from Near-Infrared Photometry of Cepheid Variables". In: *The Astrophysical Journal* 773.1, p. 69.

Gómez, Facundo A et al. (2012a). "Signatures of minor mergers in Milky Way like disc kinematics: ringing revisited". In: *Monthly Notices of the Royal Astronomical Society* 419.3, pp. 2163–2172.

Gómez, Facundo A et al. (2012b). "Vertical density waves in the Milky Way disc induced by the Sagittarius dwarf galaxy". In: *Monthly Notices of the Royal Astronomical Society* 429.1, pp. 159–164.

Gómez, Facundo A et al. (2021). "A Tidally Induced Global Corrugation Pattern in an External Disk Galaxy Similar to the Milky Way". In: *The Astrophysical Journal* 908.1, p. 27.

Hagen, Jorrit HJ et al. (2019). "The tilt of the velocity ellipsoid in the Milky Way with Gaia DR2". In: *arXiv preprint arXiv:1902.05268*.

Harper, Douglas et al. (2001). "Online etymology dictionary". In.

Hasan, Hashima, Daniel Pfenniger, and Colin Norman (1993). "Galactic bars with central mass concentrations-Three-dimensional dynamics". In: *The Astrophysical Journal* 409, pp. 91–109.

Haywood, Misha et al. (2018). "In disguise or out of reach: first clues about in situ and accreted stars in the stellar halo of the Milky Way from Gaia DR2". In: *The Astrophysical Journal* 863.2, p. 113.

Heintz, KE et al. (2018). "Unidentified quasars among stationary objects from Gaia DR2". In: *Astronomy & Astrophysics* 615, p. L8.

Helmi, Amina (2004). "Is the dark halo of our Galaxy spherical?" In: *Monthly Notices of the Royal Astronomical Society* 351.2, pp. 643–648.

— (2020). "Streams, substructures, and the early history of the Milky Way". In: *Annual Review of Astronomy and Astrophysics* 58, pp. 205–256.

Helmi, Amina and P Tim de Zeeuw (2000). "Mapping the substructure in the Galactic halo with the next generation of astrometric satellites". In: *Monthly Notices of the Royal Astronomical Society* 319.3, pp. 657–665.

Helmi, Amina et al. (2018a). "Gaia Data Release 2-Kinematics of globular clusters and dwarf galaxies around the Milky Way". In: *Astronomy & astrophysics* 616, A12.

Helmi, Amina et al. (2018b). "The merger that led to the formation of the Milky Way's inner stellar halo and thick disk". In: *Nature* 563.7729, p. 85.

Hernquist, Lars (1990). "An analytical model for spherical galaxies and bulges". In: *The Astrophysical Journal* 356, pp. 359–364.

Hilmi, T et al. (2020). "Fluctuations in galactic bar parameters due to bar-spiral interaction". In: *arXiv preprint arXiv:2003.05457*.

Hinkel, Austin, Susan Gardner, and Brian Yanny (2020a). "Axial Asymmetry Studies in Gaia Data Release 2 Yield the Pattern Speed of the Galactic Bar". In: *The Astrophysical Journal Letters* 899.1, p. L14.

— (2020b). "Probing Axial Symmetry Breaking in the Galaxy with Gaia Data Release 2". In: *The Astrophysical Journal* 893.2, p. 105.

Hoddeson, Lillian et al. (1997). "The Rise of the Standard Model: A History of Particle Physics from 1964 to 1979". In: DOI: 10.1017/CBO9780511471094.

Hogg, David W, Anna-Christina Eilers, and Hans-Walter Rix (2019). "Spectrophotometric parallaxes with linear models: Accurate distances for luminous red-giant stars". In: *The Astronomical Journal* 158.4, p. 147.

Holl, B et al. (2018). "Gaia Data Release 2-Summary of the variability processing and analysis results". In: *Astronomy & Astrophysics* 618, A30.

Hunt, Jason AS and Jo Bovy (2018). "The 4: 1 outer Lindblad resonance of a long-slow bar as an explanation for the Hercules stream". In: *Monthly Notices of the Royal Astronomical Society* 477.3, pp. 3945–3953.

Hunt, Jason AS et al. (2020). "The power of coordinate transformations in dynamical interpretations of Galactic structure". In: *Monthly Notices of the Royal Astronomical Society* 497.1, pp. 818–828.

Hunter, Cj and Alar Toomre (1969). "Dynamics of the Bending of the Galaxy". In: *The Astrophysical Journal* 155, p. 747.

Ideta, Makoto et al. (2000). "Time evolution of galactic warps in prolate haloes". In: *Monthly Notices of the Royal Astronomical Society* 311.4, pp. 733–740.

Iorio, Giuliano and Vasily Belokurov (2018). "The shape of the Galactic halo with Gaia DR2 RR Lyrae. Anatomy of an ancient major merger". In: *Monthly Notices of the Royal Astronomical Society* 482.3, pp. 3868–3879.

Iye, Masanori (1985). "Oscillations of rotating gas disks: p-modes, g-modes, and r-modes". In: *Symposium-International Astronomical Union*. Vol. 106. Cambridge University Press, pp. 535–536.

Jeans, J. H. (Dec. 1915). "On the theory of star-streaming and the structure of the universe". In: *Monthly Notices of the Royal Astronomical Society* 76, pp. 70–84. DOI: 10.1093/mnras/76.2.70.

Johnston, Kathryn V, David R Law, and Steven R Majewski (2005). "A two micron all sky survey view of the sagittarius dwarf galaxy. III. Constraints on the flattening of the galactic halo". In: *The Astrophysical Journal* 619.2, p. 800.

Jurić, Mario et al. (2008). "The Milky Way tomography with SDSS. I. Stellar number density distribution". In: *The Astrophysical Journal* 673.2, p. 864.

Kalberla, Peter MW and Jürgen Kerp (2009). "The Hi distribution of the milky way". In: *Annual review of astronomy and Astrophysics* 47, pp. 27–61.

Kalberla, PMW et al. (2007). "Dark matter in the Milky Way-II. The HI gas distribution as a tracer of the gravitational potential". In: *Astronomy & Astrophysics* 469.2, pp. 511–527.

Kallivayalil, Nitya et al. (Feb. 2013). "Third-epoch Magellanic Cloud Proper Motions. I. Hubble Space Telescope/WFC3 Data and Orbit Implications". In: *The Astrophysical Journal* 764.2, 161, p. 161. DOI: 10.1088/0004-637X/764/2/161. arXiv: 1301.0832 [astro-ph.CO].

Kamdar, Harshil et al. (2020). "Spatial and Kinematic Clustering of Stars in the Galactic Disk". In: *arXiv preprint arXiv:2007.10990*.

Kardar, Mehran (2007). *Statistical physics of particles*. Cambridge University Press.

Kerr, FJ (1957). "A Magellanic effect on the galaxy." In: *The Astronomical Journal* 62, pp. 93–93.

Kh, Sara Rezaei et al. (2018). "Detection of the Milky Way spiral arms in dust from 3D mapping". In: *Astronomy & Astrophysics* 618, A168.

Khoperskov, S et al. (2019a). "Hic sunt dracones: Cartography of the Milky Way spiral arms and bar resonances with Gaia Data Release 2". In: *arXiv preprint arXiv:1910.06335*.

Khoperskov, Sergey et al. (2019b). "The echo of the bar buckling: Phase-space spirals in Gaia Data Release 2". In: *Astronomy & Astrophysics* 622, p. L6.

Klypin, Anatoly A, Sebastian Trujillo-Gomez, and Joel Primack (2011). "Dark matter halos in the standard cosmological model: Results from the bolshoi simulation". In: *The Astrophysical Journal* 740.2, p. 102.

Koposov, SE et al. (2019). "Piercing the Milky Way: an all-sky view of the Orphan Stream". In: *Monthly Notices of the Royal Astronomical Society* 485.4, pp. 4726–4742.

Koppelman, Helmer, Amina Helmi, and Jovan Veljanoski (2018). "One large blob and many streams frosting the nearby stellar halo in Gaia DR2". In: *The Astrophysical Journal Letters* 860.1, p. L11.

Kuzmin, GG (1956). "Model of the steady galaxy allowing of the triaxial distribution of velocities". In: *Astronomicheskii Zhurnal* 33, p. 27.

Lancaster, Lachlan, Vasily Belokurov, and N. Wyn Evans (Apr. 2019). "Quantifying the smoothness of the stellar halo: a link to accretion history". In: 484.2, pp. 2556–2565. DOI: 10.1093/mnras/stz124. arXiv: 1804.09181 [astro-ph.GA].

Landy, Stephen D and Alexander S Szalay (1993). "Bias and variance of angular correlation functions". In: *The Astrophysical Journal* 412, pp. 64–71.

Laporte, Chervin F. P. et al. (Jan. 2018a). "Response of the Milky Way's disc to the Large Magellanic Cloud in a first infall scenario". In: *Monthly Notices of the Royal Astronomical Society* 473.1, pp. 1218–1230. DOI: 10.1093/mnras/stx2146. arXiv: 1608.04743 [astro-ph.GA].

Laporte, Chervin FP et al. (2018b). "The influence of Sagittarius and the Large Magellanic Cloud on the stellar disc of the Milky Way Galaxy". In: *Monthly Notices of the Royal Astronomical Society* 481.1, pp. 286–306.

Laporte, Chervin FP et al. (2019). "Footprints of the Sagittarius dwarf galaxy in the Gaia data set". In: *Monthly Notices of the Royal Astronomical Society* 485.3, pp. 3134–3152.

Laporte, Chervin FP et al. (2020). "Bar resonances and low angular momentum moving groups in the Galaxy revealed by their stellar ages". In: *Astronomy & Astrophysics* 643, p. L3.

Law, David R and Steven R Majewski (2010). "The Sagittarius dwarf galaxy: a model for evolution in a triaxial Milky Way halo". In: *The Astrophysical Journal* 714.1, p. 229.

Leane, Rebecca K and Tracy R Slatyer (2019). "Revival of the dark matter hypothesis for the galactic center gamma-ray excess". In: *Physical review letters* 123.24, p. 241101.

— (2020). "The Enigmatic Galactic Center Excess: Spurious Point Sources and Signal Mismodeling". In: *arXiv preprint arXiv:2002.12371*.

Levine, Evan S, Leo Blitz, and Carl Heiles (2006). "The vertical structure of the outer Milky Way HI disk". In: *The Astrophysical Journal* 643.2, p. 881.

Levine, Evan S et al. (2008). "The Warp and Spiral Arms of the Milky Way". In: *Mapping the Galaxy and Nearby Galaxies*. Springer, pp. 85–90.

Lewandowski, Matthew and Leonardo Senatore (Aug. 2017). "IR-safe and UV-safe integrands in the EFTofLSS with exact time dependence". In: 2017.08, pp. 037–037. DOI: 10.1088/1475-7516/2017/08/037. URL: https://doi.org/10.1088/1475-7516/2017/08/037.

— (Mar. 2020). "An analytic implementation of the IR-resummation for the BAO peak". In: 2020.03, pp. 018–018. DOI: 10.1088/1475-7516/2020/03/018. URL: https://doi.org/10.1088/1475-7516/2020/03/018.

Li, Chengdong, Gang Zhao, and Chengqun Yang (2019). "Galactic Rotation and the Oort Constants in the Solar Vicinity". In: *The Astrophysical Journal* 872.2, p. 205.

Li, Zhao-Yu and Juntai Shen (2012). "The vertical X-shaped structure in the Milky Way: evidence from a simple boxy bulge model". In: *The Astrophysical Journal Letters* 757.1, p. L7.

Li, Zhi et al. (2021). "Gas Dynamics in the Galaxy: Total Mass Distribution and the Bar Pattern Speed". In: *arXiv preprint arXiv:2103.10342*.

Lindegren, L et al. (2018). "Gaia Data Release 2-The astrometric solution". In: *Astronomy & Astrophysics* 616, A2.

Lindegren, Lennart et al. (2012). "The astrometric core solution for the Gaia mission-Overview of models, algorithms, and software implementation". In: *Astronomy & Astrophysics* 538, A78.

Łokas, Ewa L (2009). "The mass and velocity anisotropy of the Carina, Fornax, Sculptor and Sextans dwarf spheroidal galaxies". In: *Monthly Notices of the Royal Astronomical Society: Letters* 394.1, pp. L102–L106.

— (2019). "Anatomy of a buckling galactic bar". In: *Astronomy & Astrophysics* 629, A52.

Luri, X et al. (2018). "Gaia Data Release 2-Using Gaia parallaxes". In: *Astronomy & Astrophysics* 616, A9.

Mackereth, J Ted et al. (Nov. 2018). "The origin of accreted stellar halo populations in the Milky Way using APOGEE, Gaia, and the EAGLE simulations". In: *Monthly Notices of the Royal Astronomical Society* 482.3, pp. 3426–3442. ISSN: 0035-8711. DOI: 10.1093/mnras/sty2955. eprint: https://academic.oup.com/mnras/article-pdf/482/3/3426/26660129/sty2955.pdf. URL: https://doi.org/10.1093/mnras/sty2955.

Marel, Roeland P van der and Nitya Kallivayalil (2013). "Third-epoch Magellanic Cloud proper motions. II. The Large Magellanic Cloud rotation field in three dimensions". In: *The Astrophysical Journal* 781.2, p. 121.

Martinez-Valpuesta, Inma, Isaac Shlosman, and Clayton Heller (2006). "Evolution of stellar bars in live axisymmetric halos: recurrent buckling and secular growth". In: *The Astrophysical Journal* 637.1, p. 214.

Matsumoto, Makoto and Takuji Nishimura (1998). "Mersenne twister: a 623-dimensionally equidistributed uniform pseudo-random number generator". In: *ACM Transactions on Modeling and Computer Simulation (TOMACS)* 8.1, pp. 3–30.

Metropolis, N et al. (1953a). "Introduction of the metropolis algorithm for molecular-dynamics simulation". In: *J. Chem. Phys* 21, p. 1987.

Metropolis, Nicholas et al. (1953b). "Equation of state calculations by fast computing machines". In: *The journal of chemical physics* 21.6, pp. 1087–1092.

Michalik, Daniel et al. (2015). "Gaia astrometry for stars with too few observations. A Bayesian approach". In: *Astronomy & Astrophysics* 583, A68.

Minchev, Ivan, J Nordhaus, and AC Quillen (2007). "New constraints on the galactic bar". In: *The Astrophysical Journal Letters* 664.1, p. L31.

Minniti, D. et al. (July 2010). "VISTA Variables in the Via Lactea (VVV): The public ESO near-IR variability survey of the Milky Way". In: *New Astronomy* 15.5, pp. 433–443. DOI: 10.1016/j.newast.2009.12.002. arXiv: 0912.1056 [astro-ph.GA].

Mishurov, Yu N and IA Zenina (1999). "Yes, the Sun is located near the corotation circle". In: *Astronomy and Astrophysics* 341, pp. 81–85.

Miyamoto, M. and R. Nagai (Jan. 1975). "Three-dimensional models for the distribution of mass in galaxies." In: *Publications of the Astronomical Society of Japan* 27, pp. 533–543.

Monari, Giacomo et al. (2017). "Tracing the Hercules stream with Gaia and LAMOST: new evidence for a fast bar in the Milky Way". In: *Monthly Notices of the Royal Astronomical Society: Letters* 466.1, pp. L113–L117.

Morganson, Eric et al. (2016). "Mapping the monoceros ring in 3D with Pan-STARRS1". In: *The Astrophysical Journal* 825.2, p. 140.

Moster, Benjamin P., Thorsten Naab, and Simon D. M. White (Feb. 2013). "Galactic star formation and accretion histories from matching galaxies to dark matter haloes". In: *Monthly Notices of the Royal Astronomical Society* 428.4, pp. 3121–3138. DOI: 10.1093/mnras/sts261. arXiv: 1205.5807 [astro-ph.CO].

Mróz, Przemek et al. (2019). "Rotation Curve of the Milky Way from Classical Cepheids". In: *The Astrophysical Journal Letters* 870.1, p. L10.

Mühlbauer, G and Walter Dehnen (2003). "Kinematic response of the outer stellar disk to a central bar". In: *Astronomy & Astrophysics* 401.3, pp. 975–984.

Myeong, G C et al. (July 2019). "Evidence for two early accretion events that built the Milky Way stellar halo". In: *Monthly Notices of the Royal Astronomical Society* 488.1, pp. 1235–1247. ISSN: 0035-8711. DOI: 10.1093/mnras/stz1770. eprint: https://academic.oup.com/mnras/article-pdf/488/1/1235/28936943/stz1770.pdf. URL: https://doi.org/10.1093/mnras/stz1770.

Nadler, EO et al. (2021). "Constraints on Dark Matter Properties from Observations of Milky Way Satellite Galaxies". In: *Physical review letters* 126.9, p. 091101.

Navarro, Julio F, Carlos S Frenk, and Simon DM White (1997). "A universal density profile from hierarchical clustering". In: *The Astrophysical Journal* 490.2, p. 493.

Necib, Lina et al. (2019). "Evidence for a Vast Prograde Stellar Stream in the Solar Vicinity". In: *arXiv preprint arXiv:1907.07190*.

Nelson, Robert W and Scott Tremaine (1995). "The Damping and excitation of galactic warps by dynamical friction". In: *Monthly Notices of the Royal Astronomical Society* 275.4, pp. 897–920.

Newberg, Heidi Jo et al. (2002). "The ghost of Sagittarius and lumps in the halo of the Milky Way". In: *The Astrophysical Journal* 569.1, p. 245.

Noether, Emmy (Jan. 1918). "Invariant Variation Problems". In: *Nachr. v. d. Ges. d. Wiss. Zu Göttingen*, pp. 235–237.

Norris, John E (1994). "Population studies. 12: The duality of the galactic halo". In: *The Astrophysical Journal* 431, pp. 645–657.

O'Hare, Ciaran AJ et al. (2020). "Velocity substructure from Gaia and direct searches for dark matter". In: *Physical Review D* 101.2, p. 023006.

Olver, Peter J (1993). *Applications of Lie groups to differential equations*. 2nd ed. Springer-Verlag.

Ostriker, Jeremiah Paul and Philip JE Peebles (1973). "A numerical study of the stability of flattened galaxies: or, can cold galaxies survive?" In: *The Astrophysical Journal* 186, pp. 467–480.

Panagia, Nino (1999). "Distance to SN 1987A and the LMC". In: *Symposium-International Astronomical Union*. Vol. 190. Cambridge University Press, pp. 549–554.

Patel, Ekta, Gurtina Besla, and Sangmo Tony Sohn (2016). "Orbits of massive satellite galaxies–I. A close look at the Large Magellanic Cloud and a new orbital history for M33". In: *Monthly Notices of the Royal Astronomical Society* 464.4, pp. 3825–3849.

Peebles, Phillip James Edwin and Phillip J Peebles (1993). *Principles of physical cosmology*. Princeton university press.

Peñarrubia, Jorge et al. (2015). "A timing constraint on the (total) mass of the Large Magellanic Cloud". In: *Monthly Notices of the Royal Astronomical Society: Letters* 456.1, pp. L54–L58.

Pfenniger, Daniel and Daniel Friedli (1991). "Structure and dynamics of 3D N-body barred galaxies". In: *Astronomy and Astrophysics* 252, pp. 75–93.

Piffl, T, Z Penoyre, and J Binney (2015). "Bringing the Galaxy's dark halo to life". In: *Monthly Notices of the Royal Astronomical Society* 451.1, pp. 639–650.

Piffl, T. et al. (Oct. 2014). "Constraining the Galaxy's dark halo with RAVE stars". In: *Monthly Notices of the Royal Astronomical Society* 445.3, pp. 3133–3151. ISSN: 0035-8711. DOI: 10.1093/mnras/stu1948. eprint: http://oup.prod.sis.lan/mnras/article-pdf/445/3/3133/3589606/stu1948.pdf. URL: https://doi.org/10.1093/mnras/stu1948.

Portail, Matthieu (2016). "Structure and dynamics of the galactic bulge and bar". PhD thesis. lmu.

Portail, Matthieu et al. (Mar. 2015). "Made-to-measure models of the Galactic box/-peanut bulge: stellar and total mass in the bulge region". In: *Monthly Notices of the Royal Astronomical Society* 448.1, pp. 713–731. DOI: 10.1093/mnras/stv058. arXiv: 1502.00633 [astro-ph.GA].

Portail, Matthieu et al. (2016). "Dynamical modelling of the galactic bulge and bar: the Milky Way's pattern speed, stellar and dark matter mass distribution". In: *Monthly Notices of the Royal Astronomical Society*, stw2819.

Posti, Lorenzo and Amina Helmi (2019). "Mass and shape of the Milky Way's dark matter halo with globular clusters from Gaia and Hubble". In: *Astronomy & Astrophysics* 621, A56.

Prescott, C Yi et al. (1978). "Parity non-conservation in inelastic electron scattering". In: *Physics Letters B* 77.3, pp. 347–352.

Price-Whelan, Adrian M et al. (2015). "A reinterpretation of the Triangulum–Andromeda stellar clouds: a population of halo stars kicked out of the Galactic disc". In: *Monthly Notices of the Royal Astronomical Society* 452.1, pp. 676–685.

Prusti, Timo et al. (2016). "The gaia mission". In: *Astronomy & Astrophysics* 595, A1.

Purcell, Chris W et al. (2011). "The Sagittarius impact as an architect of spirality and outer rings in the Milky Way". In: *Nature* 477.7364, p. 301.

Quillen, Alice C (2002). "Growth of a peanut-shaped bulge via resonant trapping of stellar orbits in the vertical inner Lindblad resonances". In: *The Astronomical Journal* 124.2, p. 722.

Quillen, Alice C et al. (2014). "A vertical resonance heating model for X-or peanut-shaped galactic bulges". In: *Monthly Notices of the Royal Astronomical Society* 437.2, pp. 1284–1307.

Raboud, Didier et al. (1998). "Evidence for a signature of the galactic bar in the solar neighbourhood". In: *arXiv preprint astro-ph/9802266*.

Reid, MJ et al. (2019). "Trigonometric Parallaxes of High-mass Star-forming Regions: Our View of the Milky Way". In: *The Astrophysical Journal* 885.2, p. 131.

Ribas, Ignasi et al. (2005). "First determination of the distance and fundamental properties of an eclipsing binary in the Andromeda Galaxy". In: *The Astrophysical Journal Letters* 635.1, p. L37.

Robin, Annie C et al. (2003). "A synthetic view on structure and evolution of the Milky Way". In: *Astronomy & Astrophysics* 409.2, pp. 523–540.

Robin, Annie C et al. (2012). "Stellar populations in the Milky Way bulge region: towards solving the Galactic bulge and bar shapes using 2MASS data". In: *Astronomy & Astrophysics* 538, A106.

Rubin, Vera C and W Kent Ford Jr (1970). "Rotation of the Andromeda nebula from a spectroscopic survey of emission regions". In: *The Astrophysical Journal* 159, p. 379.

Rybizki, Jan et al. (2021). "Characterizing the Gaia radial velocity sample selection function in its native photometry". In: *Monthly Notices of the Royal Astronomical Society* 500.1, pp. 397–409.

Sanders, Jason L, Leigh Smith, and N Wyn Evans (2019). "The pattern speed of the Milky Way bar from transverse velocities". In: *Monthly Notices of the Royal Astronomical Society* 488.4, pp. 4552–4564.

Sartoretti, P et al. (2018). "Gaia Data Release 2-Processing the spectroscopic data". In: *Astronomy & Astrophysics* 616, A6.

Schlegel, David J., Douglas P. Finkbeiner, and Marc Davis (June 1998). "Maps of Dust Infrared Emission for Use in Estimation of Reddening and Cosmic Microwave Background Radiation Foregrounds". In: *The Astrophysical Journal* 500.2, pp. 525–553. DOI: 10.1086/305772. arXiv: astro-ph/9710327 [astro-ph].

Schulz, A. E. et al. (May 2013). "Gravitational collapse in one dimension". In: *Monthly Notices of the Royal Astronomical Society* 431, pp. 49–62. DOI: 10.1093/mnras/stt073. arXiv: 1206.0299.

Schutz, Katelin (2020). "Subhalo mass function and ultralight bosonic dark matter". In: *Physical Review D* 101.12, p. 123026.

Schutz, Katelin et al. (2018). "Constraining a Thin Dark Matter Disk with G a i a". In: *Physical review letters* 121.8, p. 081101.

Searle, Leonard and Robert Zinn (1978). "Compositions of halo clusters and the formation of the galactic halo". In: *The Astrophysical Journal* 225, pp. 357–379.

Sellwood, JA (2010). "A recent Lindblad resonance in the solar neighbourhood". In: *Monthly Notices of the Royal Astronomical Society* 409.1, pp. 145–155.

Shen, Juntai and JA Sellwood (2006). "Galactic warps induced by cosmic infall". In: *Monthly Notices of the Royal Astronomical Society* 370.1, pp. 2–14.

Skowron, Dorota M et al. (2019). "A three-dimensional map of the Milky Way using classical Cepheid variable stars". In: *Science* 365.6452, pp. 478–482.

Sofue, Yoshiaki and Vera Rubin (Jan. 2001). "Rotation Curves of Spiral Galaxies". In: *Annual Review of Astronomy and Astrophysics* 39, pp. 137–174. DOI: 10.1146/annurev.astro.39.1.137. arXiv: astro-ph/0010594 [astro-ph].

Sparke, Linda S and Stefano Casertano (1988). "A model for persistent galactic warps". In: *Monthly Notices of the Royal Astronomical Society* 234.4, pp. 873–898.

Spitzer Jr., Lyman (1942). "The Dynamics Of The Interstellar Medium". In: *Astrophysical Journal* 95, p. 329.

Spoto, Federica et al. (2018). "Gaia Data Release 2-Observations of solar system objects". In: *Astronomy & astrophysics* 616, A13.

Stassun, Keivan G and Guillermo Torres (2018). "Evidence for a systematic offset of-80 micro-arcseconds in the Gaia DR2 parallaxes". In: *arXiv preprint arXiv:1805.03526*.

Thorne, Kip S. and Roger D. Blandford (2017). *Modern Classical Physics*. Princeton University Press.

Tremaine, S and MD Weinberg (1984). "A kinematic method for measuring the pattern speed of barred galaxies". In: *The Astrophysical Journal* 282, pp. L5–L7.

Trick, Wilma H (2020). "Identifying resonances of the Galactic bar in Gaia DR2: II. Clues from angle space". In: *arXiv preprint arXiv:2011.01233*.

Trick, Wilma H et al. (2021). "Identifying resonances of the Galactic bar in Gaia DR2: I. Clues from action space". In: *Monthly Notices of the Royal Astronomical Society* 500.2, pp. 2645–2665.

van der Marel, Roeland P (2011). In: *The Local Group as an Astrophysical Laboratory*. Ed. by Mario Livio and Thomas M. Brown.

Vasiliev, Eugene (2019). "Systematic errors in Gaia DR2 astrometry and their impact on measurements of internal kinematics of star clusters". In: *Monthly Notices of the Royal Astronomical Society* 489.1, pp. 623–640.

Vasiliev, Eugene, Vasily Belokurov, and Denis Erkal (2021). "Tango for three: Sagittarius, LMC, and the Milky Way". In: *Monthly Notices of the Royal Astronomical Society* 501.2, pp. 2279–2304.

Vera-Ciro, Carlos and Amina Helmi (2013). "Constraints on the shape of the Milky Way dark matter halo from the Sagittarius stream". In: *The Astrophysical Journal Letters* 773.1, p. L4.

Wall, Jasper Vivian and Charles R Jenkins (2012). *Practical statistics for astronomers*. Cambridge University Press.

Waller, William H (2017). *The Milky Way: an insider's guide*. Princeton University Press.

Wegg, Christopher and Ortwin Gerhard (Nov. 2013). "Mapping the three-dimensional density of the Galactic bulge with VVV red clump stars". In: *Monthly Notices of the Royal Astronomical Society* 435.3, pp. 1874–1887. DOI: 10.1093/mnras/stt1376. arXiv: 1308.0593 [astro-ph.GA].

Wegg, Christopher, Ortwin Gerhard, and Matthieu Portail (May 2015). "The structure of the Milky Way's bar outside the bulge". In: *Monthly Notices of the Royal Astronomical Society* 450.4, pp. 4050–4069. ISSN: 0035-8711. DOI: 10.1093/mnras/stv745. eprint: http://oup.prod.sis.lan/mnras/article-pdf/450/4/4050/5766721/stv745.pdf. URL: https://doi.org/10.1093/mnras/stv745.

Weinberg, Martin D (1985). "Evolution of barred galaxies by dynamical friction". In: *Monthly Notices of the Royal Astronomical Society* 213.3, pp. 451–471.

— (1993). "Kinematic signature of a rotating bar near a resonance". In: *arXiv preprint astro-ph/9304026*.

Weinberg, Martin D and Leo Blitz (2006). "A Magellanic Origin for the Warp of the Galaxy". In: *The Astrophysical Journal Letters* 641.1, p. L33.

Wenger, Marc et al. (2000). "The SIMBAD astronomical database-The CDS reference database for astronomical objects". In: *Astronomy and Astrophysics Supplement Series* 143.1, pp. 9–22.

Widrow, Lawrence M and John Dubinski (2005). "Equilibrium disk-bulge-halo models for the Milky Way and Andromeda galaxies". In: *The Astrophysical Journal* 631.2, p. 838.

Widrow, Lawrence M et al. (2012). "Galactoseismology: discovery of vertical waves in the Galactic disk". In: *The Astrophysical Journal Letters* 750.2, p. L41.

Williams, M. E. K. et al. (Oct. 2013). "The wobbly Galaxy: kinematics north and south with RAVE red-clump giants". In: *Monthly Notices of the Royal Astronomical Society* 436.1, pp. 101–121. ISSN: 0035-8711. DOI: 10.1093/mnras/stt1522. eprint: https://academic.oup.com/mnras/article-pdf/436/1/101/18500408/stt1522.pdf. URL: https://doi.org/10.1093/mnras/stt1522.

Xu, Yan et al. (2015). "Rings and radial waves in the disk of the Milky Way". In: *The Astrophysical Journal* 801.2, p. 105.

Yan, Yepeng et al. (2019). "Chemical and Kinematic Properties of the Galactic Disk from the LAMOST and Gaia Sample Stars". In: *The Astrophysical Journal* 880.1, p. 36.

Yanny, Brian and Susan Gardner (2013). "The stellar number density distribution in the local solar neighborhood is North-South asymmetric". In: *The Astrophysical Journal* 777.2, p. 91.

Zinn, Joel C et al. (2019). "Confirmation of the Gaia DR2 Parallax Zero-point Offset Using Asteroseismology and Spectroscopy in the Kepler Field". In: *The Astrophysical Journal* 878.2, p. 136.

Vita

Austin Hinkel

Education

Ph.D., Physics - University of Kentucky 2021 (expected)
M.S., Physics - University of Kentucky 2018
B.S., Physics - University of Kentucky 2016

Academic Employment

Colorado College
Visiting Assistant Professor 8/2021 - present

University of Kentucky
Graduate Research and Teaching Assistant 8/2016 - present

Publications

A. Hinkel, S. Gardner, and B. Yanny, "Applying the Two-Point Correlation Function to the Milky Way: A novel, model-independent way of detecting variations in structure throughout the Galaxy," (working title) In preparation.

A. Hinkel, S. Gardner, and B. Yanny, "Axial Asymmetry Studies in Gaia Data Release 2 Yield the Pattern Speed of the Galactic Bar," The Astrophysical Journal Letters. (2020). 899.1: L14. https://doi.org/10.3847/2041-8213/aba905.

A. Hinkel, S. Gardner, and B. Yanny, "Probing Axial Symmetry Breaking in the Galaxy with Gaia Data Release 2," The Astrophysical Journal. (2020). 893.2: 105. https://iopscience.iop.org/article/10.3847/1538-4357/ab8235/.

S. Gardner, A. Hinkel, and B. Yanny, "Applying Noether's Theorem to Matter in the Milky Way: Evidence for External Perturbations and Non-Steady-State Effects from Gaia Data Release 2," The Astrophysical Journal. (2020). 890.2: 110. https://iopscience.iop.org/article/10.3847/1538-4357/ab66c8/.

A. Hinkel, "Modeling Extrasolar Trojan Asteroids in Gravitational Potentials of Migrating Jovian-like Planets to Inform Future Observation," University of Kentucky Honors Program Capstone Collection, senior thesis (2016). https://uknowledge.uky.edu/honprog/22.

A. Hinkel, "The Brocard-Ramanujan Problem and an Unexpected Connection to Primitive Pythagorean Triples," In preparation.

Awards and Honors

U. Kentucky College of Arts & Sciences Dean's Competitive Fellowship: Fall 2020.

GAANN Fellow, U.S. Dept. of Education for study at the U. Kentucky: Fall 2018 - Spring 2019.

Three time Universities Research Association Visiting Scholars Program grant winner: 2018 - 2021.

American Physical Society Five Sigma Physicist Award: 2016.

U. Kentucky Dept. of Physics & Astronomy Outstanding Senior & Outstanding Junior Awards.

U. Kentucky Presidential Scholarship: Fall 2012 - Spring 2016.

U. Kentucky Department of Physics and Astronomy Scholarship: Fall 2014 - Spring 2016.

Sigma Pi Sigma Physics Honor Society inductee: 2015.